Optical Studies of Super-Collimation in Photonic Crystals

by

Marcus Dahlem

Licenciatura, Optics (Applied Physics)
Oporto University, 2001

Submitted to the Department of Electrical Engineering and Computer Science
in Partial Fulfillment of the Requirements for the Degree of
Master of Science in Electrical Engineering and Computer Science

at the

Massachusetts Institute of Technology

June 2005

Signature of Author .....
Department of Electrical Engineering and Computer Science
June 19, 2005

Certified by .....
Erich P. Ippen
Elihu Thompson Professor of Electrical Engineering
Professor of Physics
Thesis Supervisor

Accepted by .....
Arthur C. Smith
Chair, Department Committee on Graduate Stundents
Department of Electrical Engineering and Computer Science

Optical Studies of Super-Collimation in Photonic Crystals

by

Marcus Dahlem

Submitted to the Department of Electrical Engineering and Computer Science
on June 19, 2005 in Partial Fulfillment of the
Requirements for the Degree of Master of Science in
Electrical Engineering and Computer Science

Abstract

Recent developments in material science and engineering have made possible the fabrication of photonic crystals for optical wavelengths. These periodic structures of alternating high-to-low index of refraction materials allow the observation of peculiar effects, in particular, the propagation of optical beams without spatial spreading. This effect, called super-collimation (also known as self-collimation), allows diffraction-free propagation of micron-sized beams over centimeter-scale distances. This linear effect is a natural result of the unique dispersive properties of photonic crystals. In this thesis, these dispersive properties are studied in a two-dimensional photonic crystal slab. Both qualitative and quantitative descriptions are presented. The beam propagation method was used to simulate the evolution of a Gaussian beam inside such structures. The wavelength dependence of the super-collimation effect was studied, and it was observed that the optimum wavelength for this device was around 1500 nm. A precise contact-mode near-field optical microscopy technique was used to obtain high-resolution images of the beam profile at different positions along the photonic crystal, and showed that a 2 μm beam width was conserved over 3 mm. In addition, high-resolution confocal measurements confirmed the size of the beam after 5 mm of propagation. The figure of merit associated with the super-collimation effect is defined by the number of diffraction lengths over which the beam stays collimated. The diffraction length is the distance in which a beam will broaden to $2^{1/2}$ of its initial width. Previous experimental studies showed figures of merit smaller than 6; the results of this experiment show figures of merit as high as 376, which correspond to more than 14200 lattice constants. Preliminary results were obtained with an 8 mm sample that could achieve a figure of merit of 601.

Thesis Supervisor: Erich P. Ippen
Title: Elihu Thompson Professor of Electrical Engineering
Professor of Physics

MARCUS DAHLEM IS SUPPORTED BY A FELLOWSHIP FROM THE PORTUGUESE SCIENCE AND TECHNOLOGY FOUNDATION (FCT)

Acknowledgements

In the sciences, we are now uniquely privileged to sit side by side with the giants on whose shoulders we stand.

-- Gerald Holton

True in the sciences and true in life! And I have the privilege to sit among wonderful and talented people. All their support made this journey smooth and fun, and I am thankful to them. Not forgetting anyone is a hard task, but I will try to do my best.

First of all, I want to thank my thesis supervisor, Professor Erich Ippen. His great scientific knowledge and vision escapes out of his modest and discrete figure, in a natural and pleasant way. All his guidance, patience, flexibility and generosity helped me along the way... and of course, his sense of humor and Oktoberfests! Thanks for proofreading my thesis and for inviting me over for Thanksgiving! I am grateful to all your support!

Along the same lines, I want to extend my thanks to Peter Rakich. It has been a true joy to work with him in the lab, and his creativity has no limits. He has been a great mentor and he has made research a fun game to play. Peter, thanks for all your patience! You have been more than a labmate; you have been a really good friend! And thanks for proofreading my thesis.

Jason Sickler and his discipline have been a great help. Besides a wonderful ski trip organizer, he has been particularly helpful in discussing Matlab coding and in

clarifying my English language questions, including proofreading this thesis. He has a great sense of humor and has been a great officemate and friend. Thanks for the company at lunch!

I also want to acknowledge the rest of my research group, which creates a professional, healthy and peaceful working environment. In particular, I want to thank Juliet Gopinath for all her guidance and constant availability to help, Ali Motamedi, Vikas Sharma and Aurea Zare for their great company and humor, Hanfei Shen, Milos Popovic and Mike Watts for always willing to help, and Donna Gale and Dorothy Fleischer, our administrative assistants.

I have had a very good time with my collaborators. I want to thank them all for making this project possible. Many thanks to the fabrication people, Sheila Tandon, Professor Leslie Kolodziejski and Gale Petrich, and to the theory people, Professor John Joannopoulos, Marin Soljacic and Mihai Ibanescu.

I cannot forget all the wonderful help and flexibility I have had from the EECS graduate office, in particular from Marilyn Pierce. She has been extremely kind, helpful and effective, and I am grateful for all her help. I also want to thank my academic advisor, Professor Martin Schmidt, for his good guidance.

Since I came to MIT, I have been living in Ashdown House. It is a wonderful place to live, and its community is unique! Thanks to all the friends I made there, and many thanks to my very loved housemasters, Ann Orlando and Professor Terry Orlando. They are part of my family and they have been present on all occasions. Also, special thanks to Bhuwan Singh, who passed away in 2004. He always battled to make the world a better place, and we all miss him very much.

The MIT community is an endless resource of exploration, and all the student activities I have been involved in have definitely made me see things from a broader perspective. Special thanks to Catarina Bjelkengren for being such a *söt flicka*, Angie

Chow for being great company, and Lucy Wong for her smile. They inspire me and keep my life a constant challenge. Also, my Portuguese friends at MIT have been great and I have had really good times in their presence, in particular with Filipa Sá, Rita Oliveira, Rita Sousa, Pedro Pinto, Jorge Oliveira, Catarina Reis and Gonçalo Soares.

Although far away, my friends back home keep supporting me. Many thanks to everyone from OUP, CNE (especially Conceição Santos), and INESC Porto (especially Professor José Luís Santos). I had unforgettable moments with them all and it is always very rewarding to see them again! In particular, Rita Lopes will always be in my thoughts.

I want to extend my thanks to my family, especially to my parents who always gave me freedom and support to explore new worlds!

Finally, I want to thank the Portuguese Science and Technology Foundation (FCT) for the fellowship that is supporting me.

Contents

List of Figures

List of tables

1

INTRODUCTION

Diffraction of light is one of the most well known phenomena in physics. It was first studied in detail in the 17th century by Francesco Grimaldi (1618-1663), and it is, today, part of the common background of any person in the scientific community.

In 1987, Durnin *et al.* reported the first experimental evidence of a new class of diffraction-free beams – the Bessel beams – which could propagate in free space over meter-length distances without observable spreading[1]. These beams are solutions of the Helmholtz equation

$$(\nabla^2 + k^2) \cdot \Phi(\vec{r}) = 0 \qquad (1.1)$$

and can be interpreted as eigenbeams of a specific medium. Their amplitude Φ is proportional to a Bessel function, and the simplest solution is the zeroth-order Bessel beam:

$$\Phi(\vec{r}) = \exp(ik_z z).J_0(k_r r) \tag{1.2}$$

where k_z and k_r are the longitudinal and radial wavevectors, respectively. J_0 is the zeroth-order Bessel function of the first kind. Unlike the plane wave solution, Bessel beams have most of the energy well localized in a narrow central spot of wavelength-scale dimensions – Figure 1.1 – allowing optical tweezing of micron-sized particles[2].

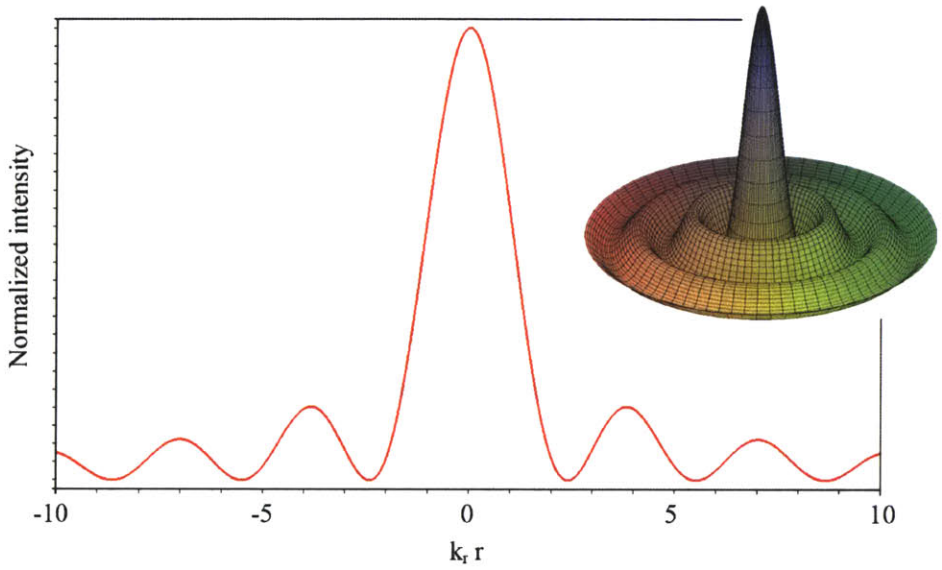

Figure 1.1 – Zeroth-order (first kind) Bessel beam. The amplitude (or intensity) is proportional to a Bessel function.

1.1 Motivation

Recently, a new linear non-diffracting phenomenon – self-collimation – has been observed in photonic crystals[3,4]. Like Bessel beams, propagation is achieved without spatial spreading. In practice, this phenomenon corresponds to guiding of light, without a

physical or induced waveguide! Or, in other words, it can be seen as a non-channel waveguide – Figure 1.2.

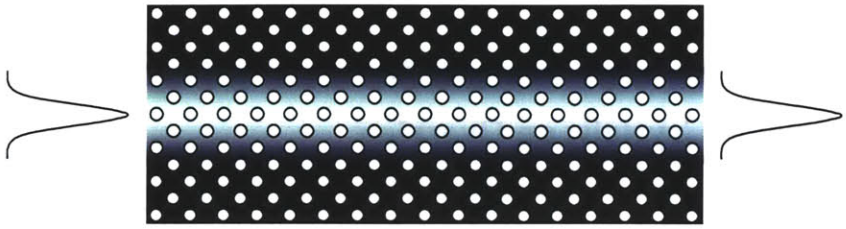

Figure 1.2 – Illustration of the concept of self-collimation. A beam propagates inside a photonic crystal without spatial spreading.

At first approach, this concept may look similar to the one behind spatial solitons. However, the physics is very different: self-collimation is a purely linear effect, while the formation of spatial solitons is nonlinear.

The fabrication of a photonic crystal (PhC) structure that can produce self-collimation in the optical domain is not a straightforward task. In order to observe interesting phenomena in such structures, the characteristic scale of the physical features has to be on the order of the wavelength of the light. The study of two-dimensional (2D) PhCs is a particularly promising field because their fabrication can take advantage of the infrastructures already developed for the silicon technology.

Previous work in self-collimation has shown propagation in 2D PhCs over small distances – about 65 μm^5. To take full advantage of these structures, larger propagation distances are required. One immediate application is the possibility of designing flexible optical interconnects. This would make the realization of all-optical integrated circuits a closer reality.

The present work takes one step further in the study of the self-collimation effect. It demonstrates propagation of an optical beam over centimeter-length scale distances, in

a 2D PhC. This improved feature – which will be called super-collimation – is a great contribution to the field, and opens new horizons to the fascinating world of densely integrated optical circuits.

1.2 Photonic Crystals: an Overview

A photonic crystal is an engineered material with peculiar dispersion characteristics, allowing the control and manipulation of light at very small scales[6,7]. The concept was first suggested in 1987 by Yablonovitch[8] and John[9], and such materials are also known as Photonic Bandgap (PBG) materials. It was anticipated that a 3D periodic structure of alternating high-to-low index of refraction could forbid the propagation of an electromagnetic wave in any direction, within a specific wavelength range, just like 1D layered dielectric mirrors do for normal incidence waves. In fact, these dielectric mirrors are considered 1D photonic crystals. Figure 1.3 illustrates a 2D PhC made of high-index cylinders in air.

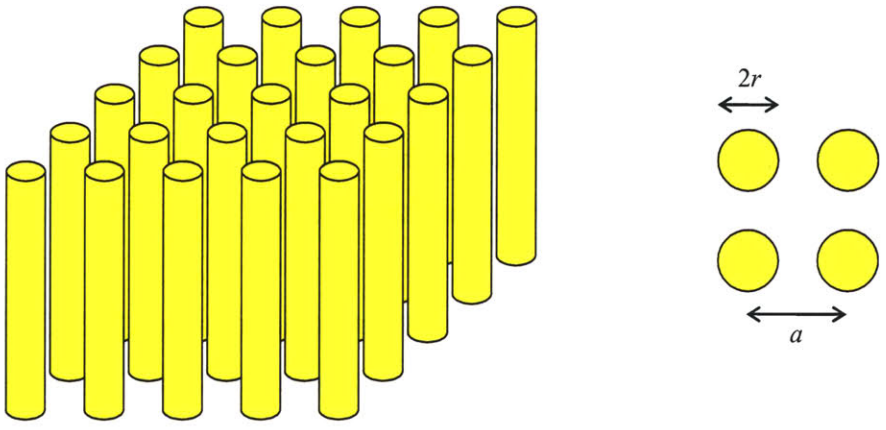

Figure 1.3 – 2D PhC formed by a stack of high-index cylinders in air, arranged in a square lattice. *a* is the lattice constant and *r* is the cylinder radius.

Advances in fabrication engineering processes have made possible the fabrication of 2D and 3D PhCs. From a conceptual point of view, 3D structures are unique, but fabrication constraints have made 2D slab PhCs much more attractive, especially when fabricated on a silicon-on-insulator (SOI) substrate. In addition, the creation of defects in a 3D PhC is much harder than in a 2D PhC. However, successful point-defect microcavities have recently been fabricated in a 3D PhC, for optical wavelengths[10].

PhCs have forbidden bands of energy in which radiation is not allowed to propagate. The unique shape of the band structure of a PhC is very different from the one of an isotropic material, which does not have bandgaps – Figure 1.4.

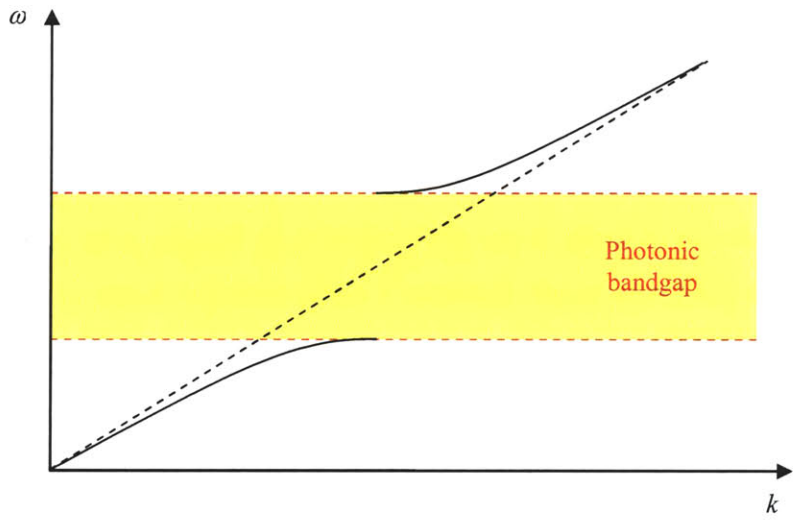

Figure 1.4 – Illustration of the band structure in a 1D PhC (solid lines), showing the existence of a photonic bandgap. The dashed line is the dispersion line for the isotropic case.

Next to the bandgap the group index of refraction n_g is very large (or equivalently, the group velocity v_g is small), and very interesting phenomena may occur.

$$n_g = \frac{c}{v_g} = \frac{c}{\partial\omega/\partial k} \to \infty \tag{1.3}$$

Localized defects inside the bandgap allow the creation of resonators (for a point defect), waveguides (for a line defect) or mirrors (for a plane defect). The defects are made by breaking the periodicity, normally by suppressing one point/row/plane of the lattice. In the particular case of a PhC waveguide, guiding of radiation of frequency within the bandgap is achieved because the light is not allowed to exist inside the PhC, therefore staying confined inside the defect. This type of waveguide has been widely studied[11-20], and low propagation losses have been shown at optical wavelengths. The smallest value reported is 5 dB/cm[19], around 1545 nm. This value is high compared to the 0.2 dB/km for a single mode fiber at 1550 nm, but is low taking into account the propagation distance over which these waveguides are used.

Numerous other demonstrations have been made over the last years. The superprism effect is one of them. It was demonstrated by Kosaka *et al.* in a 3D PhC[21], and by Wu *et al.* in a 2D GaAs-based structure[22]. More recently, Lupu *et al.* observed this effect in a 2D SOI PhC[23].

Another very important effect observed in PhCs is the self-collimation effect, which can be seen as a non-channel waveguiding process, as opposed to line-defect waveguides. Extensive work has been done in this area[3-5,24-35]. The effect was first observed by Kosaka *et al.* in a 3D PhC[3] and by Wu *et al.* in 2D triangular[4] and square[31] lattices. Self-collimation in a 2D SOI PhC has also been shown by Prather *et al.*, who measured losses as low as 1.1 dB/mm[33]. The related applications include beam steering and photonic integrated circuits[24], spot-size converters[25], lensing[29], bending and splitting of light[32,34,35], and routing[5].

1.3 Thesis Outline

The main focus of this work is the experimental demonstration of the super-collimation effect and all the underlying optical imaging techniques developed to study it.

Chapter 1 presents a brief introduction to PhCs and the state of the art in this field. Chapter 2 gives a qualitative description of both photonic crystals and the super-collimation effect. Chapter 3 describes the beam propagation method which is based on the diffraction theory. In addition, some simulations are presented and discussed. Chapter 4 presents the experimental results for the super-collimation effect. The several measurement techniques used to get the results are also considered. Chapter 5 is a short summary of the work done and discussion of applications and future work.

The work presented in this thesis was part of a project carried out in collaboration with fellow graduate students Peter Rakich, Sheila N. Tandon and Mihai Ibanescu. The idea to pursue this project, as well as theoretical guidance throughout the work, came from Marin Soljacic. The experimental setup and measurement techniques presented here were the result of close work with Peter Rakich, using his vast knowledge in waveguide characterization. The fabrication of the sample was done by Sheila N. Tandon from Professor Kolodziejski's group, and the band structure calculations for the device under study were performed by Mihai Ibanescu from Professor Joannopoulos' group.

2

PHOTONIC CRYSTALS

AND

SUPER-COLLIMATION EFFECT

This chapter gives a qualitative understanding of photonic crystals and explains the self-collimation effect, referred to as super-collimation from this point on.

2.1 Photonic Crystals

The concept of designing PhCs was first introduced by Yablonovitch[8] and John[9], in 1987. A PhC consists of a structure with a periodic change in the index of refraction. Such structures consist of a small building block that is repeated in space, and can be designed in 1D, 2D or 3D – Figure 2.1. The spatial period of such a structure – called lattice constant a – must be of the order of the wavelength of the light for which the PhC is designed. The traditional analogy to the PhC is a crystal formed by atoms or molecules. In such structures, electrons are not allowed to propagate freely. In some directions and for some frequencies there will be strong reflection, inhibiting the propagation in that

direction and for that energy – electronic bandgaps. Similarly, in a PhC, bands of energies in which propagation is not allowed are created, as a result of the periodicity. These bands are called photonic bandgaps. Due to this analogy, the field of PhCs is a merging of solid-state physics and electromagnetism.

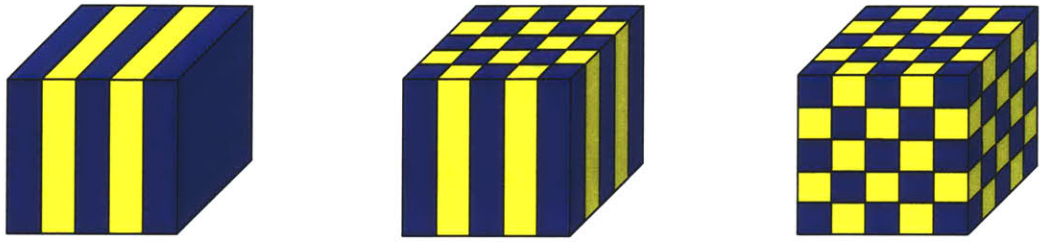

(a) *(b)* *(c)*

Figure 2.1 – Illustration of the concept of a PhC in *(a)* 1D, *(b)*, 2D and *(c)* 3D. High and low index materials are arranged in a periodic sequence, along one, two or three directions, respectively.

Radiation of frequencies within a bandgap cannot propagate inside the crystal. In the case of a 3D PhC, it is possible to create a complete photonic bandgap, i.e., a structure that does not allow propagation of radiation in any direction, within a range of frequencies. A local point defect can create a microcavity. Similarly, a line defect can create a waveguide, and a plane defect a mirror. The dimensions of such defects are very small when compared to conventional cavities, waveguides or mirrors, and therefore, PhCs can be used to control and manipulate light at very small scales[7]. Recall that conventional waveguides operate by total internal reflection and such structures are limited in terms of physical size. In addition, low loss sharp waveguide bends are not possible.

Since the current work focuses on a 2D PhC, the remaining text will only consider such a structure. A 2D PhC is periodic in two directions, and uniform in the third direction. Specifically, the structure considered is a square lattice of air holes in a

high-index material – Figure 2.2. The axes are chosen to have the propagation along the z direction. The base vectors in the real space are $\vec{a}_1 = (a,0)$ and $\vec{a}_2 = (0,a)$.

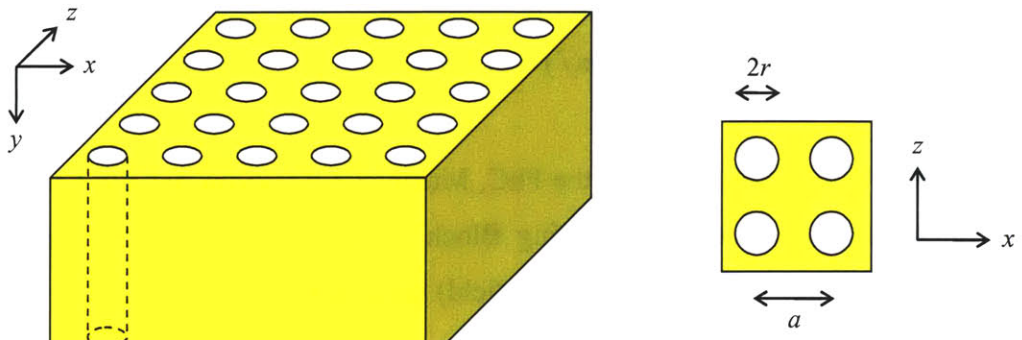

Figure 2.2 – 2D PhC formed by air cylinders in a high-index material, arranged in a square lattice. *a* is the lattice constant and *r* is the hole radius.

The reciprocal lattice of this 2D PhC is shown in Figure 2.3. By convention, the special points (0,0), (π/a,0) and (π/a,π/a) are called Γ, X and M, respectively. The base vectors in the reciprocal space are $\vec{b}_1 = (2\pi/a, 0)$ and $\vec{b}_2 = (0, 2\pi/a)$.

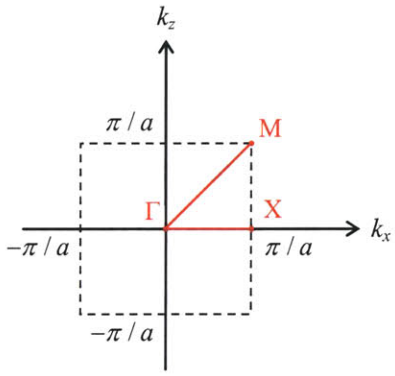

Figure 2.3 – Reciprocal lattice of the 2D square lattice PhC with lattice constant *a*. The dashed line represents the first Brillouin zone. Γ, X and M are symmetry points.

This 2D PhC has discrete translational symmetry in the *x*-*z* plane, i.e., it is invariant under a translation of any lattice vector $\vec{R} = l\vec{a}_1 + m\vec{a}_2$, where l and m are integers. This symmetry is represented by the periodicity in the dielectric constant:

$$\varepsilon(\vec{r}) = \varepsilon(\vec{r} + \vec{R}) \tag{2.1}$$

In order to find the modes of the PhC, Maxwell's equations have to be solved in this periodic dielectric medium. Applying Bloch's theorem, it can be shown that the eigenmodes of propagation (in the magnetic field) are given by

$$\vec{H}_{\vec{k},n}(\vec{r}) = \exp(i\vec{k}\cdot\vec{r})\,\vec{u}_{\vec{k},n}(\vec{r}) \tag{2.2}$$

where $\vec{k}$ identifies an eigenstate with frequency $\omega(\vec{k})$ and n is the label for the band number. The eigenmode given in the form of expression (2.2) is known as s Bloch state or Bloch wave, and it is the product of a plane wave with a periodic function. It can be seen as a regular plane wave (as in free space), spatially modulated by a periodic function, due to the periodicity of the lattice. The function $\vec{u}_{\vec{k},n}(\vec{r})$ is periodic for any lattice vector:

$$\vec{u}_{\vec{k},n}(\vec{r}) = \vec{u}_{\vec{k},n}(\vec{r} + \vec{R}) \tag{2.3}$$

Another important fact is that the eigenmodes with wavevectors $\vec{k}$ and $\vec{k} + \vec{G}$ are identical, where $\vec{G} = p\vec{b}_1 + q\vec{b}_2$ is the reciprocal lattice vector. Therefore, the mode frequencies are also periodic, and k_x and k_z need only to be considered in the interval $[-\pi/a, \pi/a]$. This region is called the Brillouin zone, and includes all the possible solutions. The collection of all the solutions (or dispersion relations for the eigenmodes) is known as the band structure.

The eigenmodes can be separated into two polarizations: TE (electric field parallel to the 2D plane) and TM (magnetic field parallel to the 2D plane). The band structures for these modes can be different. In the case of a square lattice of air holes in a high-index material, TE bandgaps are expected, as opposed to TM bandgaps for isolated high-index material in air. Also, the larger the index contrast is, the larger the bandgap.

An important characteristic of Maxwell's equations is that they do not have a characteristic length scale. This means that the band structure of two similar PhCs, differing by scale factors only, is the same, as long as the wavevectors and frequencies are scaled as well. This means that properties of the PhCs in certain wavelength ranges can be deduced from experimental results observed in other frequency ranges, easier to fabricate or measure.

The band structure of a 2D PhC is a three-dimensional surface. Figure 2.4 illustrates such a structure, for TE modes.

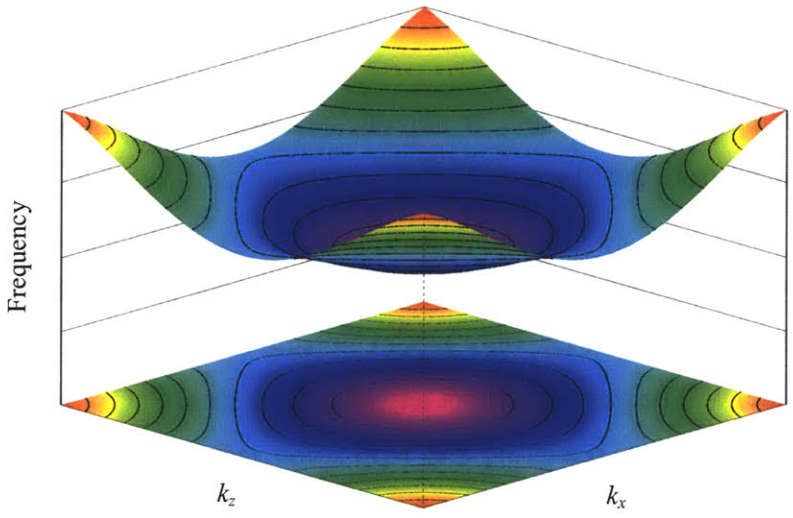

Figure 2.4 – Illustration of the photonic band structure (first band only) in a hypothetical 2D PhC, for TE modes. The bottom image represents the equifrequency contours of the band structure.

An easier way to represent this surface is to "walk" along the special directions Γ-X-M-Γ and plot the corresponding frequencies (shown in Figure 2.5).

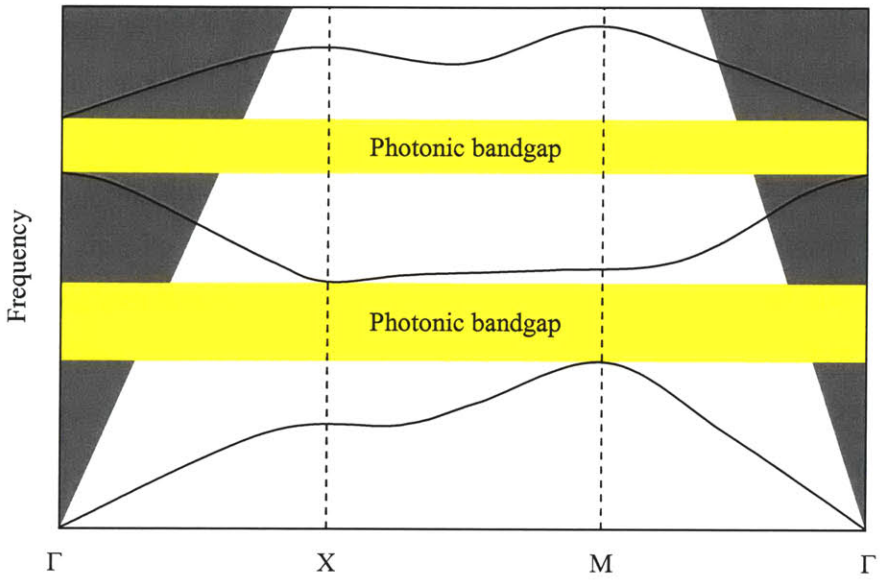

Figure 2.5 – Illustration of the photonic band structure in a hypothetical 2D PhC, for TE modes. The complicated surface is easily mapped in two dimensions by "walking" between the points Γ, X and M. The gray region represents the light cone.

The description presented here is introductory, and further understanding of this field can be obtained from the literature[6,36-42].

As a final remark, the vertical light confinement inside the 2D PhC is due to total internal reflection (TIR). However, only modes outside the light cone (or equivalently, below the light line) will be guided without any loss, in an ideal PhC[26]. In a real structure, losses are due to absorption, scattering and fabrication errors. If a mode lies inside the light cone, it will be leaky, i.e., it will not have total internal reflection, and losses will be experienced as it propagates. The light cone is determined by the over and under-cladding materials of the structure, as well as by the slab thickness. The structure considered in

this work – Figure 2.2 – is symmetric, surrounded by air both on top and bottom. The light cone is determined by the condition

$$k_{//} = \sqrt{k_x^2 + k_z^2} > k_{clad} = \frac{2\pi n_{clad}}{\lambda_0} = \frac{2\pi}{a}\Omega \tag{2.4}$$

where $k_{//}$ is the parallel (in plane) wavevector component and Ω the normalized frequency, defined as

$$\Omega = \frac{a}{\lambda_0} \tag{2.5}$$

In our real structure, considered in chapter 4, the under-cladding is not air, but SiO_2 instead, which has an index of refraction $n(SiO_2) = 1.45$. This will widen the light cone (or equivalently, lower the light line), making more modes leaky. However, in the experiment, the operation is within the first band of the PhC, which is not affected by the change in the light cone, for the considered wavelength ranges.

After describing the light confinement in the vertical direction, the next section considers the lateral confinement, which is due to distributed Bragg reflection.

2.2 Super-Collimation Effect

Super-collimation is a linear effect, totally independent of the light intensity. Unlike spatial solitons, there is no beam focusing (diffraction compensation) due to nonlinearities. Instead, PhCs can be designed to have dispersion properties that allow incident waves to naturally collimate in certain directions. Therefore, naming this effect "self-collimation" is misleading and may cause confusion among the broader audience.

Light propagation inside a PhC is governed by the band structure (or dispersion surface). Anomalous dispersion next to the band edge can be used to shape the light propagation inside the PhC. Figure 2.6 shows the equifrequency contours of the band structure from Figure 2.4. Each equifrequency contour is the cross section of the band structure surface, at a constant frequency.

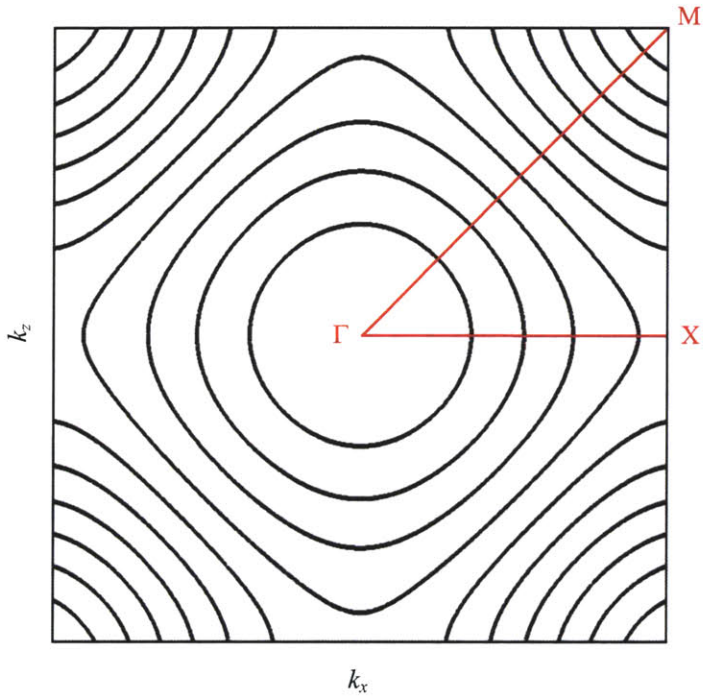

Figure 2.6 – Illustration of the equifrequency contours from the photonic band structure shown in Figure 2.4, in a hypothetical 2D PhC, for TE modes. This corresponds to the first band of the 2D square lattice PhC.

In addition to the circular contours (common in isotropic materials), square-like shapes are observed. In particular, the Γ-M direction is of special interest. The flat contour can be used to laterally confine the light. In fact, for a range of incident wavevectors, the propagation will be normal to the equifrequency contour, since the energy of the mode will propagate with a group velocity given by

$$\vec{v}_g = \nabla_{\vec{k}}\, \omega(\vec{k}) \tag{2.6}$$

which is perpendicular to the equifrequency contours – Figure 2.7.

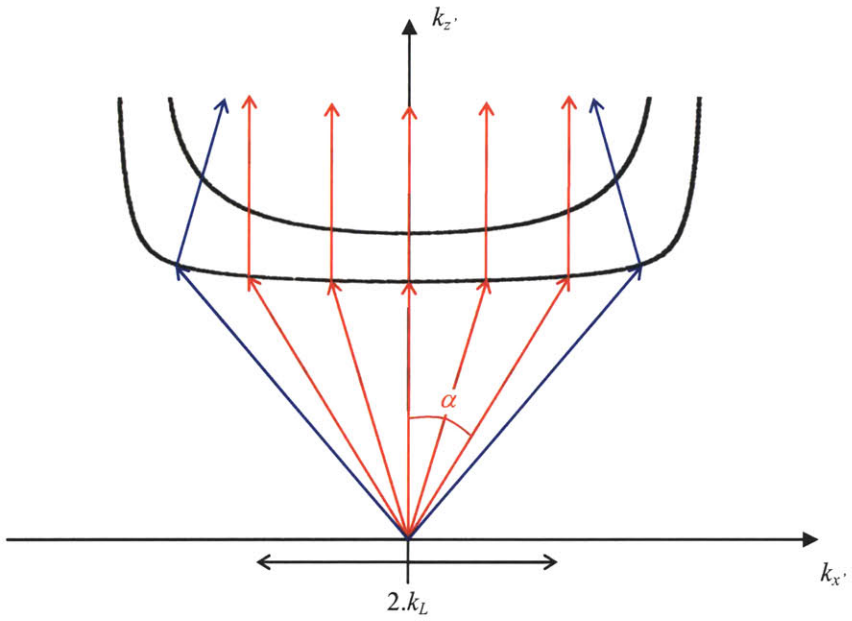

Figure 2.7 – Equifrequency contours in the Γ-M direction. The flat region of the contour allows super-collimation, for incident angles smaller than α.

This effect will be observed for incident angles smaller than α:

$$\alpha \leq \sin^{-1}\left(\frac{k_L}{2\pi}\frac{a}{\Omega}\right) \tag{2.7}$$

where $2.k_L$ is the width of the flat region of the contour. As an example, if $k_L = 1\ \mu m^{-1}$, $\Omega = 0.228$ and $a = 0.35\ \mu m$, then $\alpha \leq 14°$. Due to this alignment flexibility, the position of the input light source is not very critical.

Super-collimation can also be obtained when operating in the second band of the PhC, but now in the Γ-X direction. The description for this band of energies is similar to the one considered for the first band.

Any incident beam can potentially be collimated. In practice, the width of the flat contour may limit the minimum size of the beam. Also, if the dispersion surface is not exactly flat, beating patterns can appear. These issues are discussed in the next chapter.

As a final observation, it should also be clear that PhC lensing depends on the super-collimation effect[29].

The next chapter presents a different approach to understanding the super-collimation effect and includes some simulations that allow a better understanding of the practical observations made in chapter 4.

3

BASICS OF DIFFRACTION THEORY AND BEAM PROPAGATION METHOD

3.1 Super-Collimation Effect using Diffraction Theory

The super-collimation effect was presented in the previous chapter in a very qualitative way. A tractable and elegant way to describe this effect quantitatively is through the use of Fourier Optics[43-45]. Numerical simulations can be carried out using the *beam propagation method*[46], which is a method widely applied to the study of temporally and spatially varying waves. This approach is very powerful for considering wave propagation in axially varying waveguides, in both linear and nonlinear regimes. The beam propagation method (BPM) generally used in this approach is based on the fast Fourier transform (FFT) algorithm which is incorporated in our numerical software. BPM can be understood via analysis of the scalar Helmholtz wave equation, which is derived from the Maxwell's equations. In a source-free medium $(\vec{J} = \rho = 0)$, Maxwell's equations are:

$$\nabla \times \vec{H} = \frac{\partial \vec{D}}{\partial t} \tag{3.1}$$

$$\nabla \times \vec{E} = -\frac{\partial \vec{B}}{\partial t} \tag{3.2}$$

$$\nabla \cdot \vec{D} = 0 \tag{3.3}$$

$$\nabla \cdot \vec{B} = 0 \tag{3.4}$$

where $\vec{E}, \vec{H}, \vec{B}$ and $\vec{D}$ are real vector quantities that depend on position and time. In a dielectric medium (linear, isotropic, homogeneous, nondispersive and nonmagnetic) it is straightforward to derive the vector wave equation:

$$\nabla^2 \vec{E} - \varepsilon\mu_0 \frac{\partial^2 \vec{E}}{\partial t^2} = 0 \tag{3.5}$$

where ∇^2 is the Laplacian operator:

$$\nabla^2 = \frac{\partial^2}{\partial x^2} + \frac{\partial^2}{\partial y^2} + \frac{\partial^2}{\partial z^2} \tag{3.6}$$

$\vec{E}$ and $\vec{H}$ are vectors, and each individual component must also satisfy equation (3.5). So the wave equation can be rewritten in the scalar form:

$$\nabla^2 u - \varepsilon\mu_0 \frac{\partial^2 u}{\partial t^2} = 0 \tag{3.7}$$

where $u(\vec{r},t)$ is the real scalar wavefunction. $u(\vec{r},t)$ can be represented in terms of a complex function $U(\vec{r},t)$. This approach makes the analysis easier, and the physical quantity will be recovered by taking $u(\vec{r},t) = \mathrm{Re}\{U(\vec{r},t)\}$. The scalar wave equation becomes then:

$$\nabla^2 U - \varepsilon\mu_0 \frac{\partial^2 U}{\partial t^2} = 0 \tag{3.8}$$

Any solution to equation (3.8) represents a possible wave. Furthermore, according to the superposition principle, any linear combination of such solutions will also be a solution. Keeping this in mind, it is useful to consider a base of elementary time-harmonic (monochromatic) wavefunctions of the form

$$U(\vec{r},t) = U(\vec{r}) \,.\, \exp(-i\omega t)^{\dagger} \tag{3.9}$$

where $U(\vec{r})$ is known as the complex amplitude and ω is the angular frequency. Using this dependence, the scalar wave equation becomes

$$(\nabla^2 + k^2) \,.\, U(\vec{r}) = 0 \tag{3.10}$$

which is known as the Helmholtz equation. $k = \omega\sqrt{\varepsilon\mu_0}$ is known as the wavenumber and $\vec{k} = (k_x, k_y, k_z)$ is the wavevector. As mentioned in chapter 1, the Bessel beam is a solution of the Helmholtz equation. Other commonly used solutions are the plane wave and the spherical wave:

$$U(\vec{r}) = A \,.\, \exp(i\vec{k} \cdot \vec{r}) \tag{3.11}$$

$$U(\vec{r}) = \frac{A}{r} \,.\, \exp(ikr) \tag{3.12}$$

The wavelength λ and the wavenumber k are related by $k = k_0.n = 2\pi n / \lambda_0$, where n is the index of refraction of the medium and λ_0 the wavelength in free space.

---

† In this text the physics complex notation is used $(i = -j)$.

When the wavevectors propagate within a small angle with respect to the optical axis (or equivalently, the wavefronts lie next to the optical axis), an important approximation, called the *paraxial approximation*, can be made – Figure 3.1.

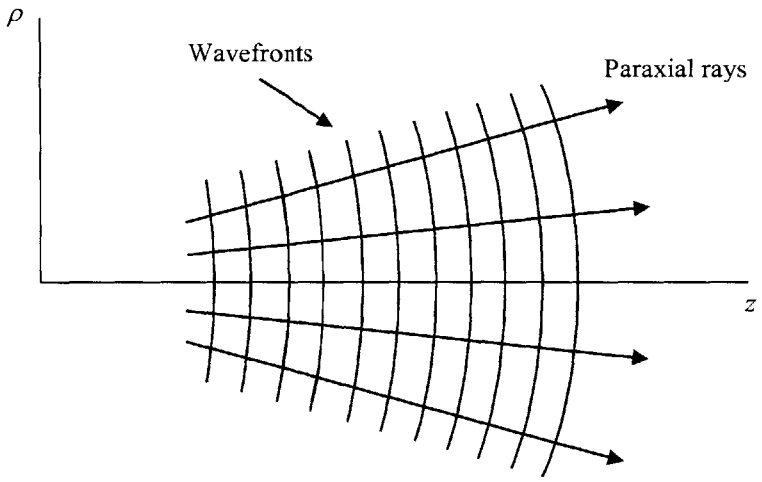

Figure 3.1 – Paraxial wave approximation

In the paraxial approximation, and assuming propagation along the z axis, the complex amplitude can be rewritten as a slowly varying envelope and a rapidly varying term:

$$U(\vec{r}) = A(\vec{r}) \,.\, \exp(ikz) \tag{3.13}$$

The variation of $A(\vec{r})$ is assumed to be small within the distance of one wavelength, i.e., the wave looks approximately like a plane wave for small distances of propagation. This condition is translated as $\Delta A \ll A$ for $\Delta z = \lambda$ and gives

$$\frac{\partial A}{\partial z} \ll kA \tag{3.14}$$

and

$$\frac{\partial^2 A}{\partial z^2} \ll k^2 A \tag{3.15}$$

This gives raise to the paraxial Helmholtz equation:

$$\nabla_T^2 A + 2ik\frac{\partial A}{\partial z} = 0 \tag{3.16}$$

where $\nabla_T^2 = \partial^2/\partial x^2 + \partial^2/\partial y^2$ is the transverse Laplacian operator.

The paraxial Helmholtz equation will give two important results: the Gaussian beam wavefunction (which is one of its solutions) and the description of the linear-space propagation of such a wave, allowing a straightforward and elegant explanation of the super-collimation effect.

3.1.1 The Gaussian Beam

The most interesting solution of the paraxial Helmholtz equation is the Gaussian beam, which is in the general form of equation (3.13). The complex envelope $A(\vec{r})$ for this solution is found to be[43]:

$$A(\vec{r}) = \frac{A_1}{q(z)} . \exp\left[ik\frac{\rho^2}{2q(z)}\right], \qquad q(z) = z - iz_0 \tag{3.17}$$

where A_1 is a constant and $\rho = \sqrt{x^2 + y^2}$ the radial distance. z_0 is the Rayleigh range, also known as the diffraction/dispersive length. The complex function $q(z)$ can be rewritten as

$$\frac{1}{q(z)} = \frac{1}{R(z)} + i\frac{\lambda}{\pi W^2(z)} \tag{3.18}$$

where $W(z)$ and $R(z)$ define the beam radius and the wavefront radius of curvature. Finally, the complex amplitude $U(\vec{r})$ is given by:

$$U(\vec{r}) = A_0 \frac{W_0}{W(z)} . \exp\left[-\frac{\rho^2}{W^2(z)}\right] . \exp\left[ikz + ik\frac{\rho^2}{2R(z)} - i\zeta(z)\right] \tag{3.19}$$

The several beam parameters are defined as follows:

$$A_0 = \frac{A_1}{-iz_0} \tag{3.20}$$

$$W_0 = \left(\frac{\lambda z_0}{\pi}\right)^{\frac{1}{2}} \tag{3.21}$$

$$W(z) = W_0\left[1 + \left(\frac{z}{z_0}\right)^2\right]^{\frac{1}{2}} \tag{3.22}$$

$$R(z) = z\left[1 + \left(\frac{z}{z_0}\right)^2\right] \tag{3.23}$$

$$\zeta(z) = \tan^{-1}\frac{z}{z_0} \tag{3.24}$$

Remember that the real Gaussian function is $u(\vec{r},t) = \mathrm{Re}\{U(\vec{r}) . \exp(-i\omega t)\}$. When $z = 0$, all the phase terms vanish and $U(\vec{r})$ is real:

$$U(\vec{r}) = A_0 . \exp\left(-\frac{\rho^2}{W_0^2}\right) \tag{3.25}$$

In addition, at this position the beam radius $W(z)$ has its smallest value W_0, normally called the waist radius. $2W_0$ is the waist diameter or spot size. At $z = z_0$ the beam radius is $\sqrt{2}\, W_0$. At very large distances z, the diverging Gaussian beam defines a cone with an angle

$$\theta = \frac{2\lambda}{\pi W_0} \tag{3.26}$$

Another important parameter is the depth of focus or confocal parameter, which is defined as the axial distance within which the beam radius is $< \sqrt{2}\, W_0$. This value is $2\, z_0$:

$$2z_0 = \frac{2\,\pi\, W_0^2}{\lambda} \tag{3.27}$$

3.1.2 Linear-Space Propagation of a Paraxial Beam

As seen, the Gaussian beam is an interesting solution of the paraxial Helmholtz equation. To understand the super-collimation effect it is essential to know the analytical tools that describe how this beam propagates and evolves inside a medium. Furthermore, this will allow us to numerically simulate the propagation and spatial evolution of such a beam.

As a start point, it is useful to represent the solution of the Helmholtz equation $U(\vec{r}) = U(x,z)$ in the Fourier integral form, considering propagation in a planar waveguide, i.e, $\partial / \partial y = 0$, and along the z direction:

$$U(x,z) = \int_{-\infty}^{\infty} \tilde{U}(k_x, z)\,.\,\exp(ik_x x)\,\frac{dk_x}{2\pi} \tag{3.28}$$

Plugging this expression into the Helmholtz equation gives:

$$\frac{\partial^2 \tilde{U}}{\partial z^2} + k_z^2 \, \tilde{U} = 0 \tag{3.29}$$

where k_z is the longitudinal component of the wavevector $\vec{k}$:

$$k_z^2 = k^2 - k_x^2 \tag{3.30}$$

The solution of equation (3.29) is

$$\tilde{U}(k_x, z) = \tilde{U}(k_x, z_i) \,.\, \exp\left[ik_z(z - z_i)\right] \tag{3.31}$$

where $\tilde{U}(k_x, z_i)$ is the Fourier transform of $U(x, z_i)$:

$$\tilde{U}(k_x, z_i) = \mathrm{F}\{U(x, z_i)\} = \int_{-\infty}^{\infty} U(x, z_i) \,.\, \exp(-ik_x x)\, dx \tag{3.32}$$

z_i is a position where the complex amplitude $U(x, z_i)$ is known. For any other position, the amplitude $U(\vec{r}) = U(x, z)$ is obtained by computing the inverse Fourier transform of equation (3.31).

Using equation (3.13), which is valid in the slowly varying envelope approximation, and computing $U(\vec{r})$ at $z = z_i + h$, one obtain the complex envelope $A(\vec{r})$:

$$A(x, z_i + h) = \mathrm{F}^{-1}\left[\exp(i\delta k_z h)\, \mathrm{F}\{A(x, z_i)\}\right] \tag{3.33}$$

where $\delta k_z = k_z - k$.

In simple words, this equation computes the beam profile at a distance h from the point $z = z_i$, where the beam profile is known. Therefore, the beam evolution can be computed at any point in space. A complete image of the propagation and spatial evolution of the beam is obtained by repeating this step for a couple of points within the range of interest. This method constitutes the beam propagation method introduced at the beginning of the section.

Looking at this expression, it is clear that if the phase term $\exp(i\delta k_z h)$ (which is a function of k_x) is constant, the amplitude $A(\vec{r})$ will not change its spatial profile. This is equivalent to saying that k_z is constant (independent of k_x) and equation (3.30) is not valid. Under this condition, the only effect of the propagation is an additional phase factor. This describes the super-collimation effect. On the other hand, when k_z depends on k_x there will be a spatial evolution of the beam profile, computed by equation (3.33) and governed by the shape of the equifrequency contours of the medium.

As seen in chapter 2, the dispersion surfaces of a PhC are unique and allow super-collimation at frequencies that exhibit flat equifrequency contours. The next section presents some simulations of the beam evolution for different contour shapes.

3.2 Numerical Simulations

The mathematical description of the super-collimation effect was presented in the previous section. The lines that follow show numerical simulations of a Gaussian beam propagating inside a medium under different equifrequency contour shapes. Figure 3.2 shows the different shapes considered. These curves are based on the curves obtained from the experimental device (presented in chapter 4) and correspond to the first band of the PhC, for TE radiation (electric field parallel to the 2D plane). Ω is the normalized

frequency, defined in expression (2.5). Propagation is in the z direction (corresponding to the Γ-M direction in the reciprocal lattice) – Figure 3.3*(a)*.

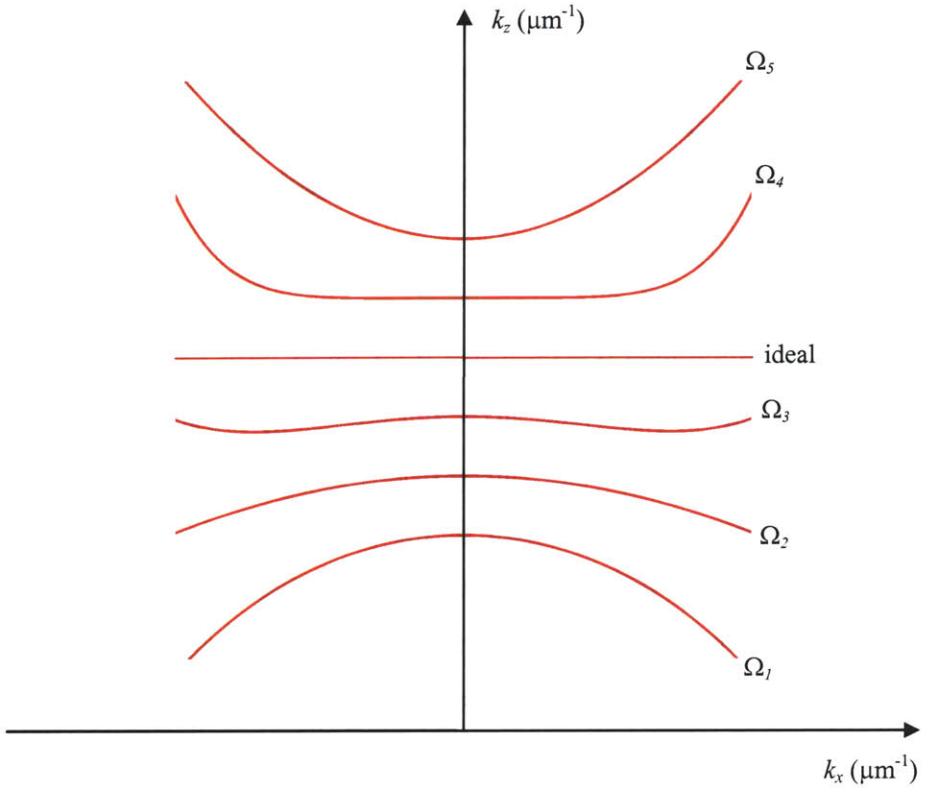

Figure 3.2 – Qualitative plot of the equifrequency contours used for the simulation. The ideal case is the flat dispersion curve. Ω_1, Ω_2, Ω_3, Ω_4 and Ω_5 represent different normalized frequencies.

For simulations purposes, the curves are defined as:

$$\begin{aligned}
\Omega_1 &: \quad k_z = \sqrt{k^2 - k_x^2} \\
\Omega_2 &: \quad k_z = k - \mathrm{a}\, k_x^2 \\
\Omega_3 &: \quad k_z = k - \mathrm{a}\, k_x^2 + \mathrm{b}\, k_x^4 \\
\Omega_4 &: \quad k_z = k + \mathrm{c}\, k_x^6 \\
\Omega_5 &: \quad k_z = k + \mathrm{d}\, k_x^2
\end{aligned} \tag{3.34}$$

where a, b, c and d are constants. The real curves were not used in the simulation.

To study the effect of the flat dispersion surfaces on the beam evolution inside the crystal, a Gaussian beam is launched at the input of a PhC slab in the Γ-M direction. The spot size is 1.7 μm and the wavelength is 1500 nm. The PhC is a square lattice of holes in a thin layer of silicon and the effective index is assumed to be 2.2, for the wavelength used. This number is also calculated from the contours of the real device and is discussed later. Figure 3.3 illustrates the simulated configuration.

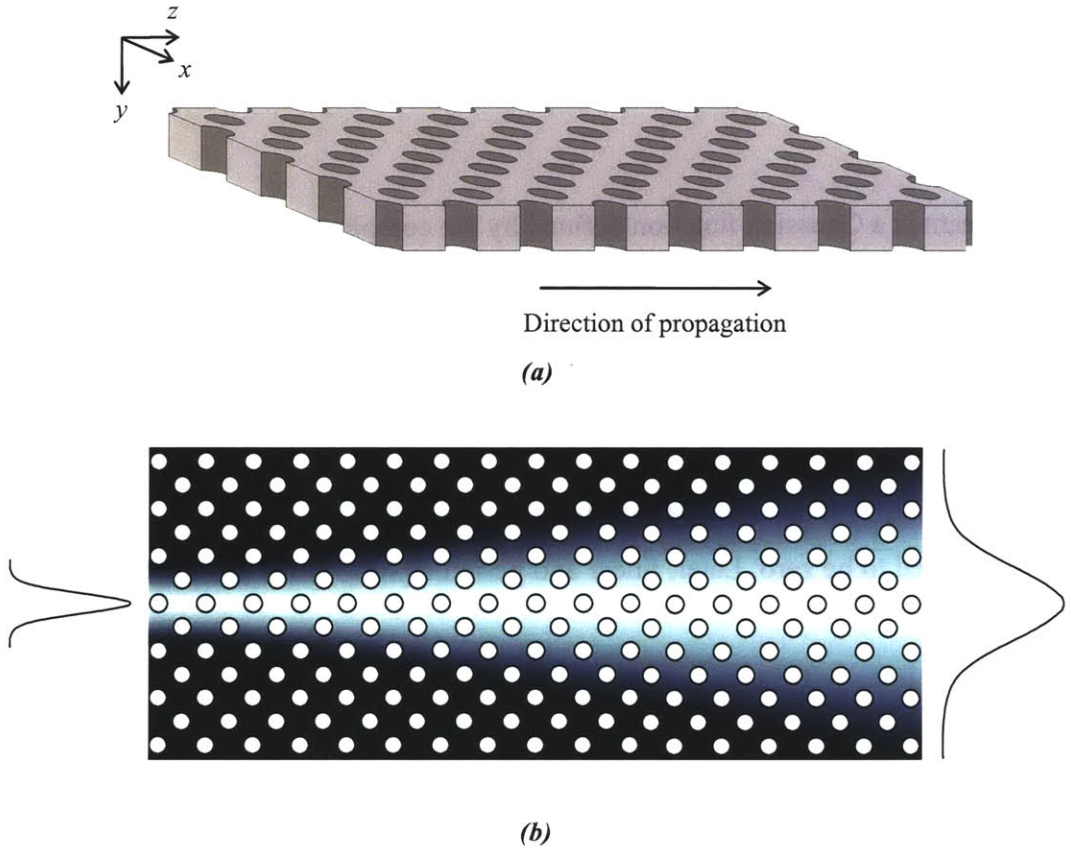

Figure 3.3 – Simulation of the propagation of a Gaussian beam inside a square lattice PhC, along the Γ-M direction. The size of the holes is not to scale. *(a)* 3D view of the device and *(b)* top view of the beam inside the PhC.

The simulation implements the BPM, by computing equation (3.33) for a number of discrete points, using MATLAB®. The Fourier transform is computed using a FFT algorithm. The simulation parameters are presented below:

- $z_{in} = 0$
- $z_{out} = 1000\ \mu m$
- $\Delta z = 2.5\ \mu m$
- $x_{min} = -1000\ \mu m$
- $x_{max} = 1000\ \mu m$
- $\Delta x = 0.4\ \mu m$
- $n = 2.2$ (effective index)
- $\lambda_0 = 1.5\ \mu m$
- $W_0 = 0.85\ \mu m$

The input beam is a Gaussian function defined by the complex envelope

$$A(x,0) = \exp\left(-\frac{x^2}{W_0^2}\right).\exp(i\phi) \tag{3.35}$$

The spot size is $2W_0$, as defined earlier. For the first set of simulations, the initial phase term ϕ is assumed to be zero. Later, linear and periodic phase terms are considered.

3.2.1 No Input Phase

In this subsection, the simplest case is considered. A simple Gaussian beam is launched at the input and propagates under the different contours shown in Figure 3.2. The ideal case is the one with the flat dispersion curve, shown in Figure 3.4.

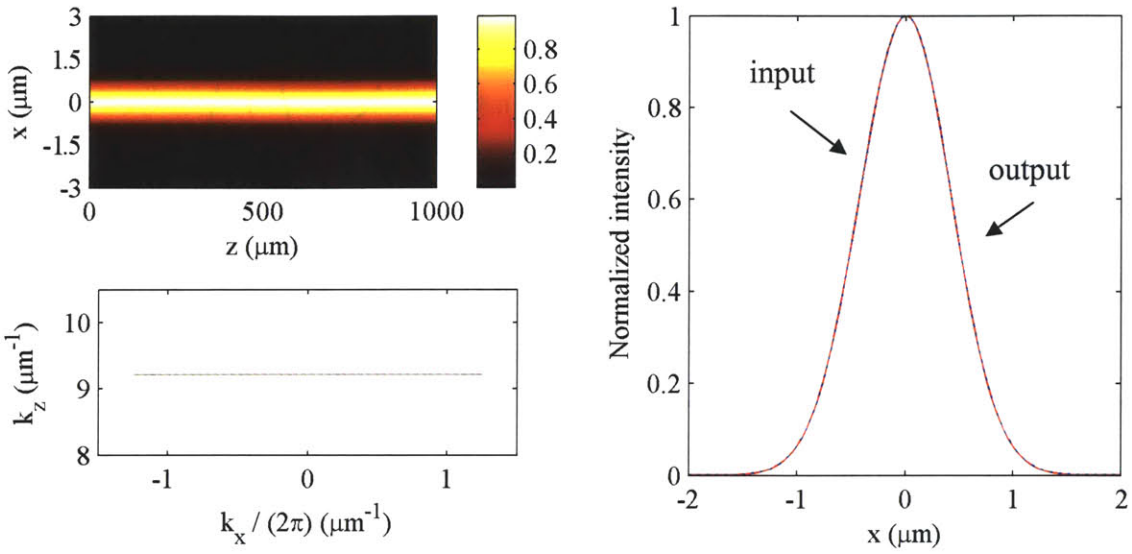

Figure 3.4 – Simulated propagation of a Gaussian beam under the ideal flat contour: *(left top)* computed image over a 1 mm propagation, *(left bottom)* computed equifrequency contour and *(right)* input and output transverse beam profiles in the PhC.

As seen, the beam stays collimated inside the PhC. The effect of the different contour shapes is presented in the figures that follow, for contours Ω_1 to Ω_5.

The different contours have different influence on the beam shape inside the PhC. Looking at the simulation results, three regimes can be identified:

- conventional diffraction-like regime – Figure 3.5, Figure 3.6 and Figure 3.9 – where the beam has a homogeneous spread as it propagates, conserving the transverse Gaussian profile;
- super-collimation regime – Figure 3.8 – where the beam propagates without lateral spreading;
- fringe-like regime – Figure 3.7 – where the beam spreads out and the transverse beam profile shape is not conserved (transverse oscillations are observed).

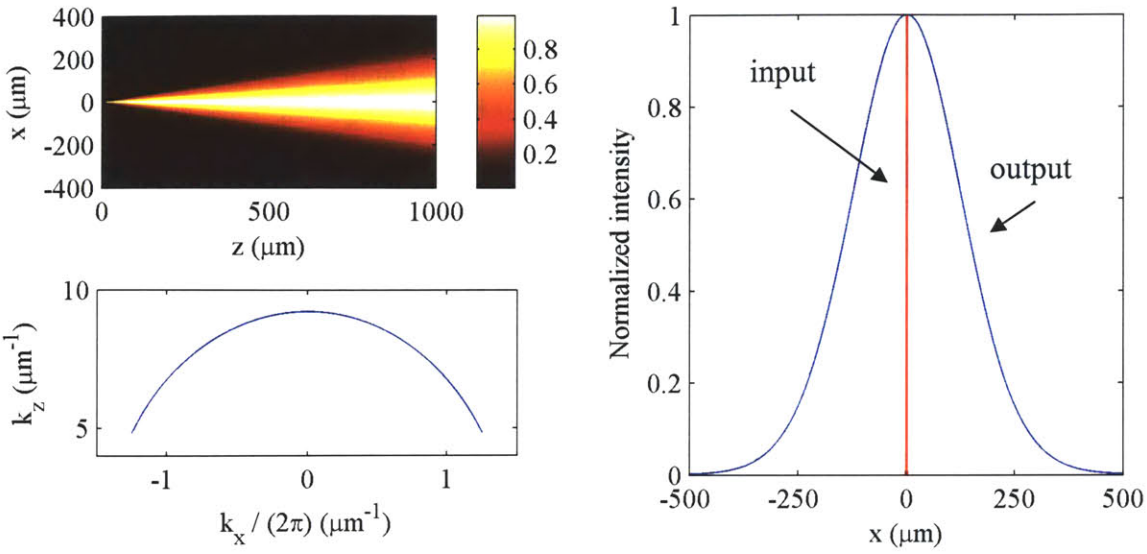

Figure 3.5 – Simulated propagation of a Gaussian beam under contour Ω_1: *(left top)* computed image over a 1 mm propagation, *(left bottom)* computed equifrequency contour and *(right)* input and output transverse beam profiles in the PhC.

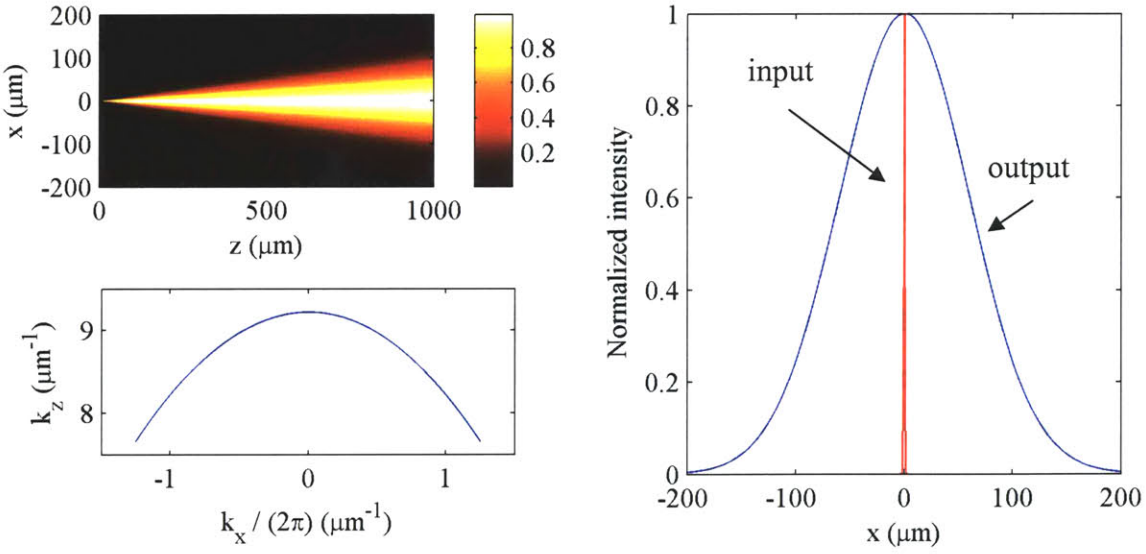

Figure 3.6 – Simulated propagation of a Gaussian beam under contour Ω_2: *(left top)* computed image over a 1 mm propagation, *(left bottom)* computed equifrequency contour and *(right)* input and output transverse beam profiles in the PhC.

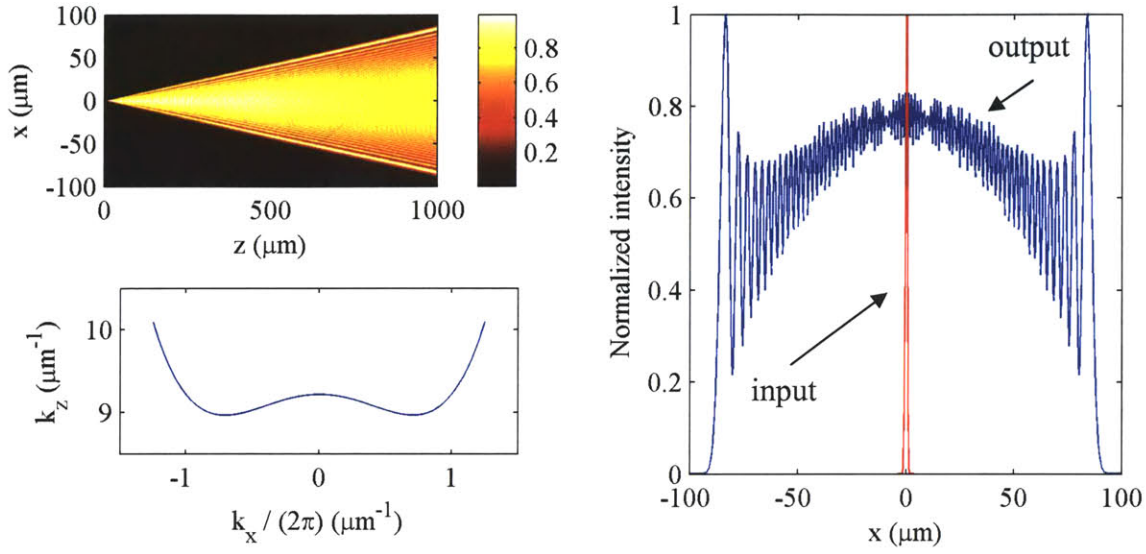

Figure 3.7 – Simulated propagation of a Gaussian beam under contour Ω_3: *(left top)* computed image over a 1 mm propagation, *(left bottom)* computed equifrequency contour and *(right)* input and output transverse beam profiles in the PhC.

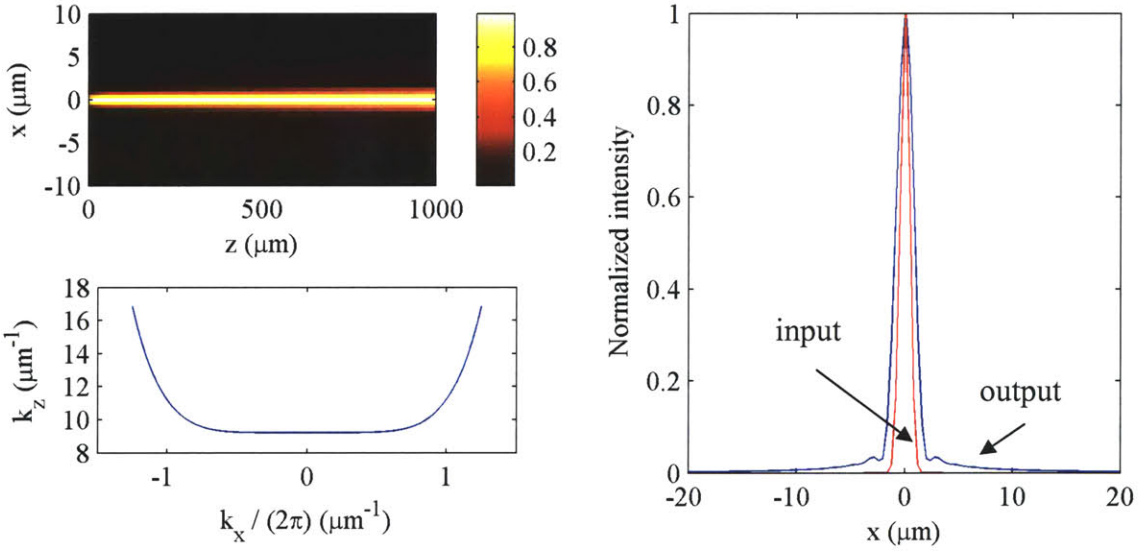

Figure 3.8 – Simulated propagation of a Gaussian beam under contour Ω_4: *(left top)* computed image over a 1 mm propagation, *(left bottom)* computed equifrequency contour and *(right)* input and output transverse beam profiles in the PhC.

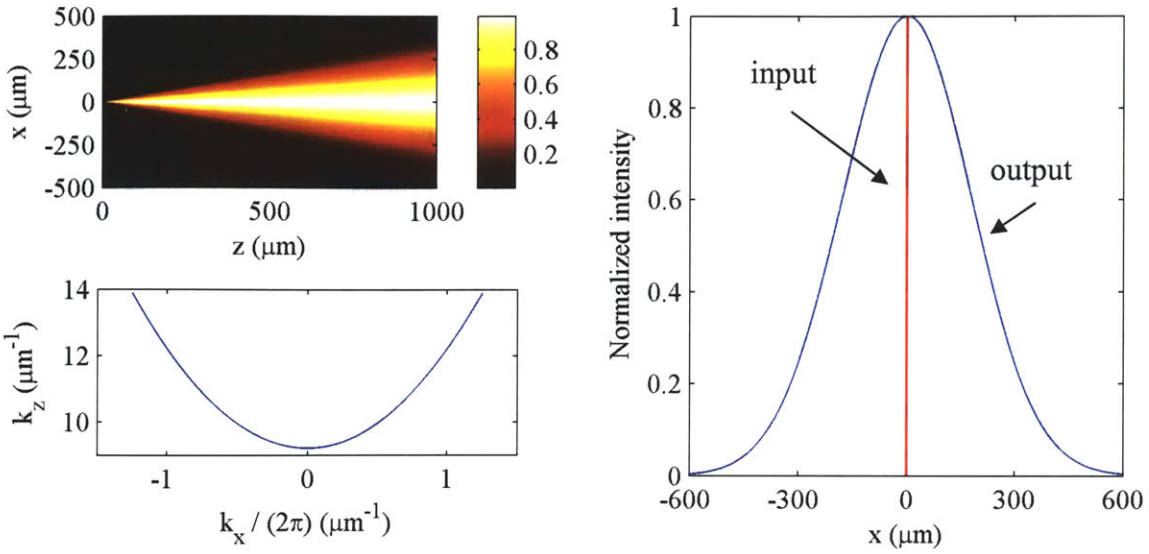

Figure 3.9 – Simulated propagation of a Gaussian beam under contour Ω_5: *(left top)* computed image over a 1 mm propagation, *(left bottom)* computed equifrequency contour and *(right)* input and output transverse beam profiles in the PhC.

At this point, the first two regimes are familiar, but the fringe-like regime is not clear. A transverse interference pattern seems to form as the beam propagates. This behavior is considered in the next subsection.

3.2.2 Beating Patterns

To better understand the fringe-like regime, two other dispersion surfaces of the functional form given by equations (3.36) are considered. These are chosen because they represent flatter curves, while still conserving the double-hump shape of contour Ω_3.

$$\begin{aligned} \Omega'_3: \quad & k_z = k - \frac{1}{2}\mathrm{a}\,k_x^2 + 5\mathrm{b}\,k_x^4 \\ \Omega''_3: \quad & k_z = k - \mathrm{a}\,k_x^2 + 5\mathrm{b}\,k_x^4 \end{aligned} \tag{3.36}$$

where $b = a^2 = (2\pi)^{-4}$.

New simulations are performed, and Figure 3.10 presents the results for the contour Ω'_3.

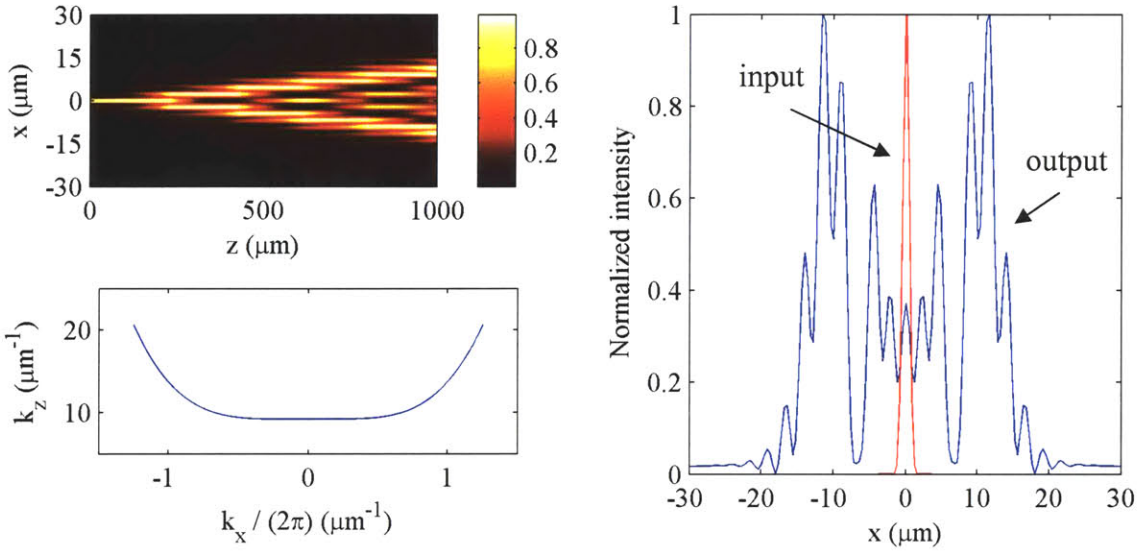

Figure 3.10 – Simulated propagation of a Gaussian beam under contour Ω'_3: *(left top)* computed image over a 1 mm propagation, *(left bottom)* computed equifrequency contour and *(right)* input and output transverse beam profiles in the PhC.

Here the transverse fringe pattern is more visible. The interference period L_x is about 2.4 μm, measured from the figure. This pattern is due to the different k_x (transverse) components of the wavevectors at the local max/min points of the contour[26]. Particularly, the Ω_3 family of contours has three points where the gradient is in the k_z direction –Figure 3.11. If the input beam is able to excite those specific wavevectors, i.e., if $\Delta k_x \geq k_m$, then interference occurs.

For the Gaussian function, the relation between the beam waist radius W_0 and the wavevector spread Δk_x is:

$$W_0 \,.\, \Delta k_x \simeq 2 \tag{3.37}$$

where Δk_x is the radius at which the transverse wavevector intensity profile drops to $1/e^2$ of its maximum value – Figure 3.12.

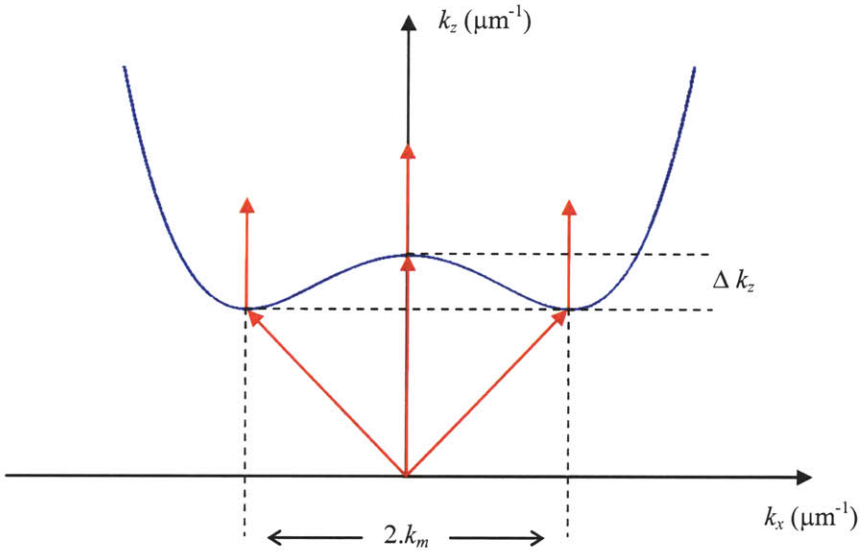

Figure 3.11 – Origin of the interference patterns seen in the Ω_3 family of contours. The allowed wavevectors have different transverse and longitudinal components, which give origin to interference.

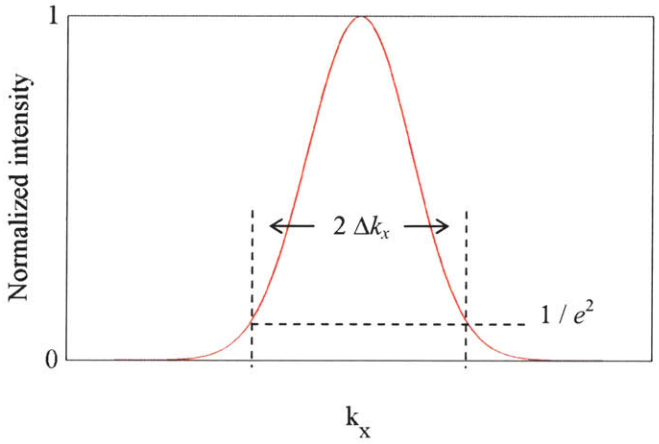

Figure 3.12 – Definition of the transverse wavevector spread Δk_x.

There will also be interference in the longitudinal direction due to the different values of the k_z (longitudinal) components. This is simulated in Figure 3.13, for contour Ω''_3.

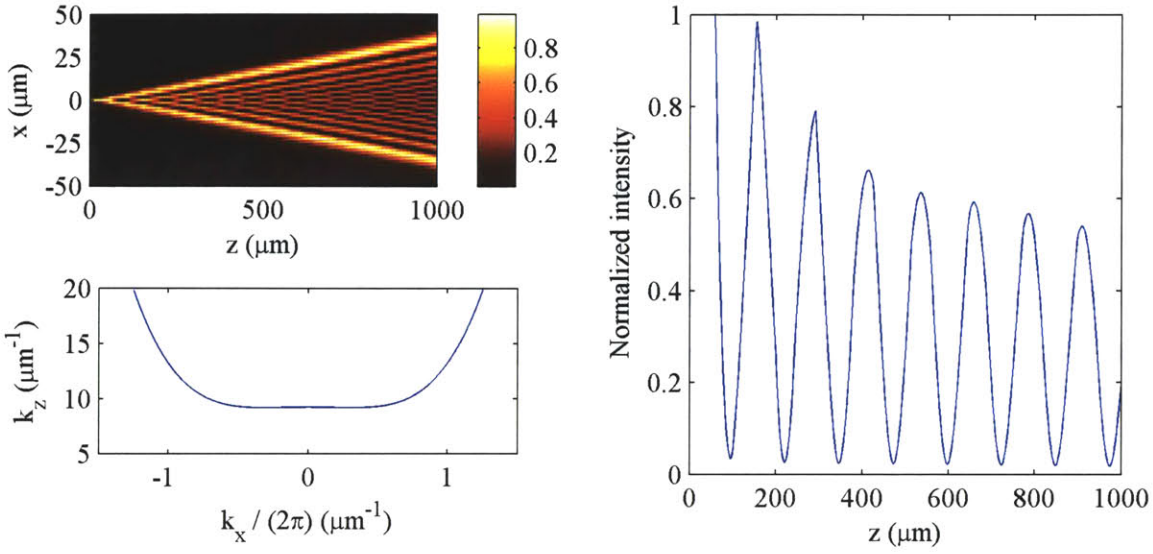

Figure 3.13 – Simulated propagation of a Gaussian beam under contour Ω''_3: *(left top)* computed image over a 1 mm propagation, *(left bottom)* computed equifrequency contour and *(right)* scan of the image along the z axis showing longitudinal beating.

The period L_z of the longitudinal beating pattern is about 125.7 μm. k_m and Δk_z are calculated from expressions (3.36), at the points where the first derivative is zero:

$$\begin{aligned} k_m &= \frac{\pi}{\sqrt{5}} \qquad (\text{for } \Omega'_3) \\ \Delta k_z &= \frac{1}{20} \qquad (\text{for } \Omega''_3) \end{aligned} \tag{3.38}$$

which give fringe periods of

$$L_{x,1} = \frac{2\pi}{k_m} = 4.5\ \mu\text{m} \qquad (\text{for } \Omega'_3)$$

$$L_{x,2} = \frac{2\pi}{2k_m} = 2.2\ \mu\text{m} \qquad (\text{for } \Omega'_3) \tag{3.39}$$

$$L_z = \frac{2\pi}{\Delta k_z} = 125.7\ \mu\text{m} \qquad (\text{for } \Omega''_3)$$

These values are consistent with the ones measured from the plots. The value $L_{x,2}$ corresponds to the one measured from Figure 3.10, and the value $L_{x,1}$ is just a double spatial frequency pattern shaded in the envelope of the first higher frequency pattern. Furthermore, the fanning-like pattern (more visible in Figure 3.13) is due to the simultaneous effect of both transverse and longitudinal interferences.

3.2.3 Angle of Spreading for the Ω_3 Contours

Another peculiar characteristic of the Ω_3 family of contours is that the diffracted beam has a very well defined sharp edge. Looking again at the dispersion contour Ω_3, in Figure 3.14, it is seen that the angle of spreading has a maximum value of θ_{max}. This angle is determined by the slope of the contour at the inflection points and it defines the sharp edge of the diffracted beam. This is very clear in Figure 3.7, where the measured angle θ is about 10.7°. The theoretical value of θ_{max} is entirely determined by the equifrequency contours, and is calculated to be ~9.9° (from the expression for Ω_3, in (3.34)).

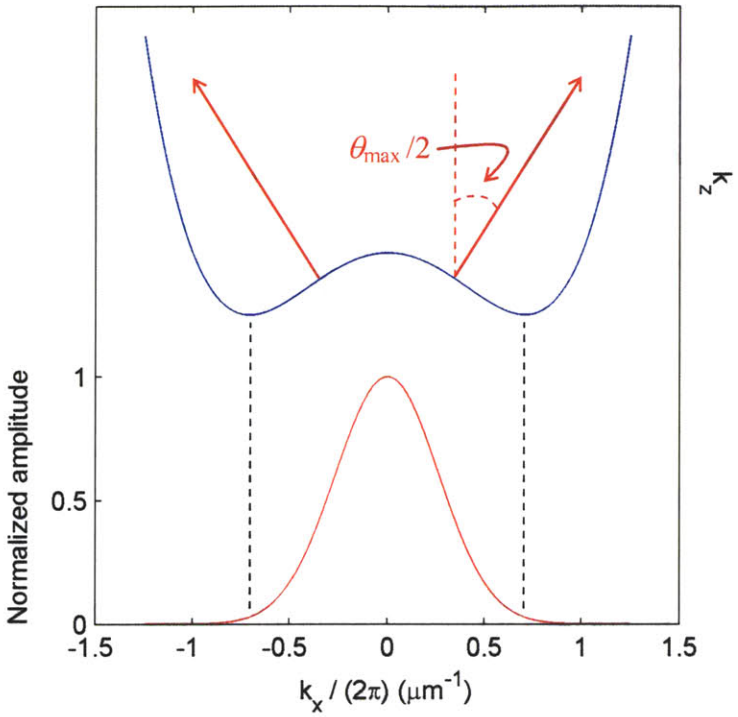

Figure 3.14 – Contour Ω_3 and Fourier transform of the input amplitude, illustrating the maximum spread angle θ_{max}. This angle is determined by the slope of the curve at the inflection points.

Figure 3.14 also shows that the local minima of the contour are slightly excited, allowing for interference to occur, as described in subsection 3.2.2.

When the input beam is wider, the excited spread of transverse wavevectors is smaller and the beam will only sense the center region of the contour. As a result, no interference pattern is observed, and the spreading angle θ may be lower than θ_{max}. This situation is illustrated in Figure 3.15, where the input beam waist radius is $W_0 = 2\ \mu m$ (as opposed to 0.85 μm), for the same contour Ω_3. The spreading angle θ is now ~8°.

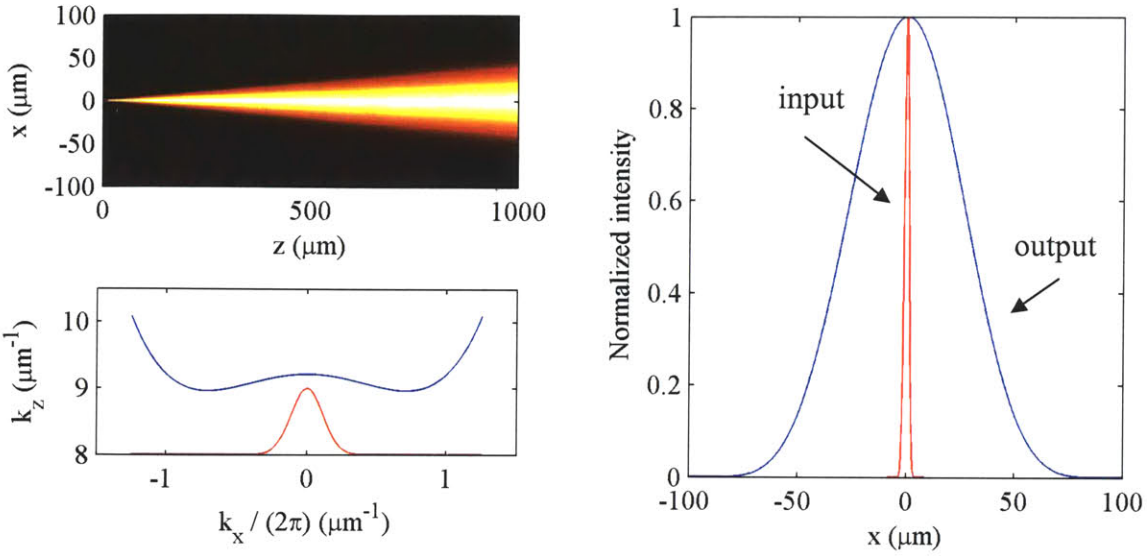

Figure 3.15 – Simulated propagation of a Gaussian beam under contour Ω_3 with an input waist radius of 2 μm: *(left top)* computed image over a 1 mm propagation, *(left bottom)* computed equifrequency contour and Fourier transform of the input (amplitude, in arbitrary units), and *(right)* input and output transverse beam profiles in the PhC. Here, the spreading angle θ is around 8°.

3.2.4 Linear and Periodic Input Phase

All the results shown until this point use an input Gaussian beam without any initial phase ϕ – in equation (3.35). To take into account the possibility of having an input facet not perpendicular to the direction of super-collimation (due to errors in the fabrication), or having the input fiber probe misaligned, a linear phase shift is added to the input beam – Figure 3.16*(a)*. This is equivalent to shifting the transverse wavevector profile along k_x, which may result in a different overlap with the equifrequency contour and, consequently, change the evolution of the beam inside the PhC. The phase term used in the simulation is

$$\phi = 0.1 \frac{2\pi n}{\lambda_0} x \tag{3.40}$$

where $n = 2.2$. This phase shift corresponds to a misalignment angle of ~5.7° between the coupling direction and the Γ-M direction.

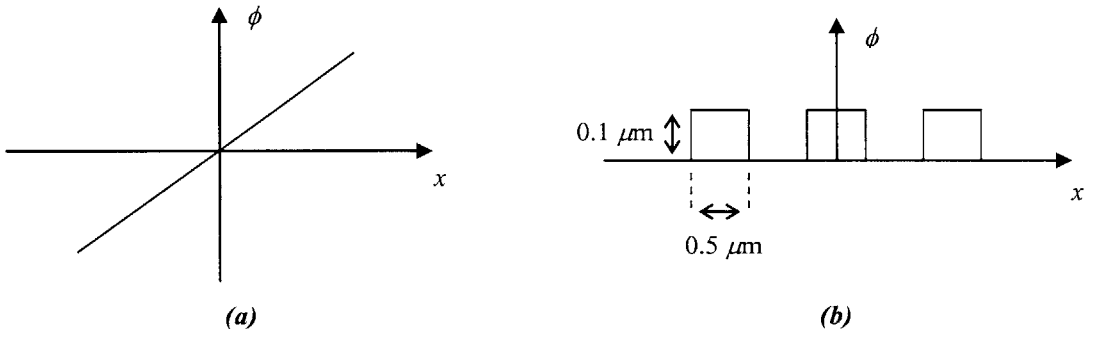

Figure 3.16 – Phase shift added to the input Gaussian beam: *(a)* linear phase and *(b)* periodic phase.

The phase shift will not have any influence under the ideal flat contour, but it changes the beam shape for the remaining contours. Figure 3.17 and Figure 3.18 simulate two of these cases (contours Ω''_3 and Ω_4).

In both cases the propagating beam is influenced by the additional phase shift at the input. The global effect is an asymmetric delocalization of the field in the transverse direction, i.e., the radiation seems to be steered towards $-x$, while less localized in the $+x$ direction. This is very clear in Figure 3.17.

As mentioned, the linear phase shift corresponds to a displacement of the transverse wavevector profile along k_x, resulting in a different overlap with the dispersion surface. This idea is illustrated in Figure 3.19.

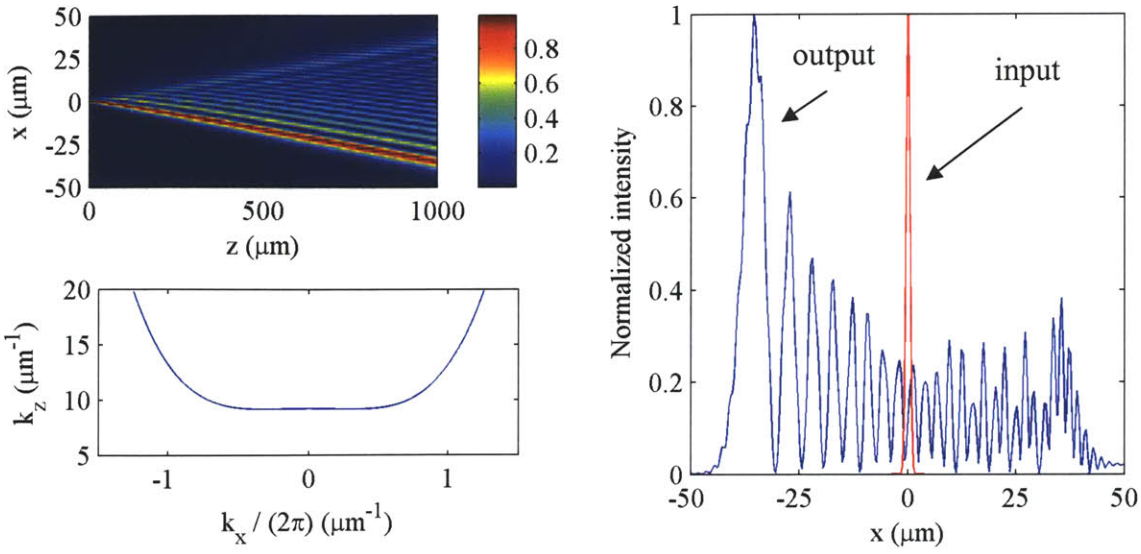

Figure 3.17 – Simulated propagation of a Gaussian beam under contour Ω''_3 with a linear phase shift at the input: *(left top)* computed image over a 1 mm propagation, *(left bottom)* computed equifrequency contour and *(right)* input and output transverse beam profiles in the PhC.

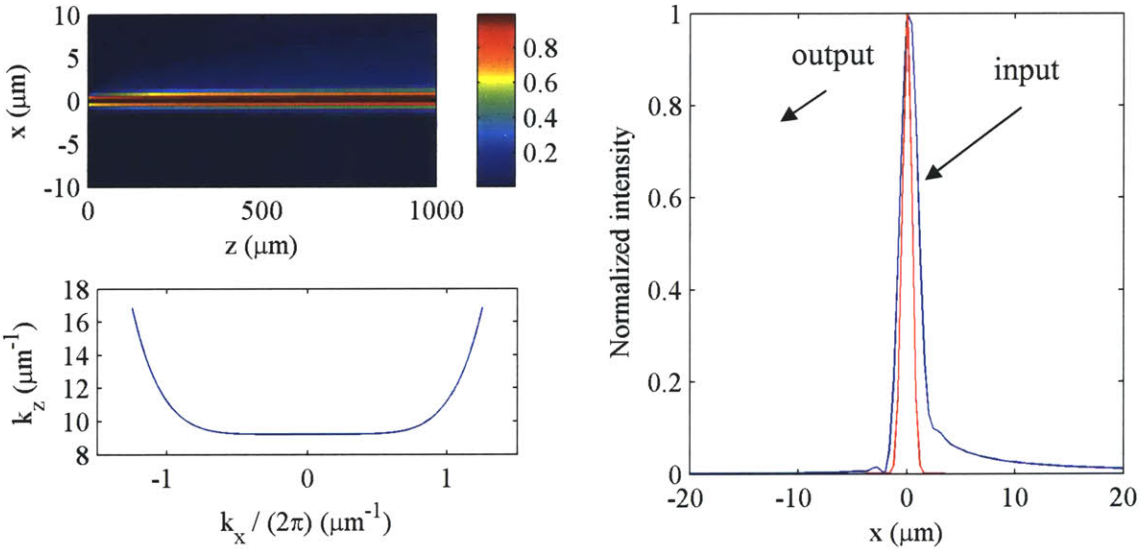

Figure 3.18 – Simulated propagation of a Gaussian beam under contour Ω_4 with a linear phase shift at the input: *(left top)* computed image over a 1 mm propagation, *(left bottom)* computed equifrequency contour and *(right)* input and output transverse beam profiles in the PhC.

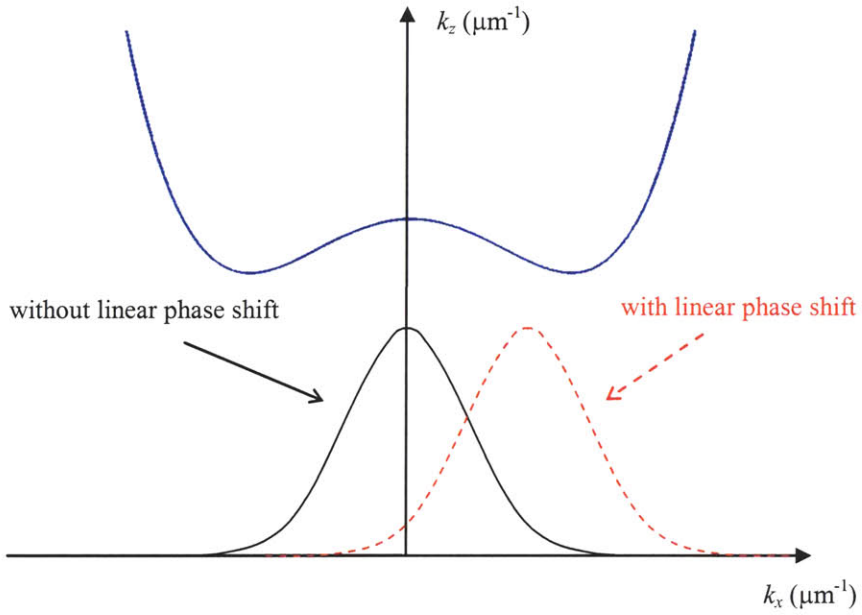

Figure 3.19 – The addition of a linear phase shift at the input has the effect of shifting the transverse wavevector profile, shifting the overlapping region with the equifrequency contour as well.

One step further in this analysis is to consider a periodic phase shift of the form depicted in Figure 3.16*(b)*. The results are presented in the next figures, using the same input Gaussian beam amplitude and considering propagation through the different equifrequency contours (Ω_1 to Ω_5).

This set of simulations was performed with slightly different parameters:

- $z_{out} = 100\ \mu m$
- $\Delta z = 0.5\ \mu m$
- $\Delta x = 0.5\ \mu m$

This change is not critical and similar results would be obtained with the previous parameters.

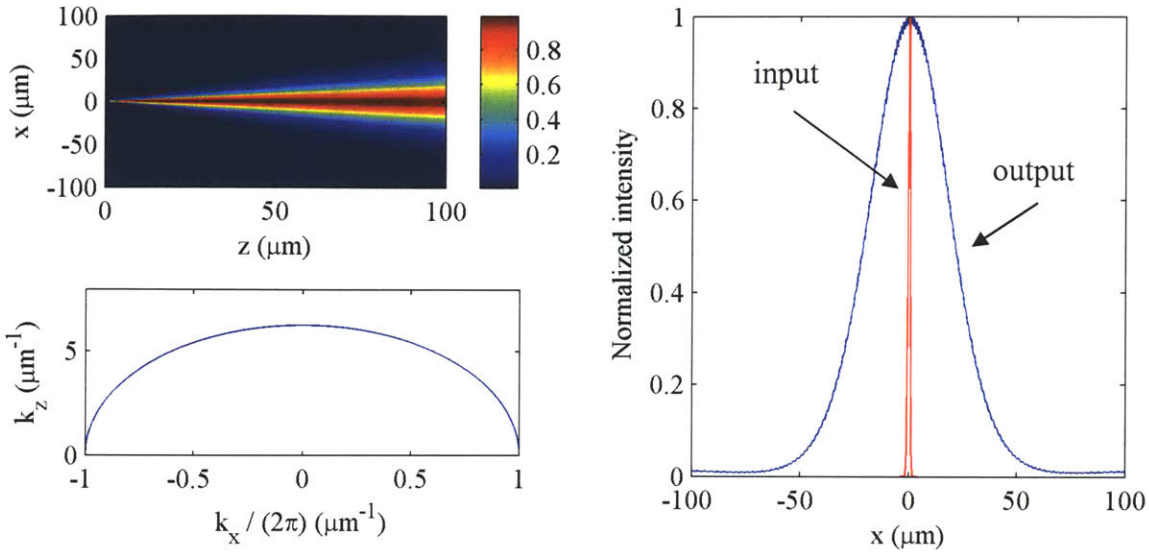

Figure 3.20 – Simulated propagation of a Gaussian beam under contour Ω_1 with a periodic phase shift at the input: *(left top)* computed image over a 100 μm propagation, *(left bottom)* computed equifrequency contour and *(right)* input and output transverse beam profiles in the PhC.

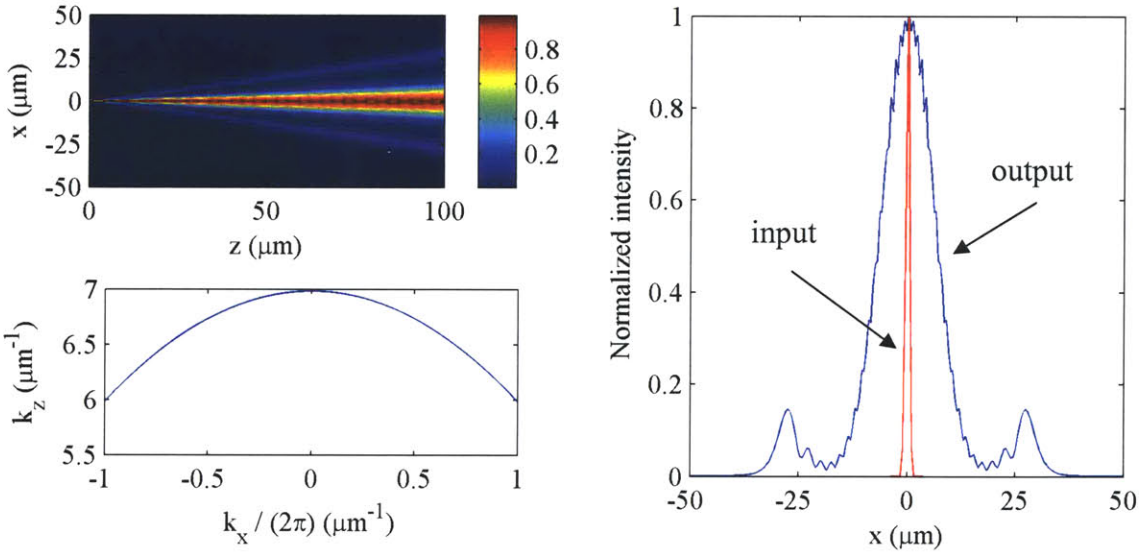

Figure 3.21 – Simulated propagation of a Gaussian beam under contour Ω_2 with a periodic phase shift at the input: *(left top)* computed image over a 100 μm propagation, *(left bottom)* computed equifrequency contour and *(right)* input and output transverse beam profiles in the PhC.

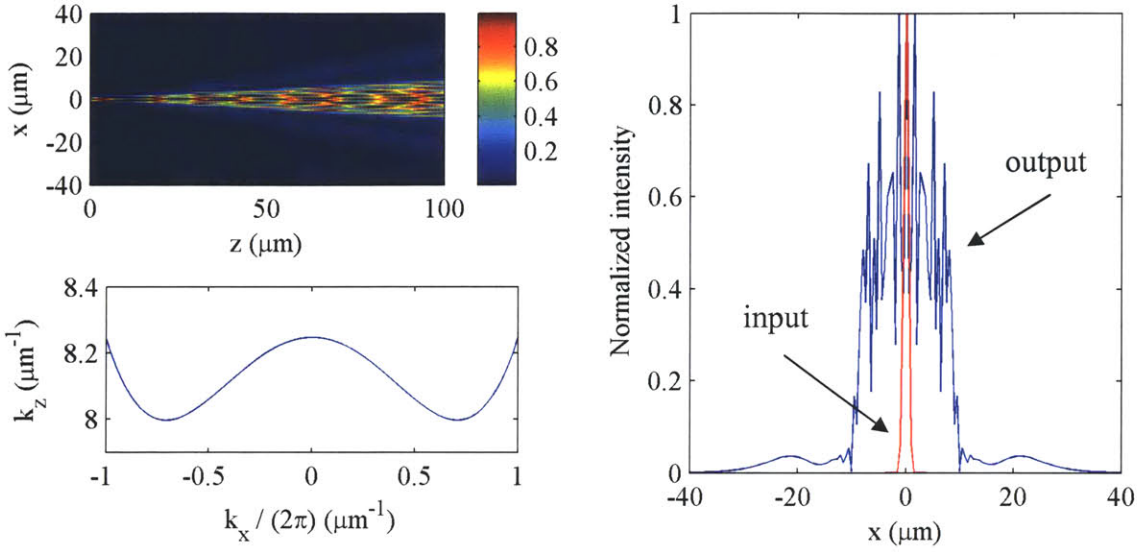

Figure 3.22 – Simulated propagation of a Gaussian beam under contour Ω_3 with a periodic phase shift at the input: *(left top)* computed image over a 100 μm propagation, *(left bottom)* computed equifrequency contour and *(right)* input and output transverse beam profiles in the PhC.

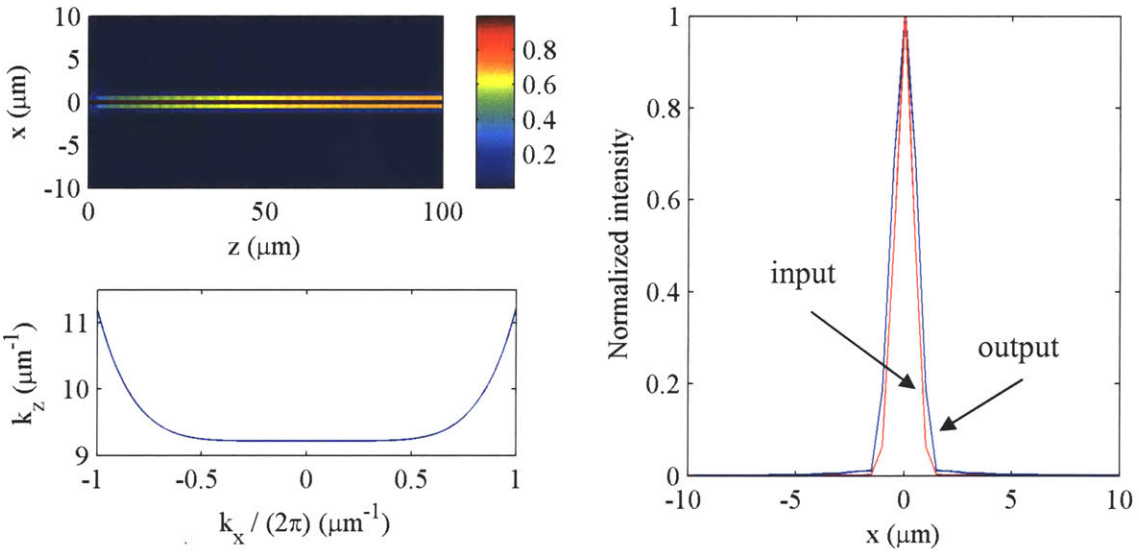

Figure 3.23 – Simulated propagation of a Gaussian beam under contour Ω_4 with a periodic phase shift at the input: *(left top)* computed image over a 100 μm propagation, *(left bottom)* computed equifrequency contour and *(right)* input and output transverse beam profiles in the PhC.

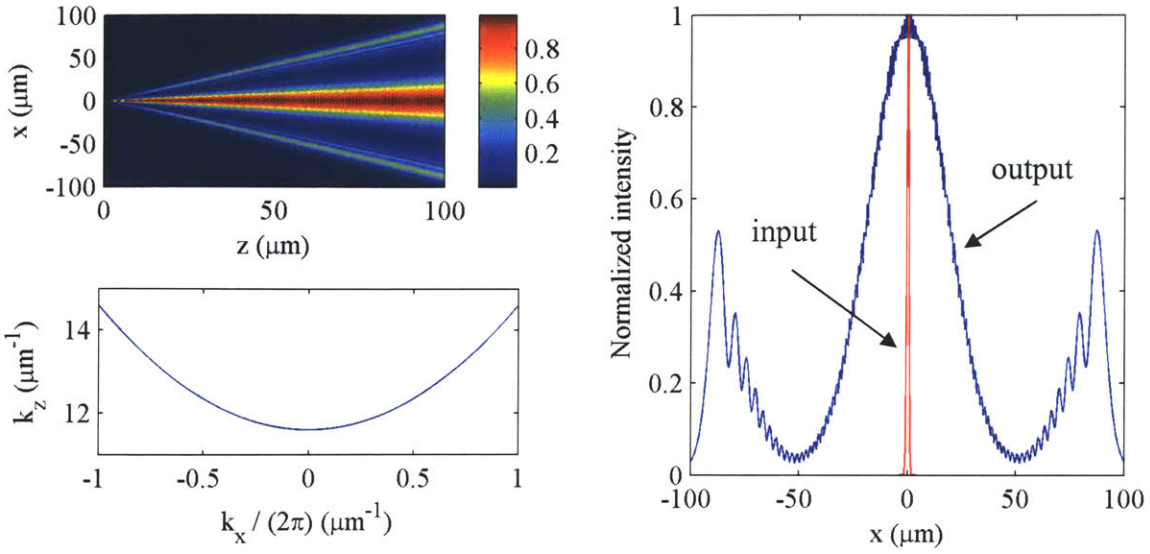

Figure 3.24 – Simulated propagation of a Gaussian beam under contour Ω_5 with a periodic phase shift at the input: *(left top)* computed image over a 100 μm propagation, *(left bottom)* computed equifrequency contour and *(right)* input and output transverse beam profiles in the PhC.

Also, until now, the wavelength and the effective index were assumed to be constant ($\lambda_0 = 1.5$ μm and $n = 2.2$). In reality, these values are different for the different contours, and here they were considered, in order to correctly take into account the periodicity of the phase shift – Table 3.1.

	Ω_1	Ω_2	Ω_3	Ω_4	Ω_5
λ_0 (μm)	1.9	1.8	1.6	1.5	1.3
n	1.9	2.0	2.1	2.2	2.4

Table 3.1 – Values of the wavelength and effective index used for each different contour.

The main additional effect observed is the fanning of the beam as it propagates. Figure 3.25 depicts the shape of the transverse wavevector profile with the periodic phase shift, which is symmetric.

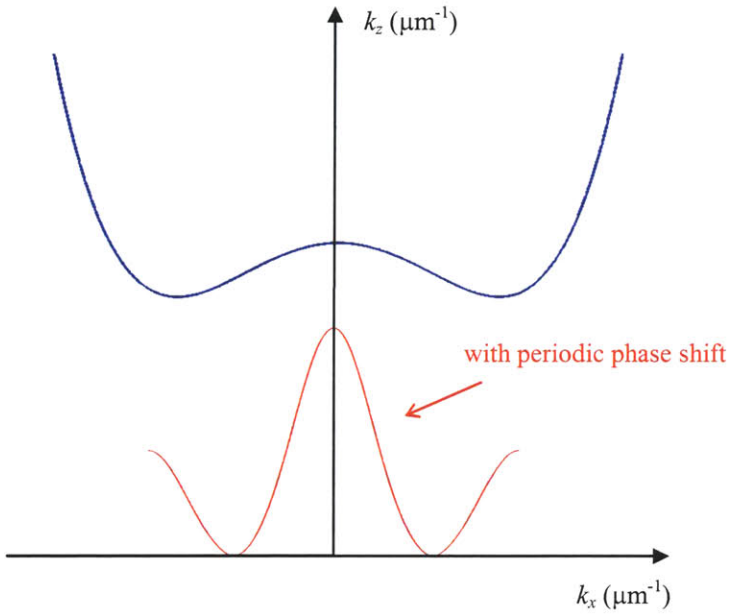

Figure 3.25 – The periodic phase shift at the input changes the shape of the transverse wavevector profile, which is now overlapping with the equifrequency contour at different positions, compared to the case with linear phase.

The main lobe of the transverse wavevector profile is responsible for the central part of the beam, while the two side lobes give origin to fanning. This periodic phase shift has no effect under the ideal flat contour. It is observed that the fanning effect is stronger for frequencies closer to the bandgap (higher energies, shorter wavelengths).

If both linear and periodic phase shifts are considered together, the observed beam will simultaneously show fanning and steering. Figure 3.26 shows this simulation.

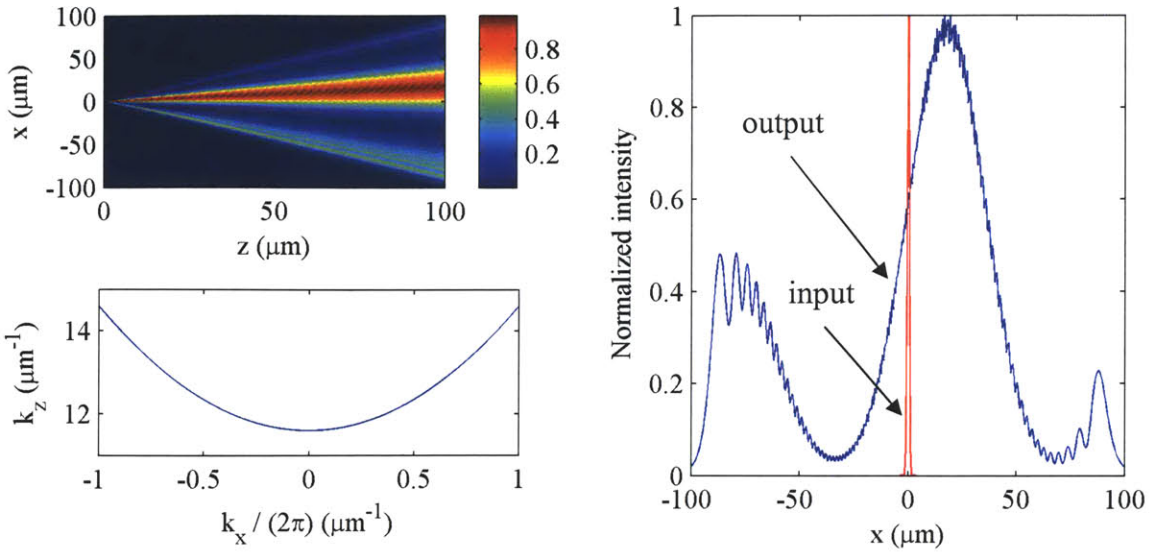

Figure 3.26 – Simulated propagation of a Gaussian beam under contour Ω_5, with both linear and periodic phase shifts at the input: *(left top)* computed image over a 100 μm propagation, *(left bottom)* computed equifrequency contour and *(right)* input and output transverse beam profiles in the PhC.

3.2.5 Minimum Beam Size Supported by the PhC

Now that some basic understanding on how the dispersion surface affects the beam evolution has been developed, and in order to complete this section, the behavior of the real PhC under study is examined. Some considerations about the width $2.k_L$ (as defined in Figure 2.7), over which the contour is flat, are made. The motivation for this study is the fact that the collimated beam shown in Figure 3.8 is slightly broader at the output, compared to the input profile. In fact, as will be seen, this effect is also a result of the contour shape and the excited spread of transverse wavevectors. The finite width of the contour over which the dispersion is flat, shown in Figure 3.27, determines the minimum size of the allowed beam inside the PhC:

$$(W_0)_{\min} \simeq \frac{2}{k_L} \tag{3.41}$$

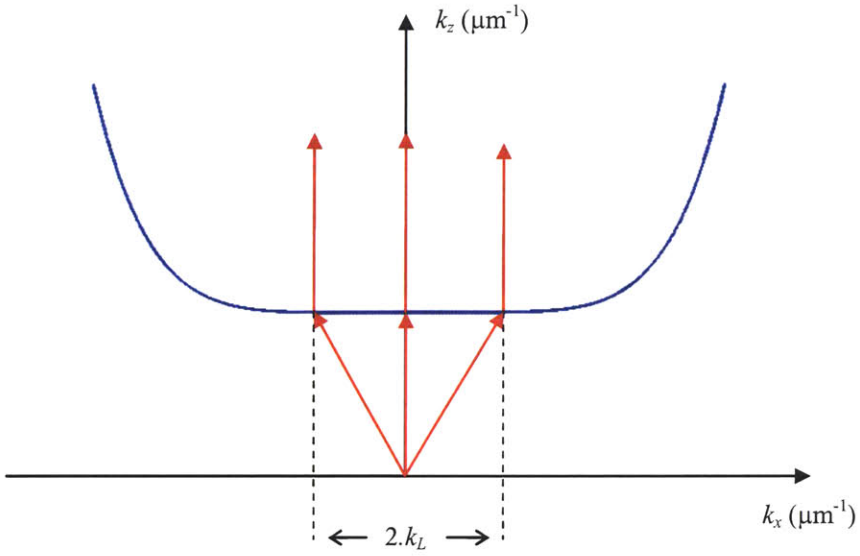

Figure 3.27 – The width of the flat region of the equifrequency contour determines the minimum allowed spot size inside the structure.

In order to obtain results closer to the real experimental PhC, a new simulation was performed. The beam is now propagating over 5 mm, under an equifrequency contour with narrower width (than in the previous simulations), which was extracted directly from the experimental contours. The general parameters are now:

- $z_{in} = 0$
- $z_{out} = 5000\ \mu m$
- $\Delta z = 50\ \mu m$
- $x_{min} = -1000\ \mu m$
- $x_{max} = 1000\ \mu m$
- $\Delta x = 0.05\ \mu m$
- $n = 2.2$ (effective index)
- $\lambda_0 = 1.5\ \mu m$
- $W_0 = 0.85\ \mu m$

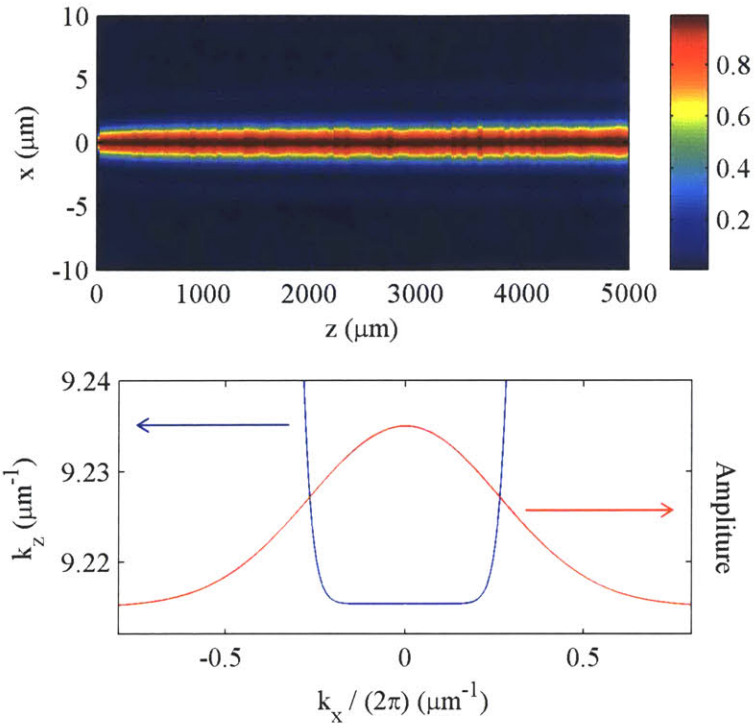

Figure 3.28 – Simulated propagation of a Gaussian beam under an experimental-based contour: *(top)* computed image over 5 mm and *(bottom)* computed equifrequency contour and Fourier transform of the input.

Figure 3.28 shows the intensity image formed by the beam and the shape of the contour used in the simulation. k_L is now ~1 μm^{-1}, yielding a minimum allowed beam spot size ($2W_0$) inside the PhC of about 4 μm. It is seen that a great region of the transverse wavevectors fall outside the flat region of the contour, and therefore are not allowed to exist inside the structure. These components will be lost because the region of the contour which they see is not flat. Figure 3.29 presents the transverse profiles of the beam at several positions along the direction of propagation. From here it is clear that the beam size is conserved as it propagates along the crystal, and that the 1.7 μm beam is not allowed inside this PhC. The transition from the 1.7 μm input beam to the 4 μm allowed beam happens after a short distance, observed to be less than 10 discretization steps Δz

(in this case). The contour used in this simulation gives good results for long samples but may not be the best for simulating short distances. In this case the exact experimental contour should be used instead.

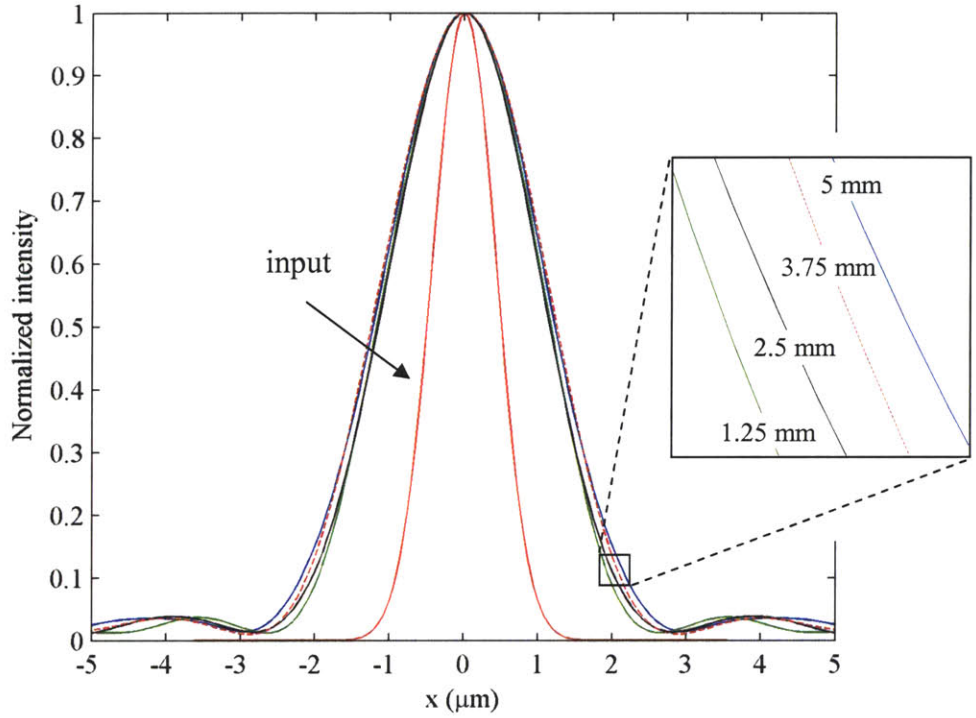

Figure 3.29 – Transverse beam profiles from Figure 3.28*(top)*, for different propagation distances.

From this simulation it is also visible that some side lobes appear and propagate along the whole structure. The transverse profile of the beam resembles a sinc function. This shape makes sense because now the transverse wavevector distribution can be interpreted as the product of the initial Gaussian with a rectangular function (which Fourier transform is a sinc function).

3.2.6 Main Results from the Simulations

Summarizing, the numerical simulations indicate very different behaviors for dispersion curves away from the super-collimation regime. The spreading angle is determined by the equifrequency contour and by the excited spread of transverse wavevectors. Fanning and beam steering are possible under certain conditions – e.g. with phase shift at the input. The behavior of the PhC is quite different from that of an isotropic medium, where the diffraction angle only depends on the properties (range of transverse wavevectors) of the input beam. When operating under a contour with three local extrema points (the double-hump shape), interference patterns may occur. The allowed minimum beam dimension inside the PhC is imposed by the shape of the contour. This means that not all input excitations are guaranteed to be supported by the structure, even in the super-collimation regime. Another important issue is the fact that the crystal has a very large area, and small variations in the slab thickness or hole size along the crystal may shift the contour shape for a specific wavelength, resulting in a mix of the effects seen for each one of the individual contours. The results obtained in this section (3.2) will be useful to compare with the experimental data presented in the next chapter.

4

DEMONSTRATION OF THE SUPER-COLLIMATION EFFECT IN A PLANAR 2D PHC

The previous chapters introduced the concept of super-collimation and presented several simulation results. In the current chapter, the experimental procedure and results are described.

4.1 The PhC Device

The device under study is a 2D photonic crystal slab with a square lattice of holes in air – Figure 4.1. The PhC was fabricated by Sheila N. Tandon, in a large-area

silicon-on-insulator (SOI) wafer, through interferometric lithography (IL), using a 325 nm HeCd laser line in a Lloyd's mirror configuration[47].

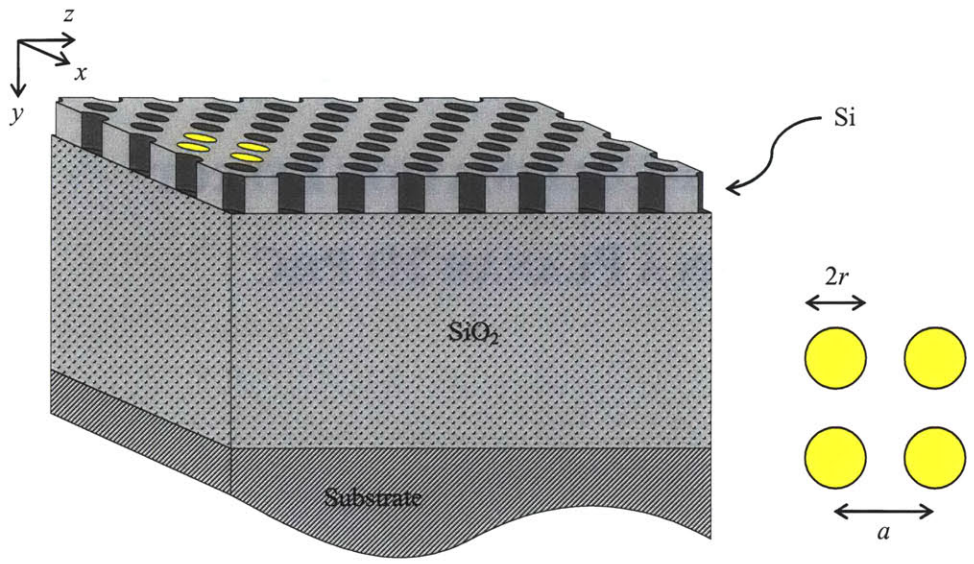

Figure 4.1 – The device under study is a square lattice PhC of holes in air. *a* is the lattice constant and *r* the hole radius.

The SOI wafer consists of a ~205 nm layer of silicon over a 3 μm layer of SiO_2, and a substrate. In the vertical direction, light is confined by total internal reflection (asymmetric silicon waveguide with an air over-cladding and a SiO_2 under-cladding). The patterning of the PhC was performed through two IL exposures rotated by 90°. The pattern was then transferred into a SiO_2 hard mask layer and onto the 205 nm Si layer via reactive ion etching (with both CF_4 and Cl_2 dry etches).

The PhC was designed to operate in the 1.5 μm wavelength range for the TE-like radiation (electric field parallel to the 2D plane), in the lowest energy band and close to the edge of the bandgap. The lattice constant is $a = 350$ nm and the hole radius is $r = 0.3a$. Figure 4.2 shows a scanning electron micrograph (SEM) image of the fabricated sample.

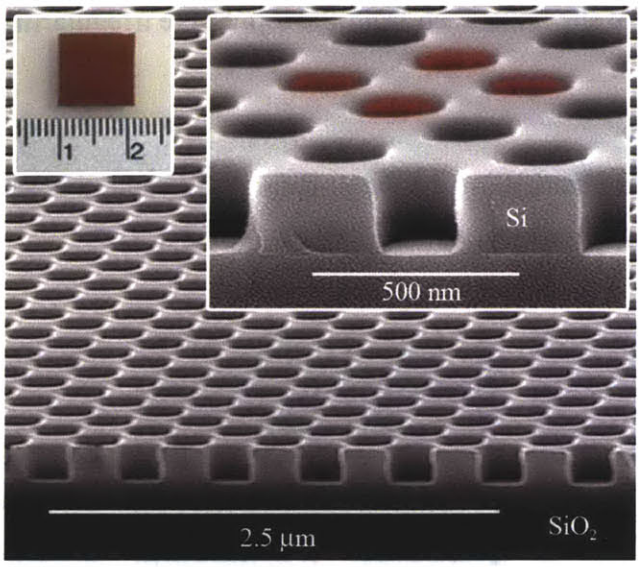

Figure 4.2 – SEM image of a sample showing the cross-section of the PhC, the square lattice (in red), and a photo of one of the fabricated samples (Courtesy of S. N. Tandon).

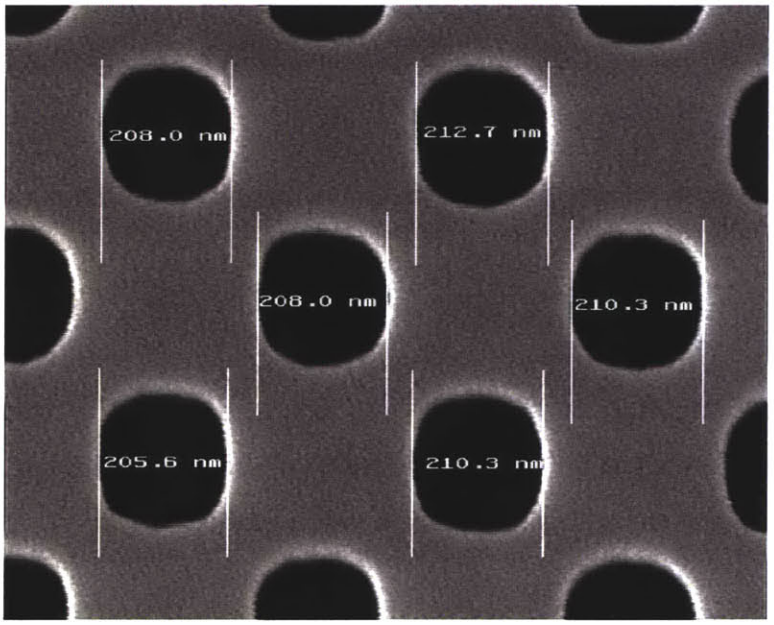

Figure 4.3 – Top view SEM image of the holes showing a diameter of about 210 nm (Courtesy of S. N. Tandon).

The holes are close to circular, and the diameter is about 210 nm. Figure 4.3 shows a SEM image of the holes seen from the top. Some irregularities due to fabrication are observed.

IL enables the fabrication of large-area PhCs, and the samples used in this experiment have centimeter-scale dimensions – Figure 4.4.

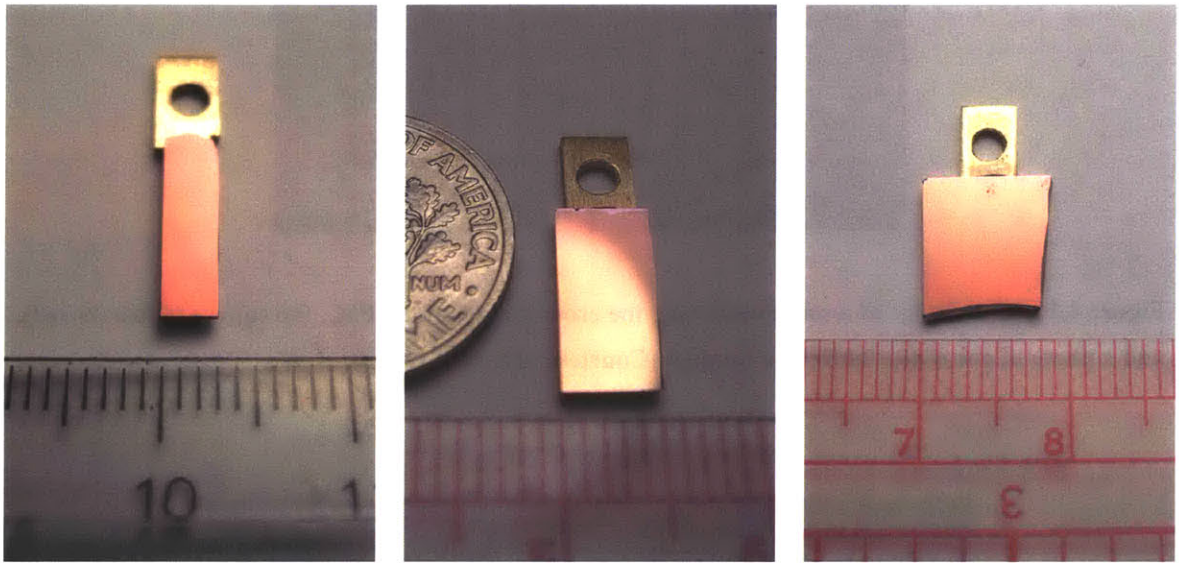

(a) *(b)* *(c)*

Figure 4.4 – Photos of the samples used in the experiment: *(a)* 3 mm, *(b)* 5 mm and *(c)* 8 mm.

The band structure of the PhC was computed using a frequency-domain eigenmode solver[48], with $n(Si) = 3.5$ and $n(SiO_2) = 1.45$. The resulting equifrequency contours for the lowest energy band are shown in Figure 4.5.

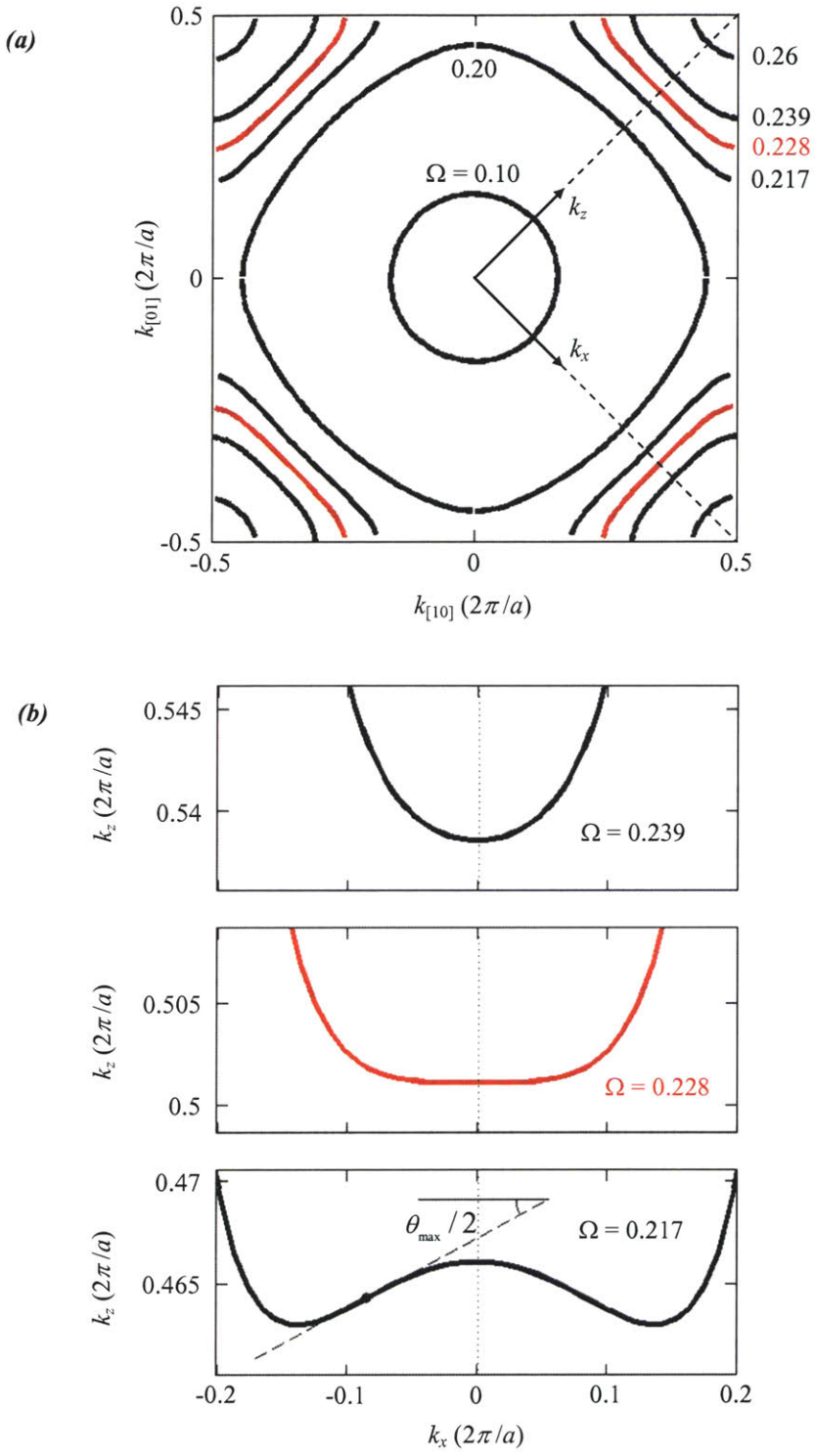

Figure 4.5 – Equifrequency contours obtained from the band structure calculation of the PhC: *(a)* contours for the first band and *(b)* detailed view for the frequencies near the flat curve ($\Omega = 0.228$) (Courtesy of M. Ibanescu).

As described before, the equifrequency contours are very different from the circular dispersion surfaces obtained for isotropic materials. There is a flat region along the Γ-M symmetry direction, allowing super-collimation. This contour corresponds to the normalized frequency of $\Omega = 0.228$, or equivalently, to $\lambda_0 = 1535$ nm, and the flatness extends over a spread of transverse wavevectors of about $\pm 1\ \mu m^{-1}$. This number sets the minimum spot size of the allowed beam inside the PhC to ~4 μm, calculated from equation (3.41). Later it is shown that the actual size of the beam propagating inside the PhC is about 3.4 μm, so this last value will be referred to as the "expected value".

For wavelengths above and under the ideal regime, the contours are very different. In particular, for $\Omega = 0.217$, the contour has a double-hump shape, which will lead to interference effects and a maximum spreading angle θ_{max}, as discussed in chapter 3.

The effective index n seen by the light propagating along the Γ-M direction depends on the frequency. For $\Omega = 0.228$, $k_z \simeq 0.50107\,(2\pi/a)$, which gives

$$n = \frac{k_z \lambda_0}{2\pi} = \frac{k_z a}{2\pi\,\Omega} \simeq \frac{0.50107}{0.228} = 2.1977 \tag{4.1}$$

This ($n = 2.2$) was the value used for most of the simulations in chapter 3. For different curves, the effective index changes and is calculated from the longitudinal wavevector component k_z and the frequency (or wavelength) correspondent to the contour.

In calculating the band diagram of the PhC, it is assumed that the structure is ideal, i.e., that the holes and periodicity are perfect. This may not be the case for the real structure, and small offsets to the predicted regimes may occur. Furthermore, problems associated with the cleave of the facets and roughness of the holes (due to fabrication) may present additional sources of loss, adding to the intrinsic (and measurement) losses.

4.2 Experimental Setup and Procedure

In order to study the spatial evolution of a beam propagating inside the PhC under the different equifrequency contours, a localized Gaussian beam was excited at the input through a high numerical aperture (NA) lensed fiber with a 1.7 μm spot size. To sense the different contours from Figure 4.5, a tunable laser (1430-1515 nm and 1510-1610 nm) is used to set the wavelength and a polarization controller sets the TE polarization at the input. The complete experimental setup is outlined in Figure 4.6. A photo of the lab apparatus is also shown - Figure 4.7.

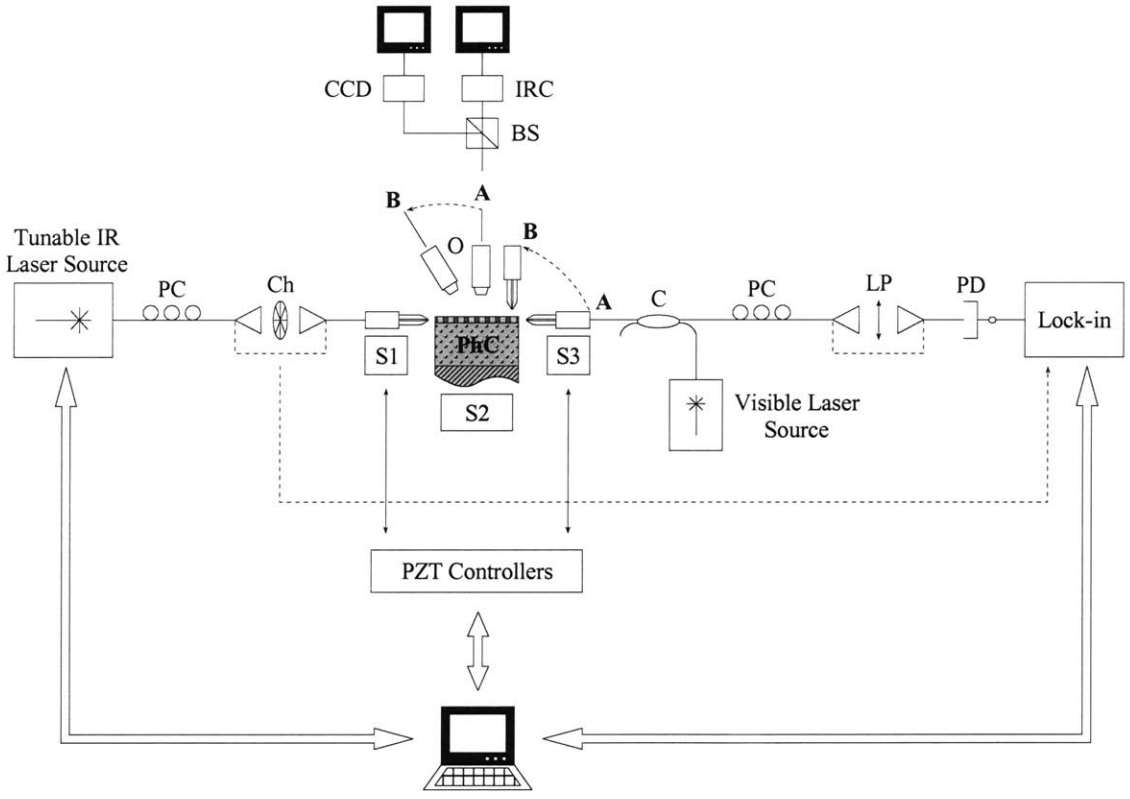

Figure 4.6 – Experimental setup used to study the super-collimation effect in a 2D PhC. PC – polarization controller; Ch – chopper; S1, S2 and S3 – micropositioning stages; O – microscope objective; C – coupler; BS – beam splitter; CCD – visible camera; IRC – infrared camera; LP – linear polarizer; PD – photodetector.

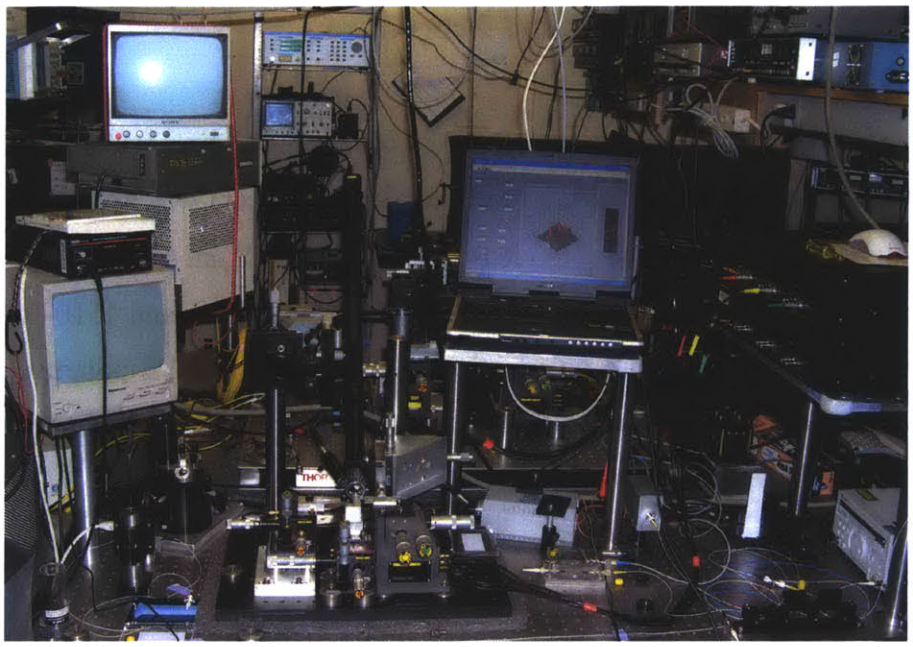

Figure 4.7 – Photo of the experimental apparatus built to study the super-collimation effect in a 2D PhC, showing the main blocks.

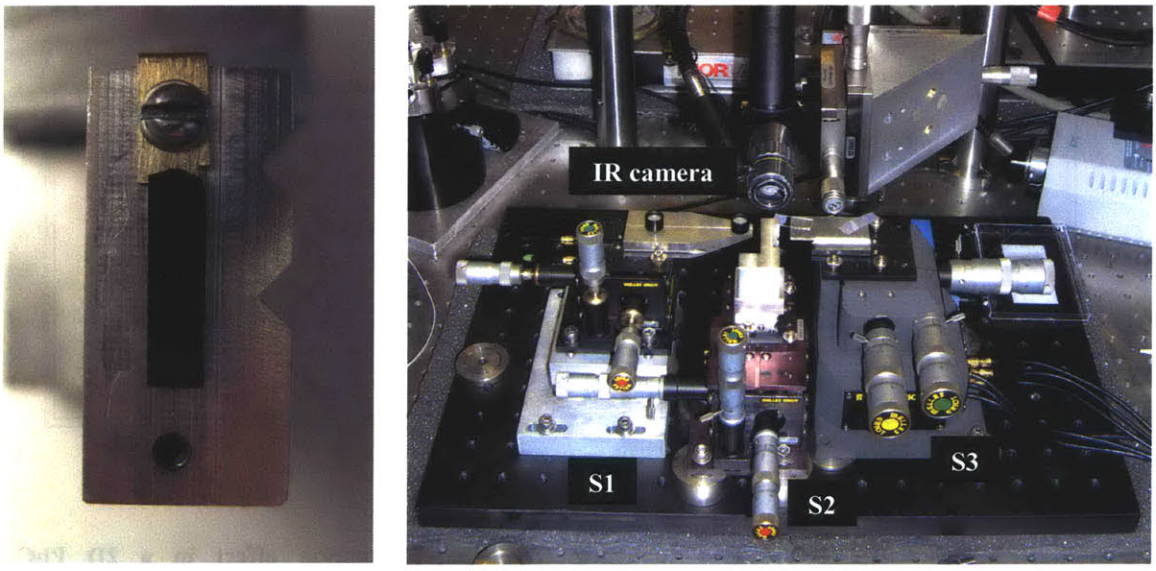

(a) *(b)*

Figure 4.8 – Details of the experimental setup: *(a)* PhC sample attached to a metal holder with crystal-bond wax. This holder is then mounted on a 4-axis micropositioning stage S2, allowing precise position control. *(b)* PZT micropositioning stages S1, S2 and S3.

Light from a tunable infrared (IR) laser is coupled into the PhC through a lensed fiber, after passing through a chopper, at a frequency around 2 kHz. A polarization controller (PC) sets the input polarization to either TE or TM. Precise coupling is achieved with a 3-axis micropositioning stage (S1) and piezoelectric (PZT) controller, programmed in LabView® through a General Purpose Interface Bus (GPIB). The fiber-PhC coupling efficiency is about 15%. The PhC sample is mounted on a metal holder with crystal-bond wax – Figure 4.8*(a)* – and attached to a 4-axis stage (S2) – Figure 4.8*(b)* – allowing precise control over its position and tilt angle.

The beam inside the PhC is measured from the top with an IR camera, which detects the scattered light as the beam propagates along the crystal (Figure 4.8*(b)*). A CCD camera is also used for visible alignment purposes. The light reaching the end facet of the crystal is detected by a second lensed fiber that is scanned in 2D (by S3) at the output, producing a high-resolution confocal image of the beam profile. The scanning program is run from LabView®. This configuration is represented by position **A** in the schematics of Figure 4.6. Another way of monitoring the light as it propagates inside the crystal is through a contact-mode near-field scanning optical microscopy (NSOM) technique. In this case, a lensed fiber is scanned over the surface – position **B** – and senses the near-field of the beam. Figure 4.9 shows the experimental implementation of the probe for the contact NSOM measurements.

The light collected by the probe may have TM components due to scattering conversion or mode mismatch between the input probe and the PhC, so a second PC and a linear polarizer (LP) ensure that only TE light is detected by the InGaAs PIN photodiode (PD). The LP has a 20 dB extinction. The photocurrent is converted into a voltage which is detected by a lock-in amplifier, referenced to the chopper. The transimpedance circuit is simple and is shown in Figure 4.10. The noise equivalent power (NEP) is $\sim 30\ \mathrm{fW}/\sqrt{\mathrm{Hz}}$ at 2 kHz.

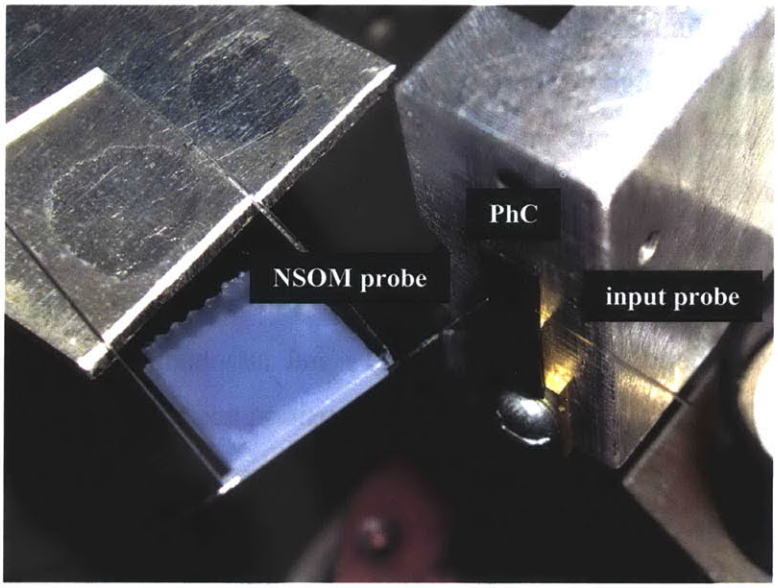

Figure 4.9 – Photo of the "homemade" contact-mode NSOM setup for scanning of the beam inside the PhC.

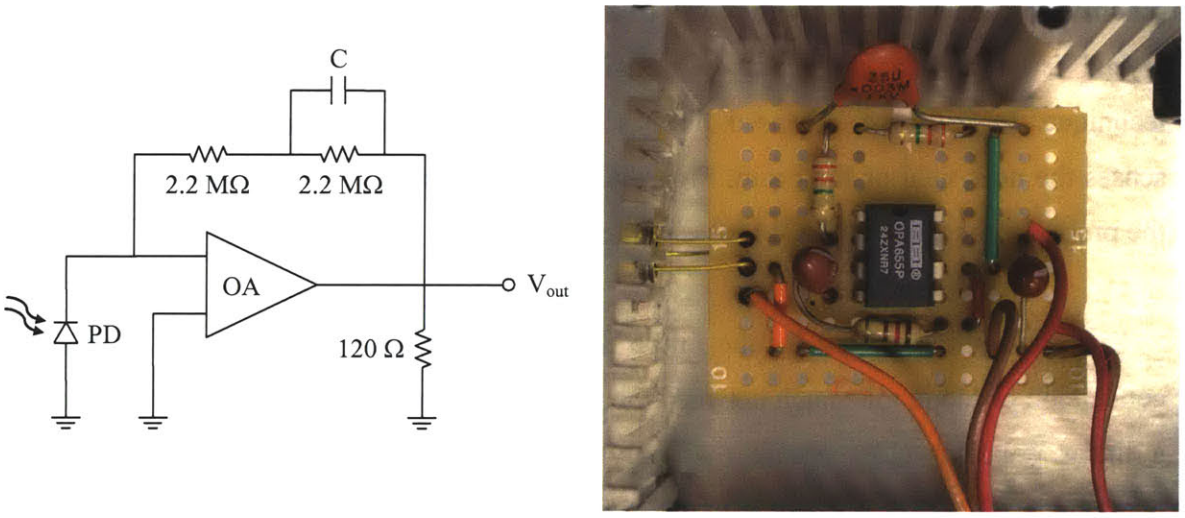

(a)

(b)

Figure 4.10 – Transimpedance circuit used to convert the photocurrent into a voltage: *(a)* circuit diagram and *(b)* photo of the implemented circuit. The NEP is about 30 fW/Hz$^{1/2}$. The operational amplifier is a Burr-Brown® FET-input OPA655 and the photodetector is a Hamamatsu G8376 series InGaAs PIN photodiode.

Both laser source and lock-in are controlled by LabView® through GPIB, allowing the synchronization of the scanning sequence. The scanning program developed is a raster-scan that allows changing the step size and scanning range. A visible laser source is coupled through the coupler (C) in order to align the scanning probe before the scan, using the visible camera.

4.2.1 Input/Output Coupling Fiber

A high NA single-mode (SM) lensed fiber is used to couple light in/out of the PhC and is shown in Figure 4.11. The fibers are fabricated by a heating and pulling process, by Nanonics Imaging Ltd. They have a spot size of about 1.7 μm and a working distance of about 4 μm.

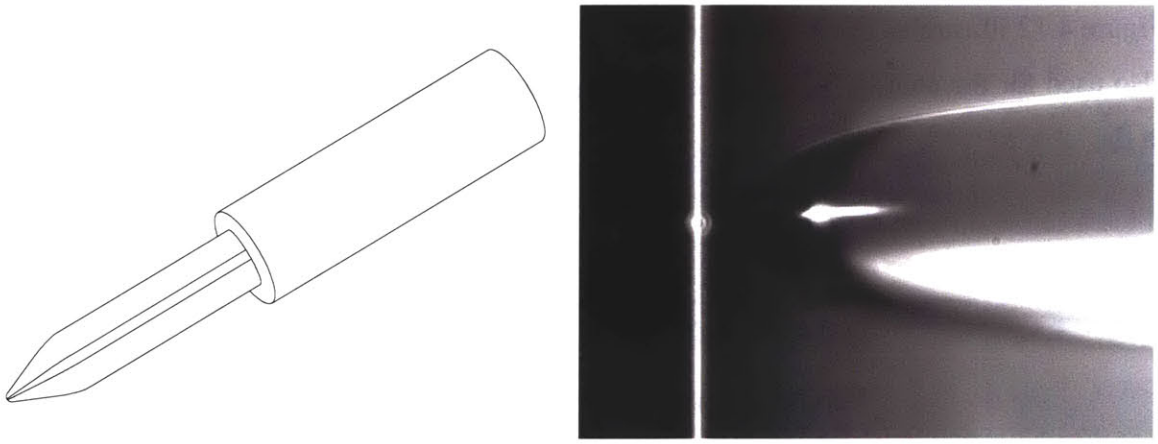

(a) *(b)*

Figure 4.11 – Lensed fiber probes used to couple light into the PhC and for the confocal and NSOM measurements: *(a)* schematic of a probe and *(b)* photo taken under a microscope.

The relation between the beam spot size ($2W_0$) and the full-width at half-maximum (FWHM) is:

$$\text{FWHM} = \sqrt{\frac{\ln(2)}{2}} \cdot (\text{spot size}) \tag{4.2}$$

The equivalent FWHM for the 1.7 μm beam is 1.0 μm. The spread of the transverse wavevector for this beam size is about $\pm 2.4\ \mu m^{-1}$, indicating that such a narrow spot size is not supported by the PhC. As mentioned, the estimated minimum FWHM supported inside the PhC is about 2.4 μm (spot size of about 4 μm), and the expected FWHM is about 2 μm (spot size of about 3.4 μm). This gives additional flexibility in the working distance: even if the working distance is off by half a diffraction length, the excited spot size will still be the same.

The relevant specifications of the fiber probes[49,50] are summarized in Table 4.1. Figure 4.12 illustrates the described parameters. A polarization-maintaining (PM) fiber is also used for the contact NSOM measurements, so the main characteristics are presented in the table as well.

	SM	PM
Spot size (μm)	1.7 ± 0.3	1.7 ± 0.3
FWHM (μm)	1.0 ± 0.2	1.0 ± 0.2
Working distance (μm)	4 ± 1	3.5 ± 1
NA	~0.4	~0.4

Table 4.1 – Main specifications of the probes. SM is a single-mode fiber and PM is a polarization-maintaining fiber.

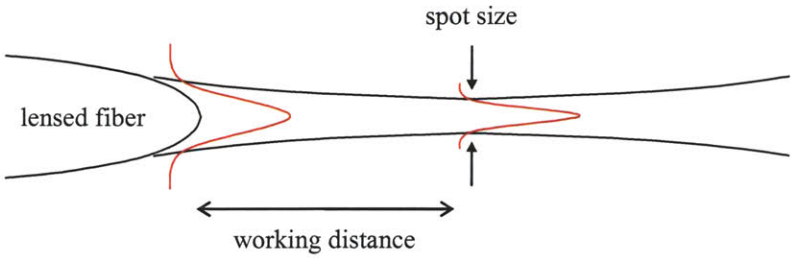

Figure 4.12 – Lensed fiber probe indicating the working distance and the spot size.

The spot size of the fiber was experimentally confirmed by scanning it over a 205 nm stripe of light, at the working distance, and plotting the response – Figure 4.13. The measured FWHM is 1.01 μm, and after deconvolution with the 205 nm stripe, the FWHM for the fiber is 0.99 μm. This number agrees with the announced value of 1 μm.

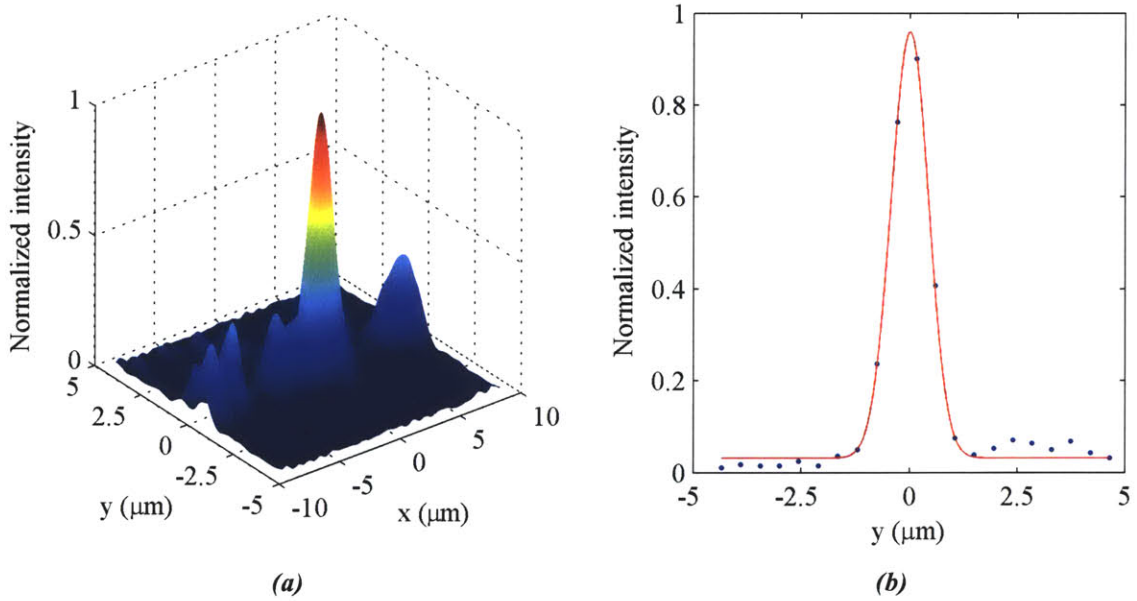

Figure 4.13 – Measure of the spot size of the fiber probe. After deconvolution, a 0.99 μm FWHM is found: *(a)* 3D profile at the output of a 205 nm stripe of light measured with the specific fiber probe and *(b)* 2D profile of the output, showing a Gaussian fit to the data. The scanning step size is 0.45 μm.

The input is maximized by controlling the distance between the fiber and the input facet with the stage S1, as well as the overlap of the spot with the 205 nm layer, by adjusting the height of the probe. Even if the distance is not exactly the correct working distance, the super-collimation may take effect. The only difference is that the coupling is weaker (less overlap between the input spot and the 205 nm layer).

4.2.2 Confocal Imaging Technique

The confocal imaging technique is straightforward and returns high-resolution images. The basic idea is depicted in Figure 4.14. The input fiber focuses the 1.7 μm beam at the input of the PhC, at a working distance of about 4 μm. After propagating and reaching the output facet, the light is collected by the second fiber which is also the working distance from the facet. This is equivalent to saying that the output facet of the PhC lies in the focal plane of the fiber. At the working distance the beam size is at its minimum waist size, i.e., it is focused. If the output fiber is scanned in 2D then a high-resolution image can be obtained by mapping the detected intensity at each point. As mentioned, the resolution of the probe is 1 μm.

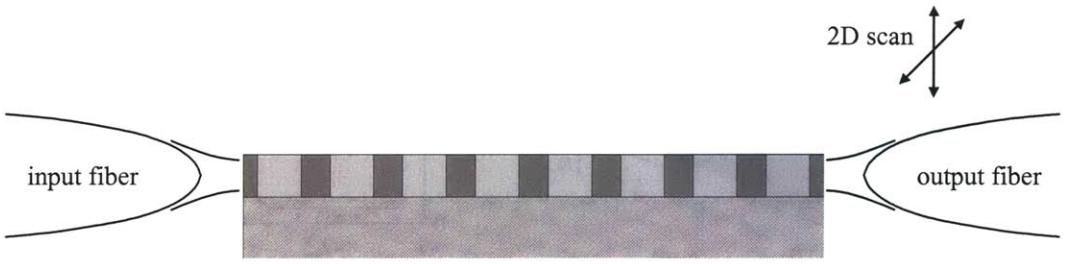

Figure 4.14 – Confocal imaging technique. A fiber probe is scanned at the output facet, at the working distance. The mapping of the intensity at each point gives the image of the output mode.

After finding the right working distance from the output facet (with stage S3), the fiber probe is scanned over a (18 × 18) μm area with steps of 0.9 μm (these parameters

are adjustable). At each position there is a waiting time (~100 ms) to allow for fiber oscillations to relax. The detection is made with the lock-in and all the data is stored in a file. An example of a confocal image obtained with this technique is the one presented in Figure 4.13 (although in this case the main goal was to measure the resolution of the probe instead of using the probe to measure a specific feature).

4.2.3 Contact-mode NSOM Technique

This technique is a rough near-field measurement, without any distance-to-sample feedback control. The basic principle of the near-field measurement is depicted in Figure 4.15. The scanning probe is a PM fiber with similar characteristics to the SM fibers mentioned before.

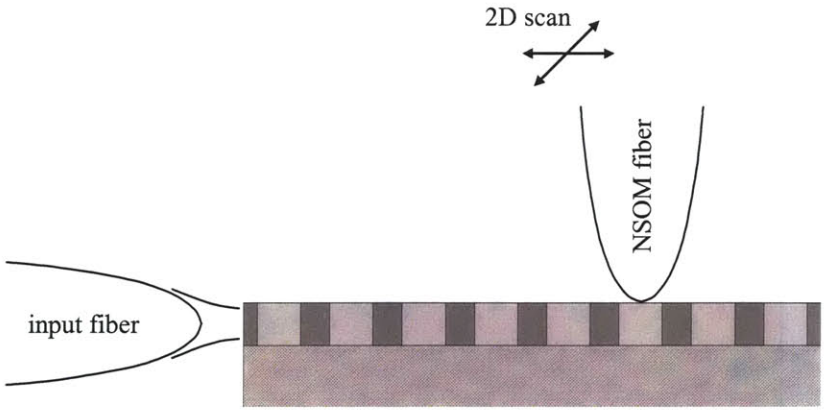

Figure 4.15 – Principle of the near-field measurement. The evanescent field can be sensed by the probe at distances in the order of the decay length, which are smaller than the wavelength. The fiber probe is scanned in contact with the surface of the PhC.

In doing this type of measurement, it is essential to know whether the detected field is really a near-field signal or a far-field scattered signal. In addition, the resolution for confocal imaging is known, but the near-field resolution has still to be determined.

Feedback NSOM techniques allow for the discrimination between near-field and far-field. In the present case, the distinction is achieved by scanning the fiber probe over a known structure with very well localized scattering losses.

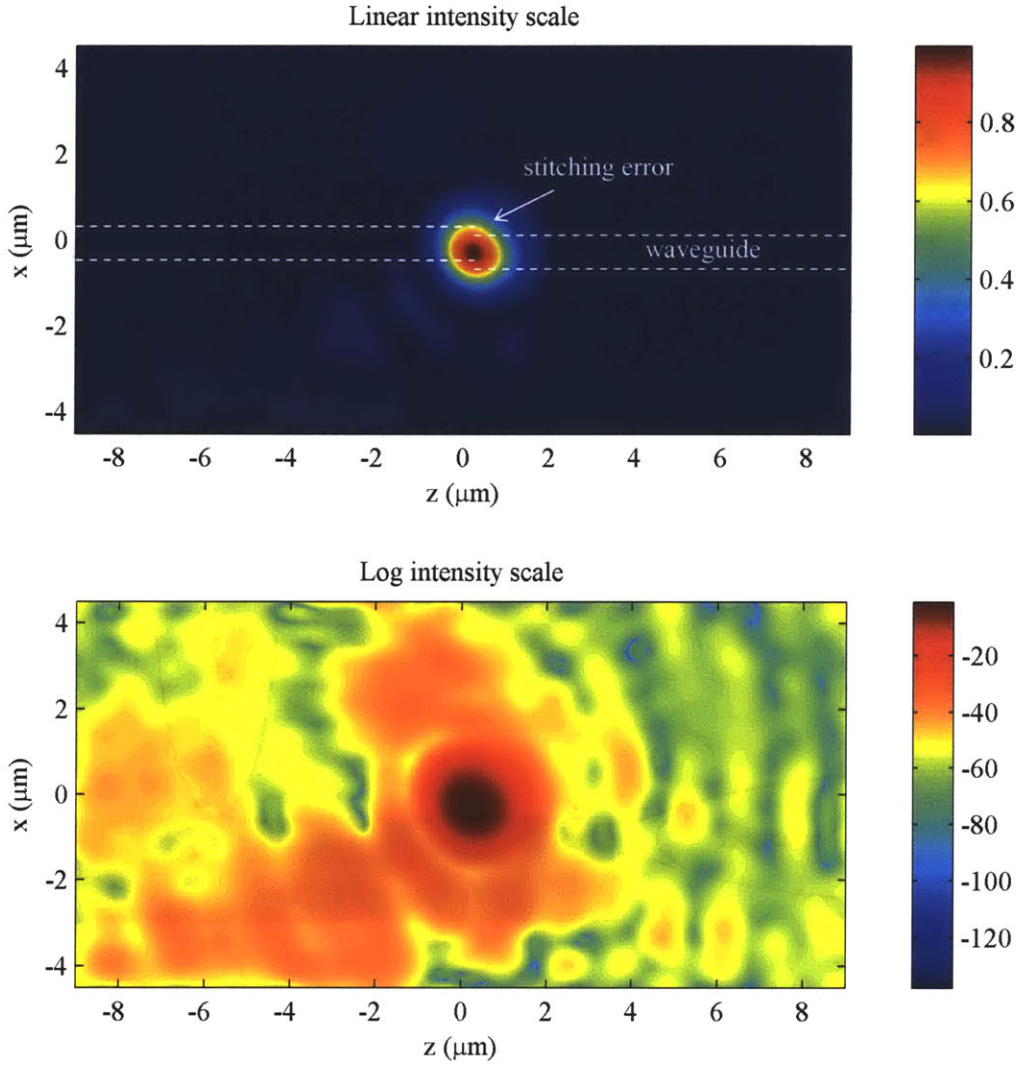

Figure 4.16 – Confocal image obtained from a test waveguide, showing the light scattered at a stitching error. Waveguide dimensions are not to scale. The scanning step size is 0.45 μm.

The structure used to implement this is a 400 nm wide and 250 nm high silicon waveguide, fabricated by e-beam lithography. Due to fabrication errors – stitching errors – there are localized points that scatter a large amount of light. These points are well localized and easy to observe from the top of the waveguide. By bringing the probe in focus with one of these points and doing a scan, a confocal image is obtained – Figure 4.16. Since the losses in the remaining waveguide are very small (less than 1 dB/mm) no light is seen. Moving the probe away from the stitching error, bringing it in contact with the waveguide surface and doing a new scan, returns a near-field image of the waveguide – Figure 4.17. The image is then column averaged and fitted to a Gaussian function. The FWHM is 1.47 μm, and after deconvolving it with the waveguide width, a probe resolution of about 1.4 μm (in FWHM) is obtained.

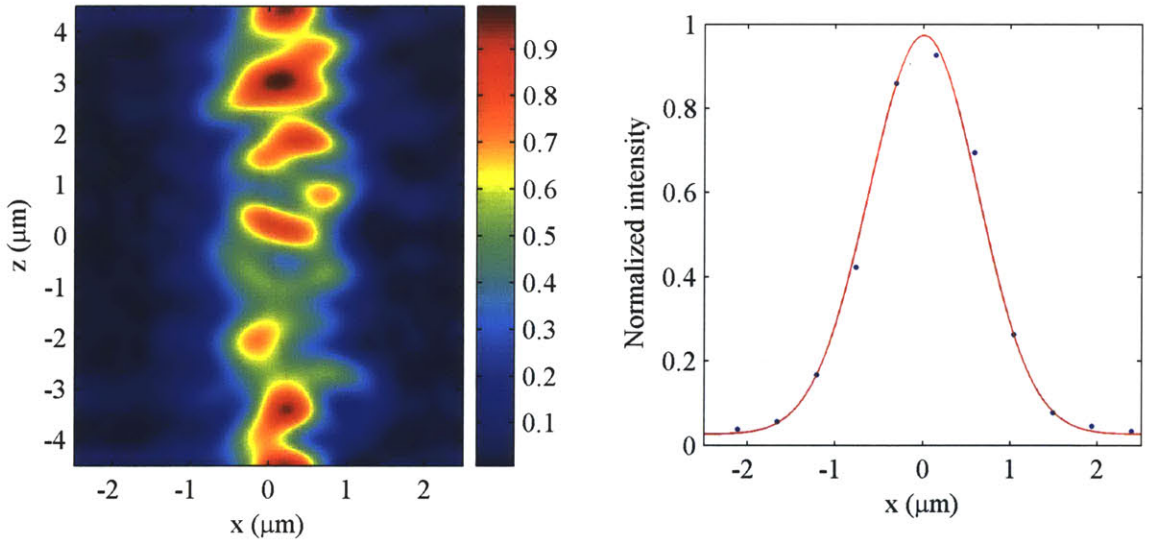

Figure 4.17 – Near-field image of the test waveguide: *(a)* 2D scan and *(b)* column averaged data fitted by a Gaussian curve with FWHM = 1.47 μm. The scanning step size is 0.45 μm.

As a side note, the NSOM image obtained for the known waveguide is grainy. This is not due to the structure itself; instead, it may be a result of the implemented NSOM technique.

The same PM fiber probe is now used to scan (in contact) over the PhC sample, next to the region where the beam propagates – position **B** in Figure 4.6. Figure 4.9 shows the implementation of such a configuration in the experimental setup. This no-feedback technique is only possible because the surface topography is flat, i.e., there are no significant height variations along the crystal. The probe is barely touching the surface and any additional tension may damage the probe and/or the sample. The initial distance is controlled and set by observing the reflection from the surface of a visible spot which is coupled into the scanning fiber through the coupler C (in Figure 4.6). The scanning procedure is the same as described before.

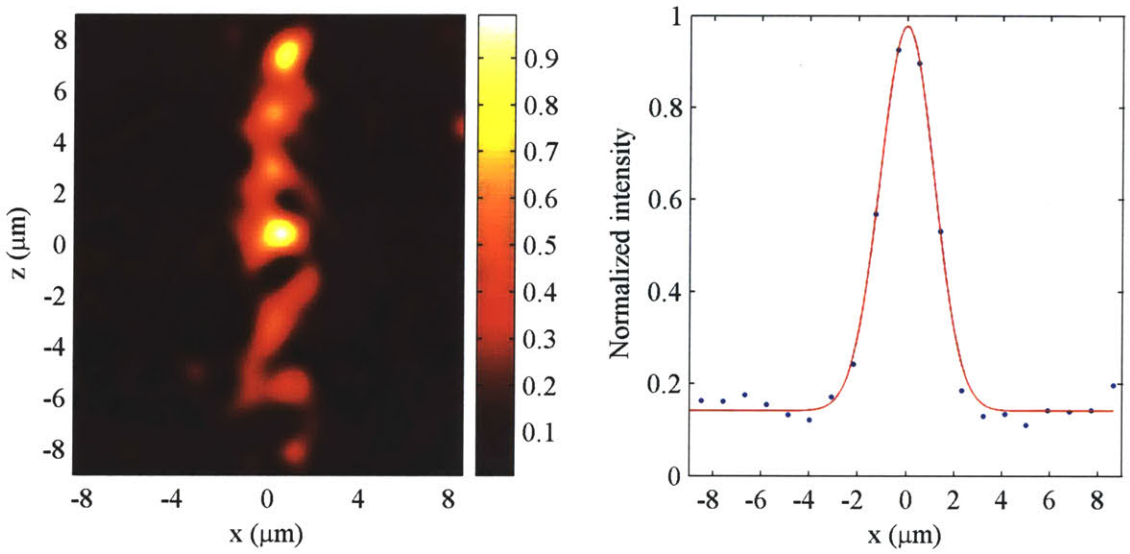

Figure 4.18 – Contact NSOM image from the top, for $\lambda = 1503$ nm at 1 mm from the input: *(a)* 2D scanned image and *(b)* Gaussian fit of the averaged data columns, with FWHM = 2.64 μm. The scanning step size is 0.9 μm.

Excelent images are obtained with this technique. Figure 4.18 shows the result of such a scan at 1 mm away from the input, for $\lambda = 1503$ nm, showing super-collimation. The data is fitted to a Gaussian function, yielding a FWHM of 2.64 μm. The experimental points in Figure 4.18*(b)* represent the average of each column of data. Also, the intensities are all normalized. As seen from this image, the FWHM is larger than the expected value of 2 μm. This is because the measured value is convolved with the resolution of the scanning probe, which is 1.4 μm (in FWHM). After deconvolution, a FWHM of 2.24 μm is obtained for the beam propagating inside the PhC, which is close to the expected value of 2 μm. Again, the grainy image does not necessarily indicate a poor beam inside the PhC.

4.2.4 Top IR Imaging Technique

A large amount of the light propagating inside the PhC is scattered due to nano-scale roughness. This results in higher losses in the PhC, but can be useful for observing the spatial beam behavior as the beam propagates.

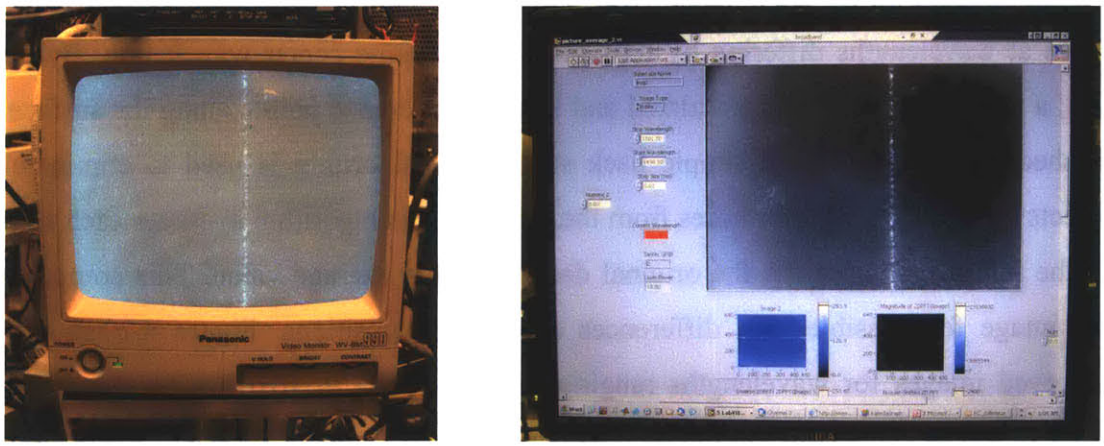

(a) *(b)*

Figure 4.19 – Top image obtained with an IR camera showing super-collimation: *(a)* displayed in a monitor and *(b)* recorded through an image acquisition card for post-processing. The image size is 720 by 540 μm.

With a sensitive IR camera from the top, the light focused by a microscope objective (O) can be observed in a monitor and recorded for future processing – Figure 4.19. The camera is attached to a micropositioning stage, allowing it to be moved parallel to the surface, along the whole sample and with high precision.

4.3 Wavelength Dependence

As mentioned before, the equifrequency contours take very different shapes for different wavelengths. There will be super-collimation for a specific wavelength λ_{sc}, with a bandwidth $\Delta\lambda$. For other wavelengths the beam may diverge like it does inside an isotropic medium, or experience fanning and steering as predicted by the simulations in chapter 3. This section studies the wavelength dependence of the spatial profile of the beam inside the PhC. TE light is coupled into the device (1.7 μm spot beam) and successive top IR images are taken near the input facet, as the wavelength is tuned. The images are acquired at about 400 μm away from the edge. Note that at this position, the spot size of the beam is already 3.4 μm. In order to reduce the noise due to laser speckle (which depends on the wavelength), each image is actually the average of 300 snapshots taken at wavelengths differing by 0.01 nm, around some center wavelength. By doing this, a white light source is simulated and small interference points along the surface are washed out. In addition, a simple back subtraction algorithm is used to eliminate the effects of spatial non uniformities from the camera. This algorithm averages each column of the image and subtracts the original data from this average value. This compensates the image for possible gain differences at different positions. Figure 4.20 shows the observed images for wavelengths ranging from 1430 nm to 1610 nm (or equivalently, from $\Omega = 0.245$ to $\Omega = 0.217$). The input laser power is between 3 and 5 mW. Strong frequency dependence is observed and the optimum wavelength for the super collimation effect λ_{sc} is around 1500 nm. Note that this value is not exactly the same as the one predicted from the equifrequency contours (1535 nm).

Figure 4.20 – Spatial profile wavelength dependence.

There is no observable spreading of the beam for a bandwidth of at least 20 nm around 1500 nm. A fanning effect is observed at other wavelengths. The results show that this effect is stronger for shorter wavelengths, as predicted by the simulations.

The image size is (460 × 200) pixels, which corresponds to about (518 × 225) μm. This calibration was performed by imaging a regular fiber probe (for which the cladding dimension is known) under the same setup.

Another image showing the beam fanning is also presented – Figure 4.21. This image was acquired for a different input fiber position, sensing a different part of the crystal. This shows that the input facet may have a big influence in defining the shape of the beam, for wavelengths outside the super-collimation regime.

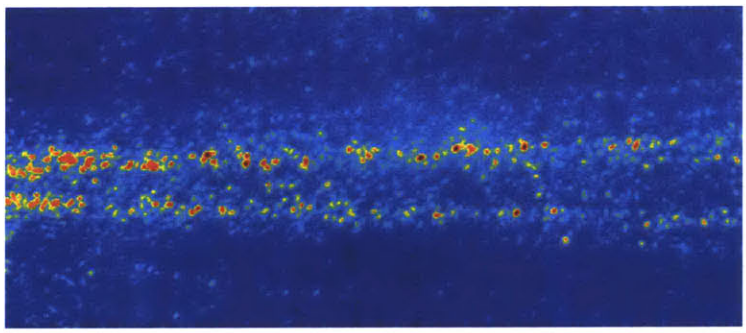

Figure 4.21 – Top IR image of the beam inside the PhC, for λ = 1430 mm, showing fanning.

4.4 Super-Collimation over a 3 mm Sample

Operating around the super-collimation wavelength, the PhC is able to guide light with no observable spatial dispersion, over large distances. λ_{sc} was experimentally determined to be around 1500 nm – Figure 4.20. The scattered light enables the monitoring of the beam from the top, using an IR camera. When testing the 3 mm

sample – Figure 4.4*(a)* – the collimated beam is seen to propagate over the whole sample length – Figure 4.22. This image is obtained by moving the IR camera parallel to the sample surface, along the distance of propagation and acquiring images at each one of these positions. The combination of all the individual images gives a complete view of the qualitative behavior of the beam in the super-collimation regime. A bright spot at the output confirms the presence of the beam. The image was taken at $\lambda = 1500$ nm.

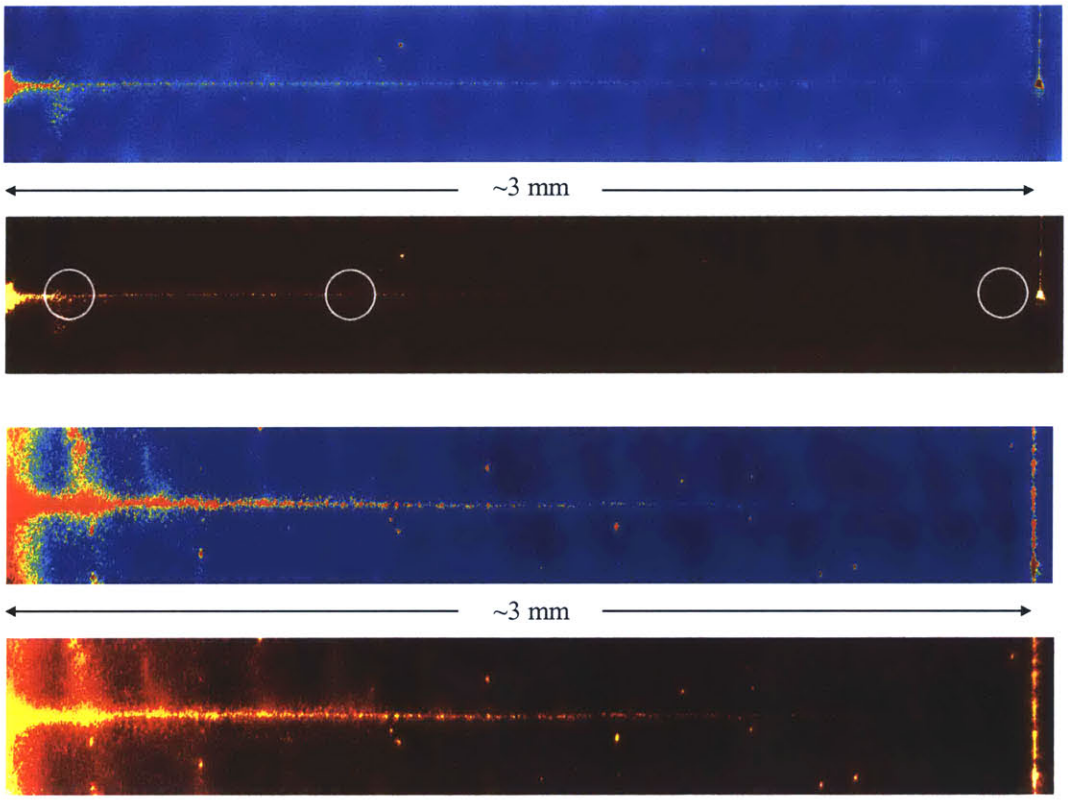

Figure 4.22 – Top IR images showing super-collimation over 3 mm, at $\lambda = 1500$ nm.

There is no apparent spatial spreading over the whole distance, but in order to better account for quantitative results, the contact-mode NSOM technique mentioned before was used. As discussed, this near-field technique has a resolution of 1.4 μm (in FWHM). Results for three different positions along the propagation direction (marked

with circles in Figure 4.22) are presented in the figures that follow, for wavelengths around $\lambda = 1500$ nm.

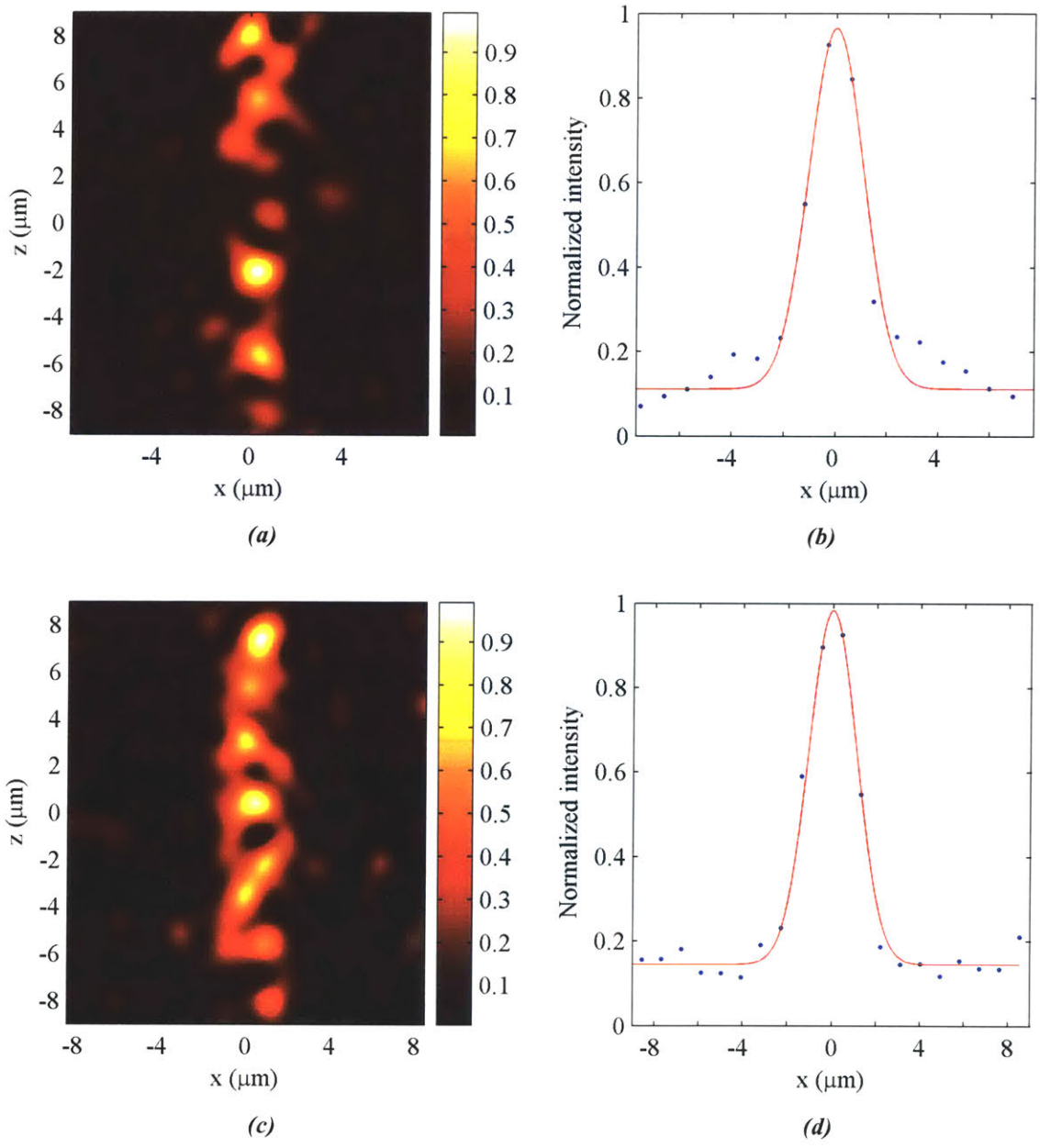

Figure 4.23 – NSOM images at two different positions along the PhC: *(a)*, *(b)* 200 μm away from the input, $\lambda = 1505$ nm, and *(c)*, *(d)* at 1 mm, $\lambda = 1503$ nm. The scanning step size is 0.9 μm.

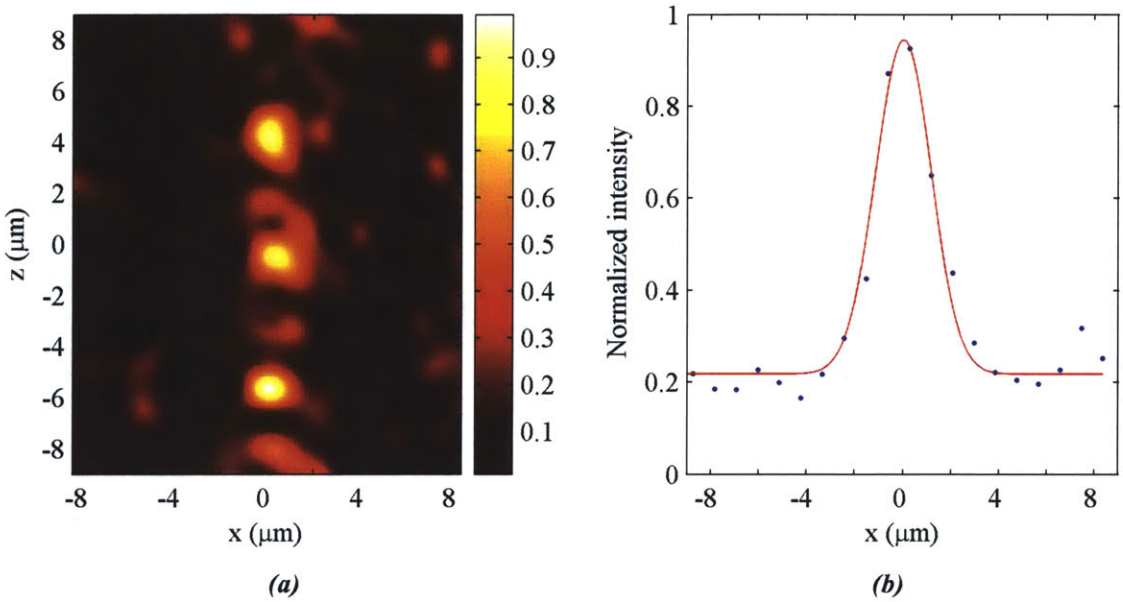

Figure 4.24 – NSOM images at 3 mm away from the input, for $\lambda = 1502$ nm. The scanning step size is 0.9 μm.

The images indicate that the beam stays collimated inside the PhC, and give some information about its width. The grains in the images can be eliminated by averaging each data column. The data is fitted to a Gaussian function and return a FWHM of 2.49, 2.54 and 2.71 μm, respectively. After deconvolution with the scanning probe resolution, FWHMs of 2.06, 2.12 and 2.32 μm are obtained. More important than describing the exact beam width, the main result here is the spatially stationary behavior of the beam over a very large propagation distance.

At this point, it is useful to define the figure of merit for the super-collimation effect as the number of diffraction lengths propagated by the beam without spatial spreading:

$$N = \frac{L}{z_0} = \frac{L\,\lambda_0}{n\,\pi\,W_0^2} \tag{4.3}$$

where L is the distance over which super-collimation is observed and n the effective index in the direction of propagation correspondent to the correct equifrequency contour. This number is 2.2, as mentioned before. Using $W_0 = 1.7$ μm (from the expected spot size of 3.4 μm), the diffraction length is $z_0 = 13.3$ μm and the figure of merit is about $N = 226$. This result by itself is almost 40 times greater than that of any other self-collimation result reported (the best of which was calculated to be around $N = 6$)[25]. Another interesting figure is the number of lattice constants over which the supper-collimation is observed. For the 3 mm sample this number is over 8500.

4.5 Loss Estimation

Although the main goal of this project was the study of super-collimation in the PhC, the present section discusses some important issues related with the losses in the structure. The different polarizations, TE-like and TM-like, will have different losses. From an intuitive approach, the losses should be greater for the TE polarization than for the TM polarization. The reason for this is that the TE mode (electric field parallel to the 2D plane) is much more confined inside the crystal, while the TM mode (electric field normal to the 2D plane) extends into the air and the under-cladding, and therefore sees less of the PhC. The fact that the TE-like collimated beam can be observed from the top indicates large losses due to scattering. These losses could be reduced if the device were symmetric, which would be made possible by removing the SiO_2 layer under the 205 nm Si layer. This approach has been mentioned and implemented by other groups[33]. In the present case, since the operation is in the first band, always under the light line, the asymmetry issue should not be limiting. The main loss mechanism is, clearly, scattering at the holes due to nano-scale roughness.

The losses are estimated by two independent processes – from the top IR images and from the contact NSOM images – yielding consistent results. Figure 4.25 presents an image obtained from the top, showing super-collimation over the 3 mm sample. This

image is qualitatively similar to Figure 4.22, but was acquired with a second IR camera which is linear.

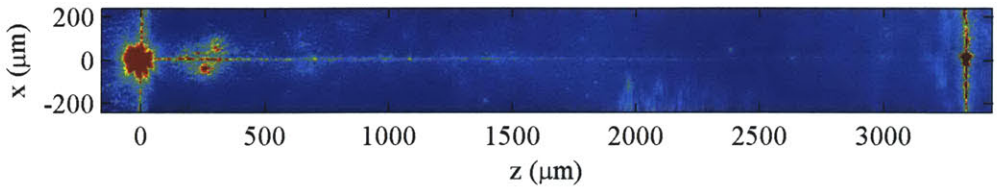

(a)

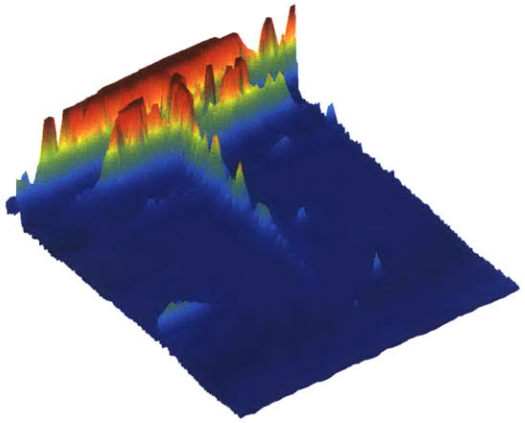

(b)

Figure 4.25 – Top IR images of the beam propagating over 3 mm, at the super-collimation regime: *(a)* top 2D image and *(b)* 3D view.

The longitudinal profile of this beam is shown in Figure 4.26. The exponential fit function is

$$\text{Normalized intensity} = a.\exp(bx) + c \tag{4.4}$$

Only the non saturated points were considered for the fit. The obtained fitting parameters are:

$$
\begin{aligned}
a &= 0.70 \pm 0.03 \\
b &= -0.0012 \pm 0.0001 \quad (\mu\text{m}^{-1}) \\
c &= 0.14 \pm 0.01
\end{aligned}
\tag{4.5}
$$

b gives the loss of the beam inside the crystal:

$$
\text{Loss} = 10\log\left[\exp(10^4 b)\right] = -52 \text{ dB/cm} \tag{4.6}
$$

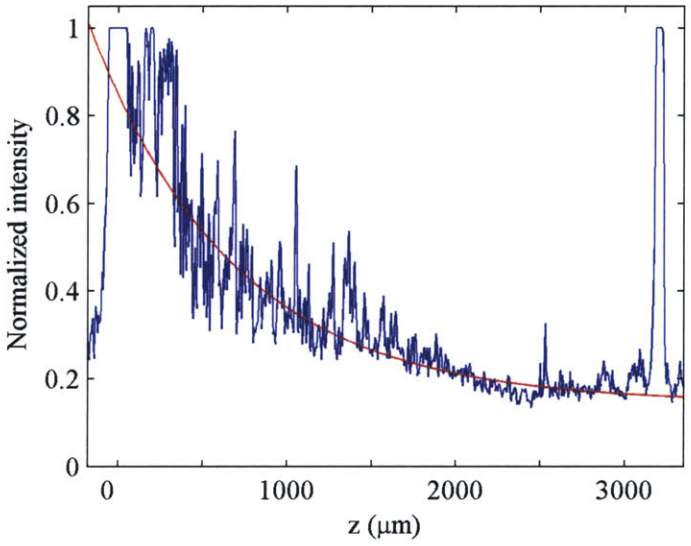

Figure 4.26 – Longitudinal profile of the beam with exponential fit to the data, returning a loss of ~52 dB/cm.

The calculated loss corresponds to the TE radiation. In order to estimate the TM loss, the NSOM images can be used. Each one of the near-field images is fitted to a Gaussian function (like in Figure 4.23). Each one of these curves has a background (or floor) level. This background level traduces the amount of TM light measured, while the Gaussian itself represents the intensity of the TE mode. Using this approach, the TE losses can be estimated form the areas under the Gaussian curves, and the TM losses

from the area of the offset (DC level) of each Gaussian. The experimental values used for this calculation are presented in Table 4.2 and plotted in Figure 4.27:

x (mm)	TE (a.u.)	TM (a.u.)
1	0.0193	0.0166
	0.0198	0.0123
	0.0171	0.0144
	0.0146	0.0153
	0.0106	0.0144
	0.0194	0.0159

x (mm)	TE (a.u.)	TM (a.u.)
3	0.0019	0.0060
	0.0017	0.0062
	0.0022	0.0055
	0.0021	0.0054

x (mm)	TE (a.u.)	TM (a.u.)
2	0.0028	0.0079
	0.0081	0.0077
	0.0039	0.0075
	0.0074	0.0069

Table 4.2 – Values used to estimate the loss of the TE and TM modes inside the PhC. These values are extracted from several NSOM images taken around 1500 nm. The value marked as TE corresponds to the area of the fitted Gaussian function, and the TM corresponds to the area of the floor level of the data.

The resulting losses are ~48 dB/cm for TE and ~22 dB/cm for TM. The two values obtained for TE are consistent. It is also clear that the TM modes are less attenuated than the TE. Although only TE light is launched into the PhC, considerable mount of TM radiation is also present due to scattering at the input facet and along the crystal. In addition, the modes inside the fiber probe and the modes of the PhC do not exactly overlap. It was observed that after 3 mm of propagation, the TE peak signal was still higher than the TM signal, but after 8 mm TM dominated over TE. This fact makes it difficult to observe super-collimation for distances close to 8 mm.

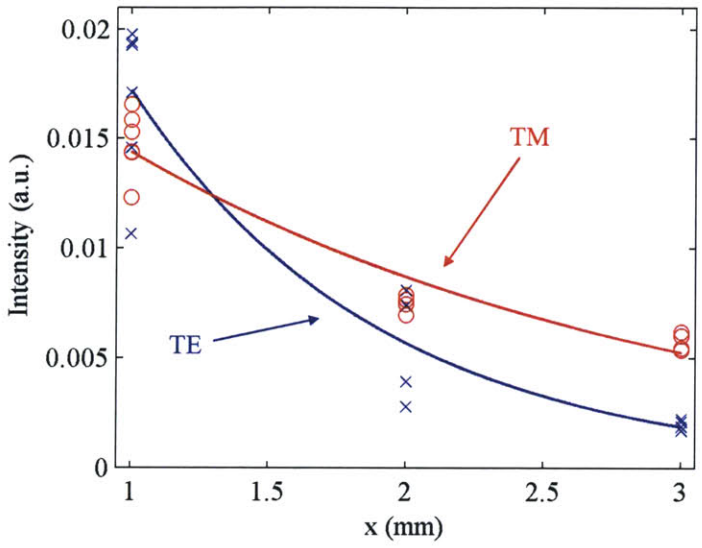

Figure 4.27 – Loss estimation for TE and TM modes, obtained from the NSOM images. The values are ~48 dB/cm for TE and ~22 db/cm for TM.

4.6 Super-Collimation over 5 mm and 8 mm Samples

For distances greater than 3 mm, the beam cannot be detected from the top through the IR camera. At this point, the scattered signal level is below the noise floor of the camera. However, sensitive confocal measurements at the output facet can still detect TE signal after 5 mm, and even after 8 mm!

Coupling light into the 5 mm sample – Figure 4.4*(b)* – the super-collimation effect can still be observed. The IR camera can track the beam over about 3 mm, but then it is lost. However, at the output facet, enough light from the beam is scattered, allowing it to be detected again. This spot at the output facet shows the position of the output beam – Figure 4.28. Moving the output fiber probe to this position and performing a confocal scanning measurement, the image in Figure 4.29 is obtained.

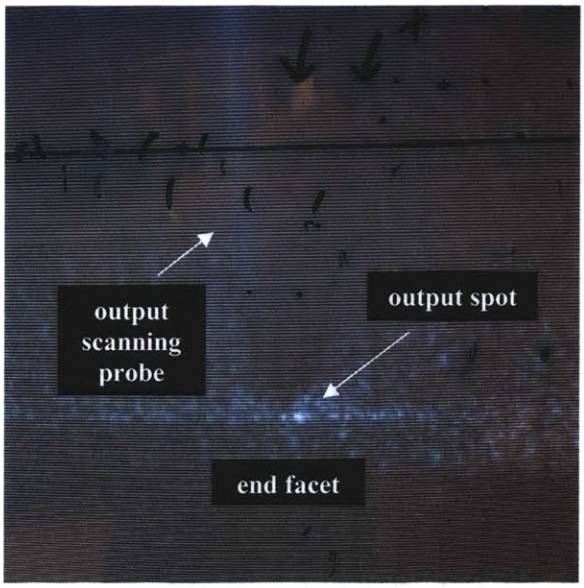

Figure 4.28 – Top IR image at the output facet showing the scattered beam, in the super-collimation regime, for the 5 mm sample.

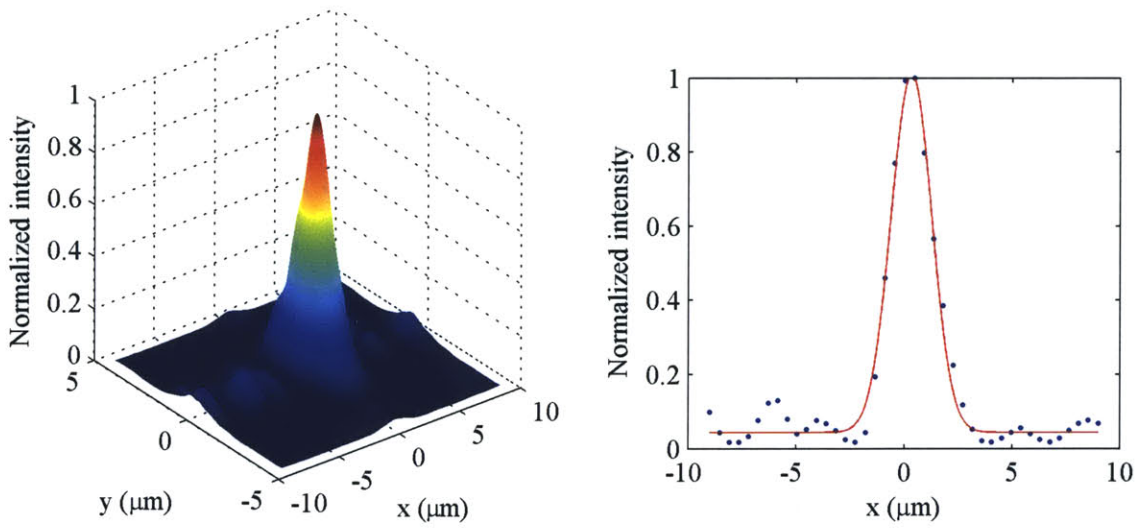

(a) ***(b)***

Figure 4.29 – Confocal image at the output of the 5 mm sample, at 1494 nm, showing that the beam width is conserved: *(a)* 3D beam profile and *(b)* Gaussian fit of the transverse section (along *x*), with FWHM = 2.20 μm. The scanning step size is 0.45 μm.

After deconvolution with the probe resolution (1 μm), a beam of FWHM = 1.96 μm is observed, for $\lambda = 1494$ nm. This value is remarkably similar to the ones obtained for the 3 mm sample, from the top NSOM images. Using expression (4.3), the figure of merit for the supper-collimation effect is now $N = 376$, corresponding to more than 14200 lattice constants.

An analogous procedure for the 8 mm sample – Figure 4.4*(c)* – gives similar results. At this distance the beam spot at the output facet is still detectable. The confocal image for $\lambda = 1501$ nm is shown in Figure 4.30 and the Gaussian fit returns a beam size of 1.51 μm (FWHM), after deconvolution. This value is smaller that expected, which is not very clear.

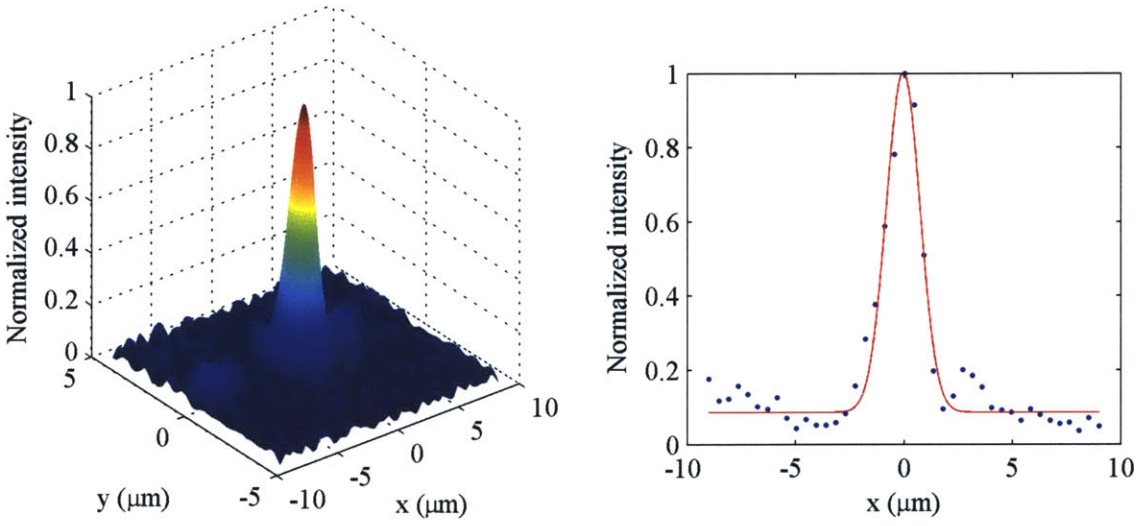

(a) *(b)*

Figure 4.30 – Confocal image at the output of the 8 mm sample, at 1501 nm, showing that the beam width is conserved: *(a)* 3D beam profile and *(b)* Gaussian fit of the transverse section (along *x*), with FWHM = 1.81 μm. The scanning step size is 0.45 μm.

Further precautions and experiments need to be done in order to understand or correct this observation. For now, it will be considered a possible solution. If valid, this shows negligible spatial spreading of the beam over almost 1 cm. The observed propagation distance corresponds to over 22800 lattice constants and sets the figure of merit at $N = 601$, which is two orders of magnitude larger than any other self-collimation result reported.

5

APPLICATIONS, FUTURE WORK AND CONCLUSIONS

Super-collimation in a planar 2D PhC was demonstrated over centimeter-scale distances. The current chapter presents some features observed in the super-collimation regime and discusses further applications, indicating possible routes for future work.

5.1 Bending, Splitting and Coupling at an Angle

As mentioned in the previous chapters, there is some flexibility in the working distance between the coupling probe and input facet. In addition, it was observed that the angle of coupling is also flexible. Figure 5.1 shows super-collimation with light coupled at an angle of ~18° with respect to the direction of propagation. The position and direction of the probe are indicated by the dashed lines. The wavelength is 1500 nm and

the image is acquired from the top of the sample, using the IR camera. This angle is close to the maximum allowed coupling angle discussed in chapter 2 (~14°).

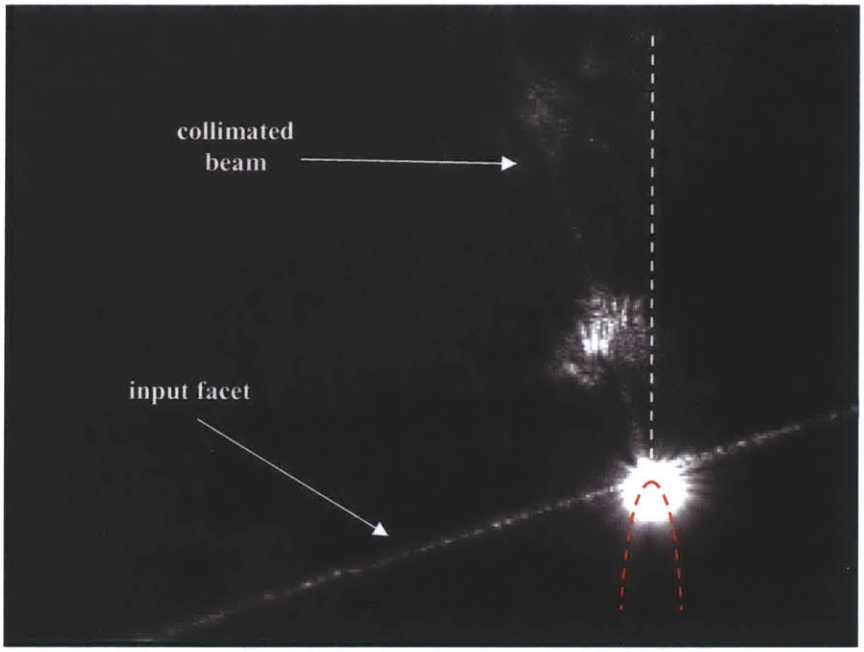

Figure 5.1 – Image from the top showing super-collimation with coupling at an angle with respect to the propagation direction. The angle is ~18° and the wavelength is 1500 nm.

Besides the flexibility in the coupling angle, there is total flexibility in the horizontal direction position. In fact, by moving the input fiber along this direction, the collimated beam moves accordingly inside the PhC. The only critical alignment position is in the vertical direction, which requires a good coupling into the 205 nm Si layer.

Another interesting feature is the ability to bend light at sharp angles. A large defect can serve as a mirror, as illustrated in Figure 5.2. Furthermore, light can be coupled into the direction perpendicular to its propagation. Remember that the equifrequency contours are symmetric under a 90° rotation. This can happen at a scattering point and is demonstrated in Figure 5.3. Here it is seen that the cleave of the input facet at this position, which is illuminated at the bottom of the image, is not

perfectly perpendicular to the direction of propagation. This small fabrication error does not affect the performance of the PhC in a drastic way, in the super-collimation regime.

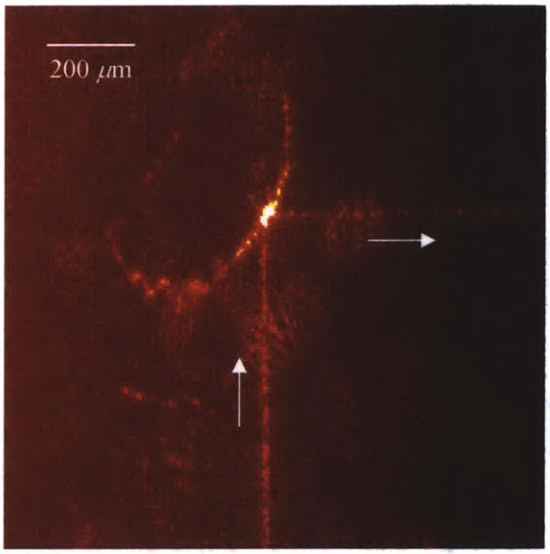

Figure 5.2 – IR image from the top showing bending of the collimated beam, at $\lambda = 1500$ nm.

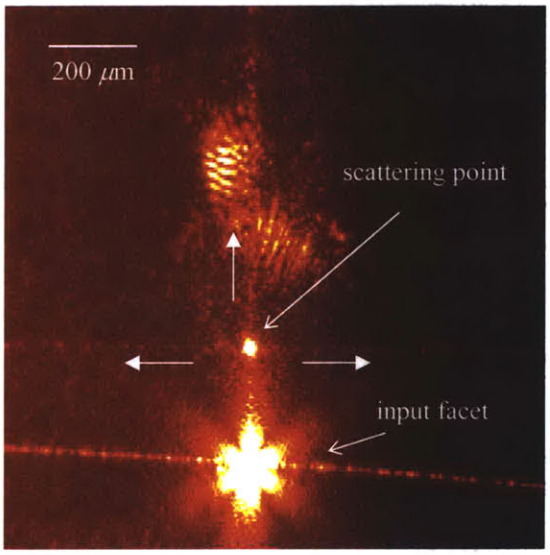

Figure 5.3 – IR image from the top showing scattering at a defect and excitation of a collimated beam in the direction perpendicular to the initial beam, at $\lambda = 1500$ nm. The bottom stripe (at an angle) is the input facet.

An interesting feature would be the ability of coupling light into the PhC from the top of the structure. This could be done by placing a high-index matching fluid droplet on the top surface of the crystal and bringing down a fiber probe. This idea is illustrated in Figure 5.4 and is an interesting application to be developed in the future.

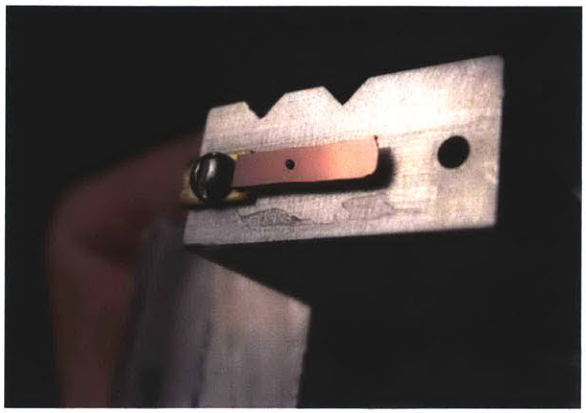

Figure 5.4 – PhC sample with a small droplet of high-index matching fluid on the top surface, for coupling from the top. The coupling would be done with a lensed fiber probe submerged into this droplet.

5.2 Applications and Future Work

Several applications were mentioned in chapter 1 and 2. The lines below develop some of them in a little more detailed way.

Optical integrated circuits

Routing of optical signals represent a powerful application of the features observed in this report. Being able to collimate, split and bend beams is useful in the development of optical integrated circuits. Optical switches can also be designed, making use of the ability to direct part of the beam by controlling the phase at the input, slightly away from the super-collimation regime (Figure 3.17). In addition, a super-collimated

beam can serve as an optical interconnect between different blocks – Figure 5.5 – and the flexible coupling makes this technique robust. Light can also be easily coupled from the top and beams can cross each other without cross-talk[28].

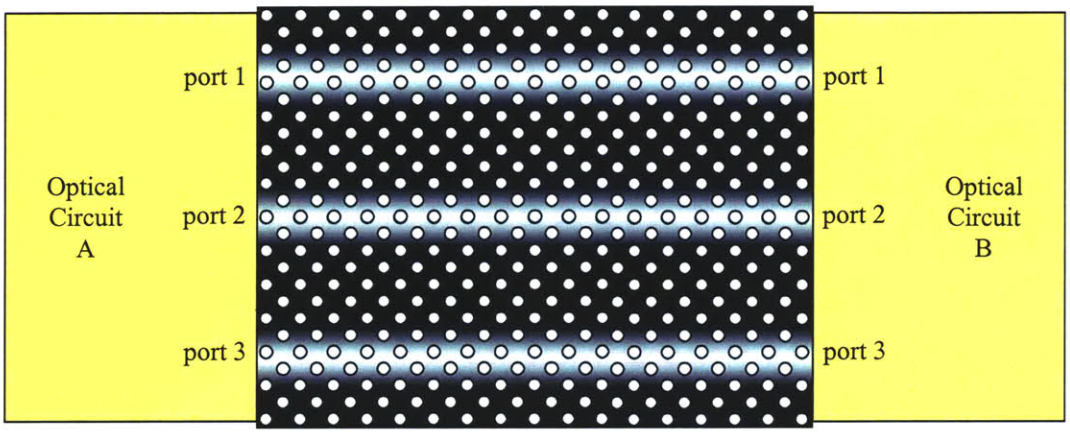

Figure 5.5 – PhC device used as an optical interconnect between two optical integrated blocks.

New imaging techniques

The super-collimation property of the light opens the possibility of creating new imaging systems based on PhC layers. Any beam profile at the input is an eigenmode of the PhC, i.e., it propagates without spatial dispersion, allowing the mapping of an object into an image. It has been shown that super-collimation and lensing properties of PhC slabs are related[29]. Furthermore, if a 2D PhC could be fabricated on top of a flexible substrate, such imaging devices could be used for medical applications.

Non-linear studies

As mentioned before, the effect described in this work is totally linear, although it is similar to the concept of spatial solitons. Nevertheless, 2D PhC structures can also be

used to study such non-linear phenomena. Work has been done in this area and solitons have been demonstrated in induced photonic crystals[51].

Low-loss PhC and NSOM imaging

The device used in our experiments has very high scattering losses due to nano-scale roughness. In addition, the asymmetry of the waveguide leads to leaky modes when operating in higher bands of energy. Removing the underneath SiO_2 layer and improving in the fabrication process could lead to lower losses. In such a situation, imaging from the top would not be possible and the solution for tracking the beam would be through NSOM imaging. A better NSOM apparatus is essential, mainly regarding an efficient feedback control. Such work is under development in the lab and will allow for a deeper understanding of the super-collimation effect. One very interesting goal is to fully characterize the evolution of the beam at the input of the PhC, when it transitions from the initial spot size to the allowed size inside the crystal. In addition, an improvement in the NSOM imaging technique will allow the exploration of other areas such as bio-optics.

5.3 Conclusions

In the present work the super-collimation effect in a 2D PhC has been demonstrated in a large-area SOI sample. Previous work had shown self-collimation over small distances – with figure of merit around 6. Here, collimation over centimeter-scale distances has been observed for the first time, with figures of merit as high as $N = 376$ (or even $N = 601$), corresponding to propagation over more than 14200 (22800) lattice constants. Both simulation and experimental data are presented.

For the first time, a thorough beam characterization in a super-collimating PhC has been demonstrated through both high-resolution contact NSOM and confocal imaging techniques. Also, the complete qualitative wavelength dependence has been

studied, as well as the fanning effects that may be observed. In addition, this is the first observation of the existence of a lower limit in the beam size supported by the PhC, through both simulation and experimental data.

BIBLIOGRAPHY

[1] J. Durnin, J. J. Miceli, and J. H. Eberly, *Diffraction-Free Beams*, Phys. Rev. Lett. **58** (15), 1499-1501 (1987).

[2] J. Arlt, V. Garces-Chavez, W. Sibbett, and K. Dholakia, *Optical Micromanipulation Using a Bessel Light Beam*, Opt. Commun. **197** (4-6), 239-245 (2001).

[3] H. Kosaka, T. Kawashima, A. Tomita, M. Notomi, T. Tamamura, T. Sato, and S. Kawakami, *Self-Collimating Phenomena in Photonic Crystals*, Appl. Phys. Lett. **74** (9), 1212-1214 (1999).

[4] L. J. Wu, M. Mazilu, and T. F. Krauss, *Beam Steering in Planar-Photonic Crystals: From Superprism to Supercollimator*, J. Lightwave Technol. **21** (2), 561-566 (2003).

[5] D. W. Prather, S. Y. Shi, D. M. Pustai, C. H. Chen, S. Venkataraman, A. Sharkawy, G. J. Schneider, and J. Murakowski, *Dispersion-Based Optical Routing in Photonic Crystals*, Opt. Lett. **29** (1), 50-52 (2004).

[6] J. D. Joannopoulos, R. D. Meade, and J. N. Winn, *Photonic Crystals: Molding the Flow of Light* (Princeton University Press, 1995).

[7] J. D. Joannopoulos, P. R. Villeneuve, and S. H. Fan, *Photonic Crystals: Putting a New Twist on Light*, Nature **386** (6621), 143-149 (1997).

[8] E. Yablonovitch, *Inhibited Spontaneous Emission in Solid-State Physics and Electronics*, Phys. Rev. Lett. **58** (20), 2059-2062 (1987).

[9] S. John, *Strong Localization of Photons in Certain Disordered Dielectric Superlattices*, Phys. Rev. Lett. **58** (23), 2486-2489 (1987).

[10] M. H. Qi, E. Lidorikis, P. T. Rakich, S. G. Johnson, J. D. Joannopoulos, E. P. Ippen, and H. I. Smith, *A Three-Dimensional Optical Photonic Crystal with Designed Point Defects*, Nature **429** (6991), 538-542 (2004).

[11] S. Y. Lin, E. Chow, V. Hietala, P. R. Villeneuve, and J. D. Joannopoulos, *Experimental Demonstration of Guiding and Bending of Electromagnetic Waves in a Photonic Crystal*, Science **282** (5387), 274-276 (1998).

[12] M. Loncar, D. Nedeljkovic, T. Doll, J. Vuckovic, A. Scherer, and T. P. Pearsall, *Waveguiding in Planar Photonic Crystals*, Appl. Phys. Lett. **77** (13), 1937-1939 (2000).

[13] S. Kuchinsky, V. Y. Golyatin, A. Y. Kutikov, T. P. Pearsall, and D. Nedeljkovic, *Coupling between Photonic Crystal Waveguides*, IEEE J. Quantum Electron. **38** (10), 1349-1352 (2002).

[14] F. Abdelmalek, W. Aroua, and H. Bouchriha, *Modelling of Photonic Crystals for the Design of Photonic Device Based on Soi Substrate*, Opt. Quantum Electron. **35** (14), 1245-1256 (2003).

[15] P. Bienstman, S. Assefa, S. G. Johnson, J. D. Joannopoulos, G. S. Petrich, and L. A. Kolodziejski, *Taper Structures for Coupling into Photonic Crystal Slab Waveguides*, J. Opt. Soc. Am. B-Opt. Phys. **20** (9), 1817-1821 (2003).

[16] S. J. McNab, N. Moll, and Y. A. Vlasov, *Ultra-Low Loss Photonic Integrated Circuit with Membrane-Type Photonic Crystal Waveguides*, Opt. Express **11** (22), 2927-2939 (2003).

[17] G. Chietera, A. H. Bouk, F. Poletti, F. Poli, S. Selleri, and A. Cucinotta, *Numerical Design for Efficiently Coupling Conventional and Photonic-Crystal Waveguides*, Microw. Opt. Technol. Lett. **42** (3), 196-199 (2004).

[18] P. Sanchis, P. Bienstman, B. Luyssaert, R. Baets, and J. Marti, *Analysis of Butt Coupling in Photonic Crystals*, IEEE J. Quantum Electron. **40** (5), 541-550 (2004).

[19] E. Kuramochi, S. Hughes, T. Watanabe, L. Ramunno, A. Shinya, and M. Notomi, *Low Loss Photonic Crystal Slab Waveguides: Fabrication, Experiment, and Theory*, Proc. of LEOS 2004 Annual Meeting, 505-506 (2004).

[20] Y. A. Vlasov and S. J. McNab, *Waveguiding in Silicon-on-Insulator Photonic Crystal and Single-Mode Strip Waveguides*, Proc. of LEOS 2004 Annual Meeting, 809-810 (2004).

[21] H. Kosaka, T. Kawashima, A. Tomita, M. Notomi, T. Tamamura, T. Sato, and S. Kawakami, *Superprism Phenomena in Photonic Crystals*, Phys. Rev. B **58** (16), 10096-10099 (1998).

[22] L. J. Wu, M. Mazilu, T. Karle, and T. F. Krauss, *Superprism Phenomena in Planar Photonic Crystals*, IEEE J. Quantum Electron. **38** (7), 915-918 (2002).

[23] A. Lupu, E. Cassan, S. Laval, L. El Melhaoui, P. Lyan, and J. M. Fedeli, *Experimental Evidence for Superprism Phenomena in Soi Photonic Crystals*, Opt. Express **12** (23), 5690-5696 (2004).

[24] H. Kosaka, T. Kawashima, A. Tomita, M. Notomi, T. Tamamura, T. Sato, and S. Kawakami, *Photonic Crystals for Micro Lightwave Circuits Using Wavelength-Dependent Angular Beam Steering*, Appl. Phys. Lett. **74** (10), 1370-1372 (1999).

[25] H. Kosaka, T. Kawashima, A. Tomita, T. Sato, and S. Kawakami, *Photonic-Crystal Spot-Size Converter*, Appl. Phys. Lett. **76** (3), 268-270 (2000).

[26] J. Witzens, M. Loncar, and A. Scherer, *Self-Collimation in Planar Photonic Crystals*, IEEE J. Sel. Top. Quantum Electron. **8** (6), 1246-1257 (2002).

[27] C. H. Chen, A. Sharkawy, D. M. Pustai, S. Y. Shi, and D. W. Prather, *Optimizing Bending Efficiency of Self-Collimated Beams in Non-Channel Planar Photonic Crystal Waveguides*, Opt. Express **11** (23), 3153-3159 (2003).

[28] D. N. Chigrin, S. Enoch, C. M. S. Torres, and G. Tayeb, *Self-Guiding in Two-Dimensional Photonic Crystals*, Opt. Express **11** (10), 1203-1211 (2003).

[29] Z. Y. Li and L. L. Lin, *Evaluation of Lensing in Photonic Crystal Slabs Exhibiting Negative Refraction*, Phys. Rev. B **68** (24), 245110 (2003).

[30] J. Witzens and A. Scherer, *Efficient Excitation of Self-Collimated Beams and Single Bloch Modes in Planar Photonic Crystals*, J. Opt. Soc. Am. A-Opt. Image Sci. Vis. **20** (5), 935-940 (2003).

[31] L. Wu, M. Mazilu, J.-F. Gallet, and T. F. Krauss, *Square Lattice Photonic-Crystal Collimator*, Photon. Nanostruct. **1** (1), 31-36 (2003).

[32] X. F. Yu and S. H. Fan, *Bends and Splitters for Self-Collimated Beams in Photonic Crystals*, Appl. Phys. Lett. **83** (16), 3251-3253 (2003).

[33] D. W. Prather, C. Chen, S. Shi, B. Miao, D. Pustai, S. Venkataraman, A. S. Sharkawy, G. J. Schneider, and J. A. Murakowski, *Ultra Low Loss Photonic Crystal Waveguides Based on the Self-Collimation Effect*, Proc. of SPIE vol. 5360 (Photonic Crystal Materials and Devices II), 175-189 (2004).

[34] D. M. Pustai, S. Y. Shi, C. H. Chen, A. Sharkawy, and D. W. Prather, *Analysis of Splitters for Self-Collimated Beams in Planar Photonic Crystals*, Opt. Express **12** (9), 1823-1831 (2004).

[35] S. Y. Shi, A. Sharkawy, C. H. Chen, D. M. Pustai, and D. W. Prather, *Dispersion-Based Beam Splitter in Photonic Crystals*, Opt. Lett. **29** (6), 617-619 (2004).

[36] K. Sakoda, *Optical Properties of Photonic Crystals* (Springer, 2001).

[37] S. G. Johnson, *Photonic Crystals: From Theory to Practice*, PhD thesis, Massachusetts Institute of Technology (2001).

[38] S. G. Johnson and J. D. Joannopoulos, *Designing Synthetic Optical Media: Photonic Crystals*, Acta Mater. **51** (19), 5823-5835 (2003).

[39] M. Notomi, *Theory of Light Propagation in Strongly Modulated Photonic Crystals: Refractionlike Behavior in the Vicinity of the Photonic Band Gap*, Phys. Rev. B **62** (16), 10696-10705 (2000).

[40] S. H. Fan and J. D. Joannopoulos, *Analysis of Guided Resonances in Photonic Crystal Slabs*, Phys. Rev. B **65** (23), 235112 (2002).

[41] C. Luo, S. G. Johnson, J. D. Joannopoulos, and J. B. Pendry, *All-Angle Negative Refraction without Negative Effective Index*, Phys. Rev. B **65** (20), 201104 (2002).

[42] H. T. Chien, H. T. Tang, C. H. Kuo, C. C. Chen, and Z. Ye, *Directed Diffraction without Negative Refraction*, Phys. Rev. B **70** (11), 113101 (2004).

[43] B. E. A. Saleh and M. C. Teich, *Fundamentals of Photonics* (John Wiley & Sons, Inc., 1991).

[44] J. W. Goodman, *Introduction to Fourier Optics* (The McGraw-Hill Companies, Inc., 1996).

[45] J. A. Kong, *Electromagnetic Wave Theory* (EMW Publishing, 2000).

[46] K. Okamoto, *Fundamentals of Optical Waveguides* (Academic Press, 2000).

[47] S. N. Tandon, *Engineering Light Using Large Area Photonic Crystal Devices*, PhD thesis, Massachusetts Institute of Technology (2005).

[48] S. G. Johnson and J. D. Joannopoulos, *Block-Iterative Frequency-Domain Methods for Maxwell's Equations in a Planewave Basis*, Opt. Express **8** (3), 173-190 (2001).

[49] N. I. Ltd., http://www.nanonics.co.il

[50] N. Axelrod, A. Lewis, N. Ben Yosef, R. Dekhter, G. Fish, and A. Krol, *Small-Focus Integral Fiber Lenses: Modeling with the Segmented Beam-Propagation Method and near-Field Characterization*, Appl. Optics **44** (7), 1270-1282 (2005).

[51] Z. G. Chen, H. Martin, E. D. Eugenieva, J. J. Xu, and J. K. Yang, *Formation of Discrete Solitons in Light-Induced Photonic Lattices*, Opt. Express **13** (6), 1816-1826 (2005).